ENERGY TRANSDUCTION IN SURFACE PHOTONIC CRYSTALS

BY

FUCHYI YANG

DISSERTATION

Submitted in partial fulfillment of the requirements
for the degree of Doctor of Philosophy in Electrical and Computer Engineering
in the Graduate College of the
University of Illinois at Urbana-Champaign, 2011

Urbana, Illinois

Doctoral Committee:

Professor Brian T. Cunningham, Chair
Professor Shun Lien Chuang
Assistant Professor Lynford L. Goddard
Assistant Professor Gang Logan Liu

ABSTRACT

This dissertation is a detailed investigation of the fabrication, design, characterization, and understanding of physical principles of energy transduction in surface photonic crystals which are engineered for various applications. One-dimensional photonic crystals are engineered as optically tunable reflectance filters for λ = 632.8 nm wavelength light by incorporating azobenzene liquid crystal dye molecules into the photonic crystal structure. Optical energy is transduced to accomplish mechanical work by exciting the dye molecules into different physical configurations, leading to changes in the optical properties of the dye molecules, namely their refractive index. This mechanism is used to tune the reflection resonance of the photonic crystal filter. The spectral and temporal optical tuning response of the photonic crystal filter due to excitation light at λ = 532 nm is characterized. Modulation of the transmitted and reflected λ = 632.8 nm light is achieved at microsecond time response. Two-dimensional photonic crystals are also investigated as reflectance filters for λ = 532 nm wavelength light. Both optically tunable and static reflectance filters are studied. Again, azobenzene liquid crystal molecules are incorporated into the photonic crystal to achieve optical tuning of the reflectance wavelength. In this case, the λ = 532 nm wavelength light is used for self-modulation. That is, the light serves both to optically tune the photonic crystal filter as well as to modulate its own reflection efficiency through the photonic crystal filter. Moreover, stacking of multiple photonic crystals into a single filter is studied for both static and optically tunable photonic crystal filters. It is shown that this approach improves the performance of the photonic crystal reflectance filter by increasing its optical density and its angular tolerance at the reflection wavelength of λ = 532 nm. Additionally, surface photonic crystals are fabricated which incorporate quantum dots as light emitters. Enhancement of optical down-conversion is

demonstrated. The quantum dots absorb photons at one wavelength and emit photons at a longer wavelength. The photonic crystal is used to engineer the optical emission behavior of the quantum dots such that the energy conversion between absorbed and emitted photons is controlled. Enhanced excitation of the quantum dots is achieved through resonant excitation of the quantum with photonic crystal modes. Also, enhanced extraction of the emitted photons is achieved through modifying the allowed emitted optical modes provided by the photonic crystal. Photons of certain wavelengths and propagation directions are more efficiently emitted through engineering of the photonic crystal. Normal incident emission enhancement of 7.7x at λ = 875 nm is obtained through the extraction effect. Normal incident emission enhancement of 1.5x is obtained at normal incidence at λ = 865 nm, and a 2x increase in optical down-conversion efficiency is achieved through enhanced excitation effects.

ACKNOWLEDGMENTS

Throughout my PhD research program, many people were integral to the progress and accomplishment of milestones over the years. I would first like to thank my adviser, Professor Brian T. Cunningham, for his enormous contributions in terms of advice, encouragement, guidance, mentorship, and leadership over the past four and a half years. I have learned much from him, and he has been a great influence in my development as a researcher and the person I am today. Also, I would like to thank my doctoral committee members, Professor Shun Lien Chuang, Assistant Professor Gang Logan Liu, and Assistant Professor Lynford L. Goddard, for serving in my doctoral committee. Their comments have been valuable. I would like to thank my research group members who have also been my close friends throughout my graduate school years. I am thankful for all of the discussions we had that helped overcome obstacles and develop new research ideas. I want to thank my mother and father who supported me with love throughout the past years, both emotionally and financially. I wouldn't have been able to make it through the past four and a half years without their encouragement. I would like to thank my friends who have been very supportive and encouraging through the years. I thank you for all of your prayers, blessings, companionship, and all of the memories that were made over the years. Last, I would like to thank God, my father, who has always been faithful to me all of my life. Without Him, nothing would have been possible.

TABLE OF CONTENTS

CHAPTER 1 INTRODUCTION

1.1 Physics of Photonic Crystals

Photonic crystals (PCs) are materials with a periodic variation in their refractive indices [1]. The periodicity may be 1D, 2D, or 3D in nature as illustrated by Fig. 1.1. The solutions to Maxwell's equations for a periodic dielectric permittivity, or refractive index (RI), variation provide the allowed frequencies and propagation vector within the PC. In this case, it is assumed that the material is non magnetic, but the dielectric permittivity ε is spatially varying, Eq. 1.1. The electric and magnetic fields are decoupled by taking the curl of Eq. 1.2 and substituting the expression of the curl of the electric field in Eq. 1.3. The resulting Eq. 1.4 is an eigenvalue equation for the magnetic field and is rewritten in Eq. 1.5 where the operator Θ is defined in Eq. 1.6. The advantage of using Eq. 1.4, instead of the corresponding equation for the electric field, is that the operator is Hermitian. This will guarantee that the eigenvalues, which are the frequencies ω that correspond to the solutions of the magnetic field profiles *H(r)*, will be real quantities. Thus, the magnetic field profile is calculated by solving Eq. 1.4 and the electric field is then calculated from the relation between the magnetic and electric fields in Eq. 1.7.

$$\varepsilon = \varepsilon(r) \tag{1.1}$$

$$\nabla \times \mathrm{E(r)} + \frac{\mathrm{i\omega}}{\mathrm{c}} \mathrm{H(r)} = 0 \tag{1.2}$$

$$\nabla \times H(r) - \frac{i\omega}{c} \varepsilon(r) E(r) = 0 \tag{1.3}$$

$$\nabla \times \left[\frac{1}{\varepsilon(r)} \nabla \times H(r) \right] = \left(\frac{\omega}{c} \right)^2 H(r) \tag{1.4}$$

$$\Theta H(r) = \left(\frac{\omega}{c} \right)^2 H(r) \tag{1.5}$$

$$\Theta = \nabla \times \frac{1}{\varepsilon(r)} \nabla \times \tag{1.6}$$

$$E(r) = -\frac{ic}{\omega \varepsilon(r)} \nabla \times H(r) \tag{1.7}$$

$$H(r) = e^{ikr}u(r) \tag{1.8}$$

Since the medium has a periodic dielectric constant profile, it is known from Bloch's theorem that the solutions to the wave equation must be a plane wave modulated by a periodic Bloch function as stated in Eq. 1.8. The eigenvalues and corresponding eigenfunctions of Eq. 1.4 can be calculated. The eigenvalues $\left(\frac{\omega}{c}\right)^2$ are the frequencies of the PC modes for a particular propagation vector *k* in the PC. Its corresponding eigenfunctions $H(r)$ are the magnetic field profile, which are plane waves modulated by Bloch functions $u(r)$. Taking the propagation vector *k* as a parameter and solving for the eigenvalues *ω*, the dispersion relation $\omega(k)$ is obtained. This dispersion relation is also known as the band diagram of the PC. Fig. 1.2 shows the photonic band diagrams for two 2D PC structures. In Fig. 1.2(a), the PC is a 2D square lattice of cylindrical rods with dielectric permittivity ε = 12 surrounded by air regions of ε=1, while in Fig. 1.2(b), the PC is a 2D triangular lattice of air holes, with ε=1, in a dielectric medium with permittivity ε = 12. Both PCs are periodic in the *xy* plane. It is possible to design the period, RI, and spatial profile of the PC such that there are no allowed electromagnetic modes within a range of frequencies, thus producing a photonic bandgap. The period is on the order of, or smaller than, the wavelength of interest. Thus, the photonic bandgap is a sub-wavelength phenomenon. It is possible to have partial (for one polarization of light, TE or TM) or complete (for both polarizations of light) photonic bandgaps depending on the design of the PC. This is seen in the band diagrams of the PC in Fig. 1.2, where no electromagnetic modes exist within a certain wavelength range regardless of propagation vector. The PC in Fig. 1.2(a) produces a bandgap for TM modes, and the PC in Fig. 1.2(b) produces a bandgap for TE modes. Neither is able to produce a complete bandgap for both TE and TM modes. The lattice constant and RI may be tuned independently in order to vary the wavelength range where the photonic bandgap

arises. In addition, increasing the contrast between different RI regions has the effect of increasing the photonic bandgap width. In addition to taking advantage of the photonic bandgap, PC bands are also useful and are utilized in this work.

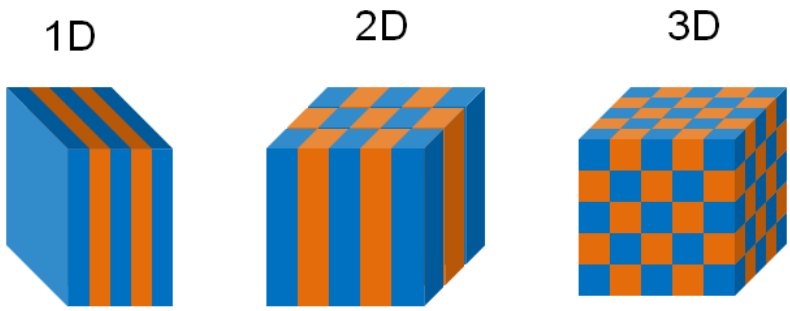

Figure 1.1 Theoretical diagram of a general photonic crystal with 1D, 2D, and 3D periodicities.

1.2 Surface Photonic Crystals and Leaky Modes

In the calculation of a PC band diagram, it is assumed that the medium is infinite in all three directions regardless of whether the periodicity is in 1D, 2D, or 3D. In reality, PCs are finite in dimension. However, when the dimension is large compared to the period of the PC it can be approximated as infinite. For 1D and 2D PC, this is usually the case for directions in the plane of the RI periodicity. However, the orthogonal direction is usually finite and constitutes a finite thickness thin film. Such structures are called surface PCs [1]. The effective RI of the surface PC must be higher than that of the material above and below it in order for surface PC modes to be guided and propagate within the PC structure. The band diagram for a surface PC is similar to that for an idealized PC except that it includes light lines which determine which PC modes are bound within the photonic crystal (non-leaky) and which PC modes can couple to free space (leaky). PC modes that occur below the light lines are non-leaky while modes occurring above the light lines are leaky. The leaky modes of the surface PC can be coupled in from the far field with incident light. Conversely, the leaky modes of the surface PC can couple out of the

PC as far field radiation. This capability is useful for designing high efficiency optical reflectance filters and optical cavities for controlled emission and excitation of optical emitters [3-10].

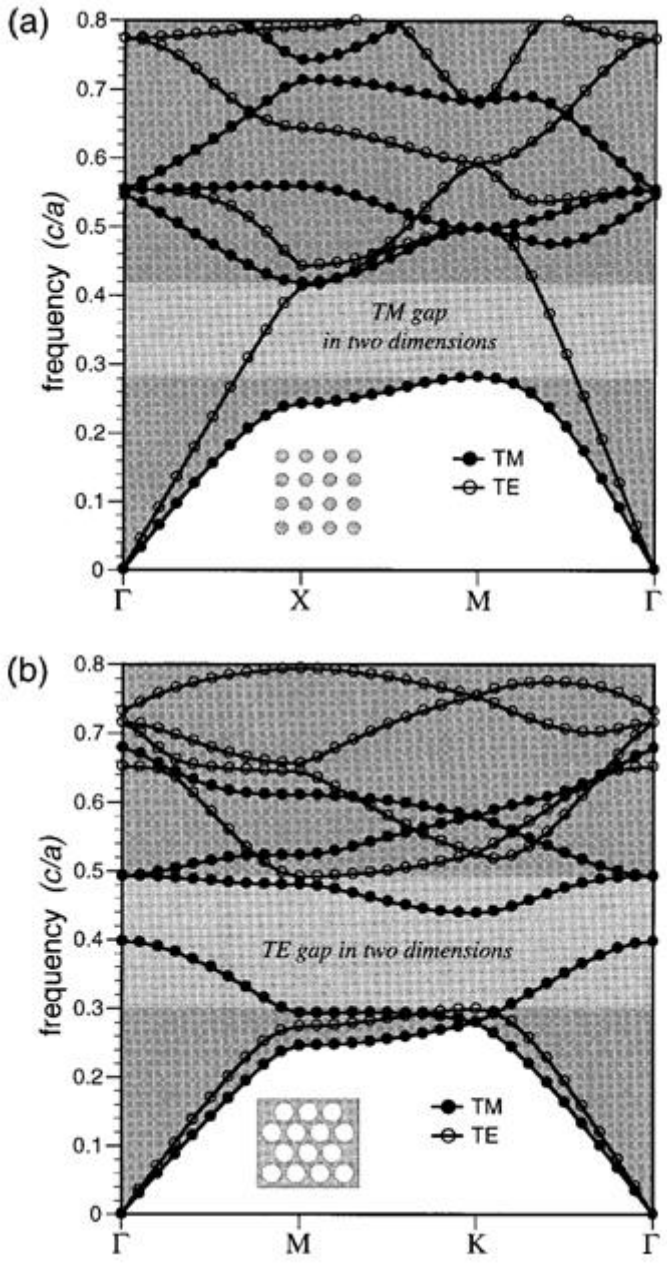

Figure 1.2 (a) Photonic band diagram of a 2D photonic crystal showing a photonic band gap for TM modes. The photonic crystal is a square lattice of dielectric rods in air. (b) Photonic band diagram of a 2D photonic crystal showing a photonic band gap for TE modes. The photonic crystal is a triangular lattice of holes in a dielectric medium. No complete photonic band gap is seen in the band diagram for these two photonic crystals. [2].

An optical reflectance filter, shown in Fig. 1.3, designed in this work incorporates a 1D surface PC. The substrate and superstrate layers are below and above a layer of high RI material. The surface PC, indicated in Fig. 1.3, comprises the layer where there is a RI modulation in the *x*-direction. A thin film of titanium dioxide (TiO_2) is used in this work to provide the high RI necessary to support the surface PC modes.

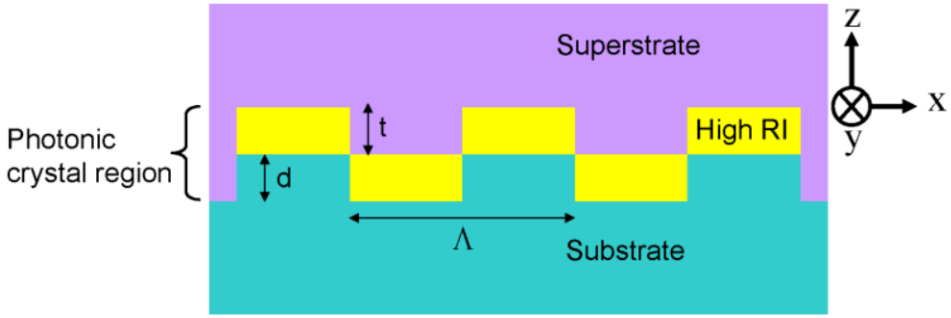

Figure 1.3 Cross section schematic of generic 1D surface photonic crystal optical reflectance filter. Parameters are the modulation height *d*, high RI layer thickness *t*, period Λ, and RI values of the substrate, superstrate, and high RI layers.

The physical mechanism for optical reflection is based on guided mode resonance [11-15] and is explained as follows. Let the light be broadband, incident in the *xz* plane, and propagating in the +*z* direction. The diffraction equation, Eq. 1.9, illustrates how the incident angle θ and period of the surface PC Λ both have an effect on modifying the initial propagation constant *k* by adding momentum in the direction of the periodicity of the surface PC. In Eq. 1.9, *m* is the diffraction order, λ is the free space wavelength, Λ is the period of the surface PC, and N_{eff} is the effective refractive index of the surface PC layer.

$$ksin(\theta) \pm m\frac{2\pi}{\Lambda} = \beta_x = \frac{2\pi}{\lambda}N_{eff} \tag{1.9}$$

Through the first diffracted order (m=1), certain wavelength and incident angle values will result in a propagation constant in the plane of the surface PC which matches a surface PC

leaky mode with the same wavelength and propagation constant. This satisfies the phase matching condition for the far field incident light to couple into a surface PC mode. From symmetry, the same mechanism for coupling in light also couples light back out of the surface PC in both the transmitted and reflected directions. The light coupled out on the transmitted side destructively interferes with the zero-order transmitted light, while the light coupled out to the reflected side constructively interferes with the zero-order reflected light. This effect results in 100% reflection of the input light for the particular wavelength and incident angle value which is phased matched with the surface PC. The reflection spectrum of a surface PC reflectance filter has a reflection peak at the resonant wavelength for a particular incident angle. The reflection peak has a Lorentzian lineshape due to broadening of the resonance conditions. The wavelength at which 100% resonant reflection occurs is called the peak wavelength value (PWV). At normal incidence ($\theta = 0$), the value of the PWV can be derived from Eq. 1.9 using the fact that the coupling is through the first diffracted order ($m = \pm 1$) and the second-order Bragg condition is met, reducing Eq. 1.9 to Eq. 1.10. At normal incidence, light at the PWV couples to two PC leaky modes, through the ±1 diffraction orders, which have opposite propagation constants within the surface PC, setting up an optical standing wave. This standing wave is resonant with the surface PC and has electromagnetic field intensities which are much higher than the input intensity. In other words, the surface PC mode is a resonant cavity mode and the surface PC can be thought of as a distributed cavity structure.

$$\lambda = \Lambda N_{eff} \tag{1.10}$$

The fact that the second-order Bragg condition is met is just a statement that the normal incidence PWV corresponds to a leaky mode of the surface PC at a band edge in the PC band

diagram. Eq. 1.10 clearly indicates that increasing the effective refractive index of the surface PC will increase the PWV for normal incident light.

Until now, polarization effects have not been considered. The 1D surface PC reflectance filter is dependent on the incident light polarization. In this work, TE (TM) polarization is defined as the incident electric field polarization being orthogonal (in the plane) to the plane of incidence. TE (TM) polarized incident light couples into surface PC leaky modes which are TE (TM) polarized. TE polarized surface PC modes have electric fields in the *y* direction, while TM polarized surface PC modes have electric fields in the *x* and *z* directions, as defined in Fig. 1.3. This fact is important when attempting to vary the PWV through changes in refractive index of the surface PC as discussed in more detail in later chapters. The TM mode occurs at lower PWV than the TE mode for the same mode order. This is a result of the TM mode electric field spatially overlapping with more of the low RI region of the surface PC than the TE mode. Thus, the TM surface PC mode has a lower effective RI than the TE surface PC mode and results in a shorter wavelength (lower PWV), as seen from Eq. 1.10. Moreover, the full width at half maximum (FWHM) of the resonant reflection peak is narrower for the TM mode than the TE mode. In other words, the quality factor is lower for the TE surface PC leaky mode than the TM surface PC leaky mode. This is due to the greater diffraction loss for the TE surface PC leaky mode. The spatial mode profile of the TE resonance is concentrated in the high RI region, which is where the grating structure is located. This results in greater spatial overlap with the grating region, and hence greater diffraction loss, for TE modes compared to TM modes. The FWHM can be made narrower in mainly two ways. The first approach is to decrease the RI contrast between the high and low RI regions in the surface PC. The second approach is to decrease the thickness of the PC layer. For the structure used in this work, this is done by either decreasing

the height of the grating or reducing the thickness of the high refractive index TiO_2 layer. Decreasing the height of the grating will not affect the PWV. However, reducing the thickness of the high RI TiO_2 layer will cause a blue shift of the PWV. The optical properties of a 1D surface PC are simulated using rigorous coupled wave analysis (DiffractMod, RSOFT), which provides solutions to Maxwell's equations for periodic structures. The simulation region comprises a single lattice of the PC structure with periodic boundary conditions in the *x* direction. The PC is a three layer structure with a high RI layer surrounded above and below by two low RI layers. Figure 1.4 shows the simulated reflection spectra for a 1D surface PC reflectance filter for both TE and TM polarizations at normal incidence. As simulated, the TM mode is at a shorter PWV than the TE mode and has a much narrower FWHM as well.

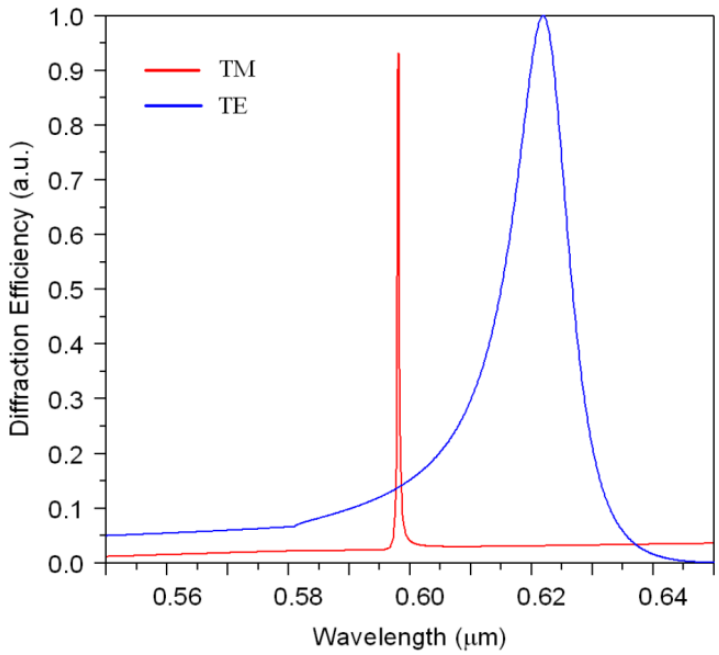

Figure 1.4 RCWA simulation results for two different input polarizations. Theoretical reflection efficiencies of 100% are possible for both polarizations.

It is possible to couple incident light into surface PC modes of orders higher than the first order mode through higher diffraction orders. This has the effect of producing additional resonant reflection peaks in the reflection spectrum of the surface PC which occur at shorter wavelengths due to the higher mode order. However, it is relatively easy to design a single mode surface PC reflectance filter that exhibits only a single TE and TM mode at normal incidence. This is mainly done by keeping the surface PC thin so that only the first-order mode can be supported within the surface PC.

When the incident light is at an oblique incident angle, the conditions for coupling into the surface PC are met by two different wavelengths, as the ±1 diffracted orders no longer result in equivalent propagation vectors as seen from Eq. 1.9. As a result, the degenerate leaky mode at normal incidence splits into two distinct leaky modes at oblique incident angles. The PWV of one leaky mode is red-shifted and the other blue-shifted with respect to the normal incident leaky mode PWV. Additionally, the standing wave that is produced at the normal incidence condition is lost. This behavior can be observed by simulating oblique incident light on the surface PC using RCWA. Fig. 1.5 plots the locations of the PWV as a function of wavelength and incident angle for TM polarized incident light with the reflection value depicted in color scale. Varying the incident angle enables coupling to surface PC modes with different propagation vectors and frequencies. By this method, it is possible to map out the surface PC leaky modes that are allowed in the structure. Thus, this type of plot is the surface PC band diagram for the leaky modes, and it can be experimentally observed and characterized. In Fig. 1.5, a photonic bandgap for TM modes can be seen at normal incidence and the normal incident PWV corresponds to one of the band edges. For oblique incidence, the PWV occurs at the different optical modes allowed by the photonic crystal dispersion.

This work also investigates the design and characteristics of 2D surface PCs. Optical reflectance filters using 2D surface PCs have the same basic behavior as in the 1D case. The 2D surface PC is used to phase match the incident light to couple to its leaky modes. This coupling also results in high resonant reflections at certain wavelength and incident angle conditions that are necessary to satisfy the phase matching condition. Behavior of the resonance modes due to changes in the dimensions and parameters of the 1D surface PC can be extended to the 2D case. However, a major difference between the 1D and 2D surface PC is that the PC leaky modes are polarization independent at normal incident for the 2D surface PC. For unpolarized light at normal incidence, the 2D surface PC can reflect 100% of the intensity at the PWV compared to 50% for a 1D surface PC. Thus, for practical applications it is much more useful to utilize a 2D surface PC.

For 2D surface PC filters, the surface PC modes cannot be separated into TE and TM modes. There exist TE and TM *like* modes in the 2D surface PC, but polarized incident light can couple into both types of modes. Whether the incident light is TE polarized, TM polarized, or unpolarized, the reflection spectrum of the 2D surface PC filter will feature both TE and TM *like* resonant reflection peaks.

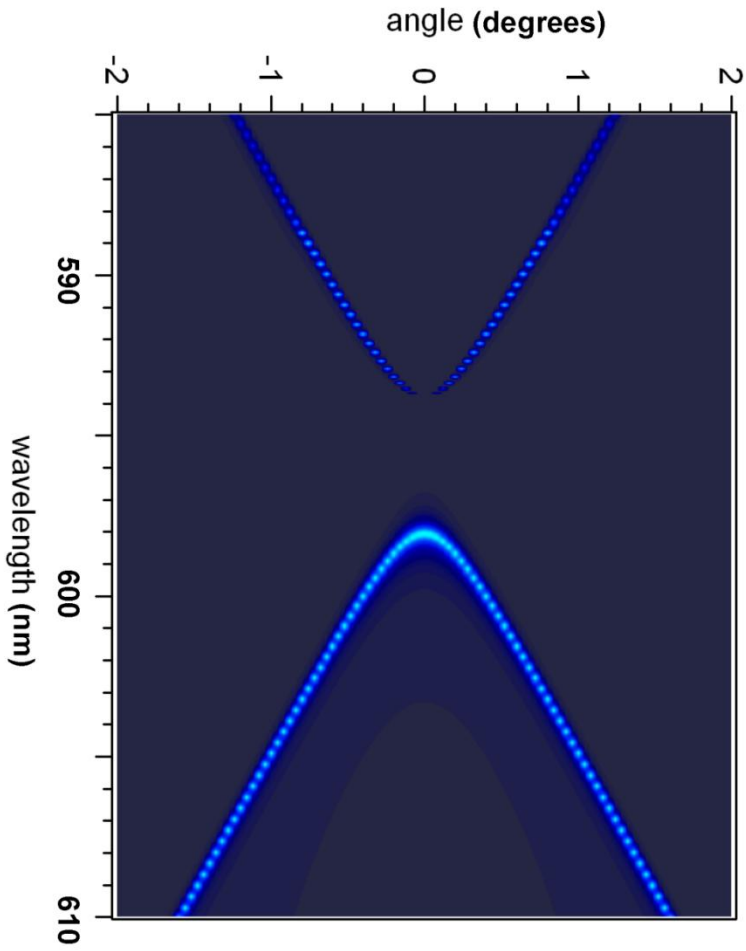

Figure 1.5 TM dispersion diagram of a 1D surface photonic crystal reflectance filter. The in-plane wave vector is analogous to the incident angle. Bright blue regions indicate high reflection values due to resonant reflection through the guided mode resonance effect. A clear photonic band gap of about 4 nm is achieved for the simulated surface PC.

CHAPTER 2 ALL OPTICALLY TUNEABLE TWO-DIMENSIONAL PHOTONIC CRYSTALS INCORPORATING AZOBENZENE DYE MOLECULES

2.1 Motivation

Research on optical filters has a long history. In consequence, many different approaches to optical limiting have been developed over the years. Optical limiting refers to the blocking of transmitted light in the visible wavelength range, which spans λ = 380-750 nm [16]. Some common mechanisms of optical limiting are through either absorption, reflection, or destructive interference [17]. If the optical limiting occurs selectively within a wavelength range, then the device also acts as an optical filter. In many applications such as optical signal modulation, wavelength division multiplexing, spatial light modulation, spectroscopy, and imaging it is desirable to have the capability of tunable optical limiting [18-23]. For example, Bouhifd et al. performed in vivo endoscopic fluorescence imaging of rat pancreas and in vitro fluorescence imaging of cells using acousto-optic tunable optical filters spanning the visible wavelength range [18]. In another work, Gan et al. developed an electro-optically tunable Fabry-Perot filter with a 10 nm tuning range for 10 V input voltage at communication wavelengths for application in high speed spatial light modulation at 200 kHz [19]. Tunable optical limiting refers to the dynamic modulation of the transmission and blockage of a target wavelength of light through some controllable mechanism(s). The work presented here will attempt to address the need for a large area and mechanically flexible tunable optical limiting filter for visible wavelengths.

One approach to tunable optical limiting filters is the twisted nematic liquid crystal (LC) cell [17]. This optical limiting filter, as well as its derivatives, is ubiquitous in the LCD display industry. The concept is to have a layer of LC which has a 90º twist in its molecular alignment from one side of the layer to the other. At each end of the LC layer, there are linear polarizers which are crossed at 90º to one another. Light which is incident on this structure is transmitted

when the LC layer is undisturbed. This occurs since the light polarized by the first polarizer is rotated 90º from its initial direction by the LC layer as it propagates and reaches the second polarizer. Thus, it is allowed to transmit through the second polarizer. When an electric field is applied across the LC layer and perpendicular to the plane of the polarizers, the molecules rearrange to line up parallel to the direction of the electric field lines, and no longer maintain their twisted characteristic. The medium undergoes a transition from an anisotropic to isotropic medium. Therefore, light which passes through the first polarizer no longer rotates its polarization direction as it propagates through the LC layer. When the light reaches the second polarizer, it is now blocked due to its crossed orientation. Even though this approach is well developed, a main concern is the lack of wavelength selection in optical limiting. Thus, all visible wavelengths are blocked since the polarizers are broadband. Another disadvantage is that the transmitting state of the twisted nematic LC cell transmits only 50% of the incident light intensity due to the presence of the first linear polarizer.

Another well developed optical limiting filter is the Bragg filter or Bragg stack [17, 24]. The optical limiting is based on reflection due to Bragg scattering, which is fundamentally a destructive interference effect. Bragg filters are wavelength selective and can have high reflection efficiencies. Such filters are made from a multilayered dielectric stack of two different alternating refractive indices. The center wavelength of the reflection band can be designed by engineering the optical thickness of each layer to be a quarter wavelength of the center wavelength value. The wavelength range of reflection can be on the order of 100 nm, which may be too wide for some applications. Narrowband reflection can be achieved at the expense of reducing the refractive index (RI) contrast between layers and increasing the total number of layers in order to maintain adequate reflection efficiency. In addition, the reflection spectrum

has high side lobes which reduce transmission at surrounding wavelengths. More crucial is the demanding and meticulous fabrication process. Fabricating Brag filters routinely consist of multiple depositions of as many as 100 alternating refractive index layers while maintaining strict control of the thickness of each layer. This is an expensive process by which it is difficult to achieve uniformity over a surface area of several square centimeters. For example, Chen et al. fabricated a Bragg filter comprising 54 dielectric layers and achieved a transmission of 10^{-7} at 1.06 μm [24]. The number of layers may be reduced, but to maintain the same reflection efficiency, the refractive index difference between the two layers must be increased. This can be impractical in terms of finding suitable dielectric materials for deposition, and it also increases the reflected wavelength bandwidth.

A third category of major optical limiting filters are dye based materials [25]. These filters depend on the optical absorption properties of certain dyes, doped within either a glass or polymer matrix as the structural material, to optically limit the transmission through these devices. Depending on the dye used, it is possible to design optical limiting filters that cover a certain range within the UV, visible, and NIR wavelengths. Grout designed an optical limiting filter for visible wavelengths using a photoactive chromoprotein, bacteriorhodopsin, as the optically absorbing material [25]. Typically, the absorption spectrum of commonly used dyes extends over a wide range of several hundred nanometers. This is disadvantageous for applications requiring high transmission over most of the visible wavelength range. To achieve highly efficient optical limiting values, it is crucial to use a high concentration of dye doped in either the glass or polymer matrix. Also, thicker layers of the material are used to increase the optical limiting effect resulting from the increased absorption based on Beer's law. Having these

thick layers of material is a disadvantage for portability and wearability due to the size and weight that these filters may have.

Previous work has combined the use of LC with photonic crystal (PC) structures for tunable optical limiting. Haurylau et al. have incorporated liquid crystals in 2D PC fabricated out of silicon substrates [26]. The devices were made using interference lithography and CMOS compatible processes. Electro-optical tuning of the photonic bandgap was achieved. Chang et al. demonstrated an electro-optically tunable 1D surface PC reflectance filter using LC and fabricated on a glass substrate using nano-imprint lithography [27]. Electro-optical tuning at communication wavelengths with $\Delta\lambda = 20$ nm was achieved with 20 V applied. Inoue et al. have demonstrated temperature tuning of reflection at communication wavelengths using 2D PC slabs incorporated with LC and fabricated on silicon nitride membranes using electron beam lithography [28]. No prior work, including the aforementioned, has demonstrated tunable optical limiting at visible wavelengths for a large area device on a flexible substrate.

The following research aims at producing a tunable optical limiting filter that will be used for eye and sensor protection against high power and high energy laser irradiation in the visible wavelengths. The optical limiting filter will be incorporated in a laser visor which has a curved surface. Thus, it is essential that the device be flexible. Moreover, the optical limiting is targeted at a specific wavelength, so a narrowband filter is desired. This is also a practical consideration, so that a person looking out of the visor is able to see most of the visible spectrum and maintain quality of sight. In applications for sensor protection, such as visible, thermal and night vision imaging sensors, this will enable most of the light to reach the sensors for imaging while still protecting the sensors from laser irradiation at the target wavelength. In addition, the optical limiting filter will need to cover a large area of at least the visor dimensions of several

square centimeters. It is desirable to produce a very large area optical limiting filter which can be cut into desired dimensions and shapes. The ease and cost of fabrication are important, which should be as simple and inexpensive as possible. The optical limiting filter needs to be tunable so that it responds to a target laser wavelength. Initially, the optical limiting filter should allow most visible wavelengths through. When laser light of the target wavelength is incident on the optical limiting filter, the optical limiting filter will block the target wavelength and protect either the eye of a person or a sensor. It is the premise of this research that tunable 1D and 2D surface PC optical reflectance filters are an appropriate approach to this problem. The surface PC relies on the guided mode resonance effect to achieve narrowband resonant reflection at visible wavelengths while maintaining high transmission values at off-resonant wavelengths. Nanoreplica molding is used to fabricate the photonic crystal structures over large areas using master templates up to 8 inch diameter silicon wafers. The photonic crystals are fabricated on plastic substrates which are optically transparent and mechanically flexible. All optical tuning of the resonant reflection wavelength is achieved by using azobenzene LC.

2.2 Azobenzene Liquid Crystals and the Optical Kerr Effect

Liquid crystals (LCs) are a well known class of materials that exhibit properties of both solids and liquids. Like liquids, individual LC molecules are able to move around relative to one another and are not fixed in any position relative to their neighbors. However, like some solids which have crystal structures, LC have long range ordering which has important physical consequences. There are subclasses of LC which display different degrees and types of order as shown in Fig. 2.1. The director is a vector which points in the direction of the long axis of the LC molecule and is used to describe its molecular orientation. Nematic LC have their director aligned in a single direction, but the LC molecules still have three degrees of freedom to move

their position in space. Smectic LCs also have their director aligned in a single direction, but they contain an additional degree of order in which the LC molecules must be located within certain planes in the bulk medium. A third type of LC is cholesterics which have molecules ordered in a helical fashion. There are other considerations with LC such as temperature-dependent phases and dislocations/defect states which are beyond the scope of this research.

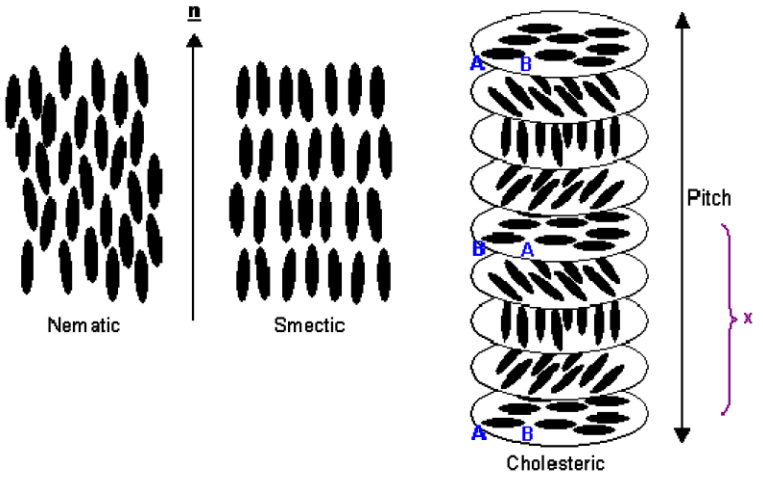

Figure 2.1 Diagram showing different liquid crystal phases [29].

Azobenzene is a particular type of molecule which has two benzene rings connected by a nitrogen–nitrogen bond. This configuration has the unique property of photo-isomerization. The azobenzene molecule can exist in either a *trans* or *cis* isomer as shown in Fig. 2.2. The *trans* isomer is the ground state of the molecule while the *cis* isomer is a metastable energy state and requires a minimum excitation energy for the molecule to undergo a change from the *trans* to *cis* isomer. The isomerization can be accomplished through a photon absorption event, provided the photon has sufficient energy. Through photon absorption, the electron wave function of the molecule is altered into an excited state which in turn induces a torque on the molecule due to the altered charge distribution within the molecule [30-32]. Isomerization of the molecule is achieved through rotation centered at the nitrogen-nitrogen bond. Thus, optical energy is

transduced to mechanical energy. Certain molecules which have the azobenzene group have been engineered to also exhibit liquid crystalline properties. Thus, these materials are called azo-LC and exhibit properties of both LC ordering and photo-isomerization [33-36]. Additionally, the *trans* and *cis* isomers result in different refractive indices of the bulk material, providing the ability to tune the RI of azo-LC using a pump light source within the absorption spectrum of the azo-LC molecules to achieve photo-isomerization. This intensity induced RI change is a third-order nonlinear process called the optical Kerr effect. The RI change is governed by Eq. 2.1, where I is the intensity of the input field, and n_2 is the nonlinear refraction coefficient defined in Eq. 2.2.

$$\Delta n = n_2 I \tag{2.1}$$

$$n_2(\omega) = \frac{3}{8}\frac{Re\chi^{(3)}(-\omega;\omega,-\omega,\omega)}{n_0(\omega)} \tag{2.2}$$

The particular azo-LC mixture used in this research is named LC 1005 and provided by BEAM corp. LC 1005 is a nematic LC, and it is a mixture of three different molecules with different end groups (or R group) as shown in Fig. 2.2. Using a laser with λ = 532 nm wavelength enables the RI of the azo-LC to be tuned.

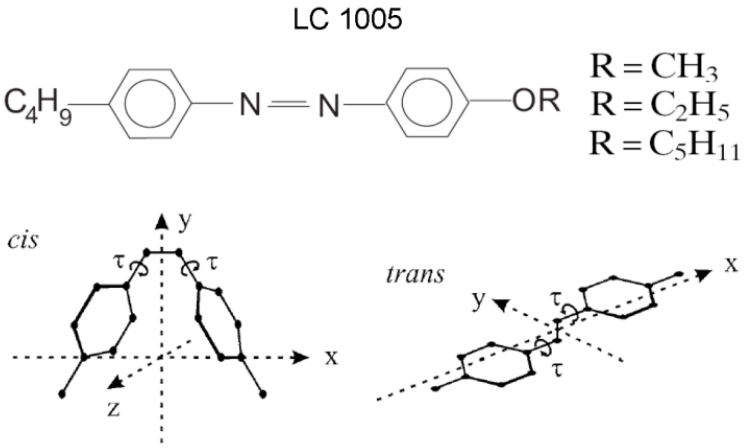

Figure 2.2 Molecular structure of the azobenzene liquid crystal LC 1005. LC 1005 is a mixture of three different molecular derivatives. The end group, R, is a carbon chain of differing lengths. Also shown are the *cis* and *trans* isomers of LC 1005. Figures from [30, 36].

2.3 Fabrication of 1D Surface Photonic Crystal with Azobenzene Dye Molecules

Azobenzene liquid crystal molecules were incorporated into a 1D surface PC to fabricate a narrowband optical reflectance filter with a tunable reflection wavelength when pumped by incoming light at a target wavelength. The 1D surface PC was fabricated using two separate pieces. First, a 1D surface PC structure was transferred from a master wafer onto a polyethylene terephthalate (PET) substrate employing nanoreplica molding. The master is an 8-inch diameter silicon wafer upon which a 1D surface PC structure with a period of Λ=370 nm and a 50% duty cycle is patterned by deep-UV photolithography over a 5x5 in^2 area. The 1D surface PC pattern is etched into the silicon wafer to a depth of d=55 nm by reactive ion etching. A layer of liquid ultraviolet curable polymer (UVCP) was drop-coated on top of the silicon master. The PET substrate is then placed over the master wafer and is then pressed onto the master wafer using a rolling cylinder. This enables the UVCP drops to form a thin continuous layer between the two surfaces and conform to the features of the master. After this has been achieved, the UVCP is cured using a UV lamp for 90 seconds. Next, the PET substrate, along with the UVCP layer, is

released from the master and a cured UVCP layer with a period of Λ=370 nm and a duty cycle of 50% is replicated on the PET substrate as shown in Fig. 2.3.

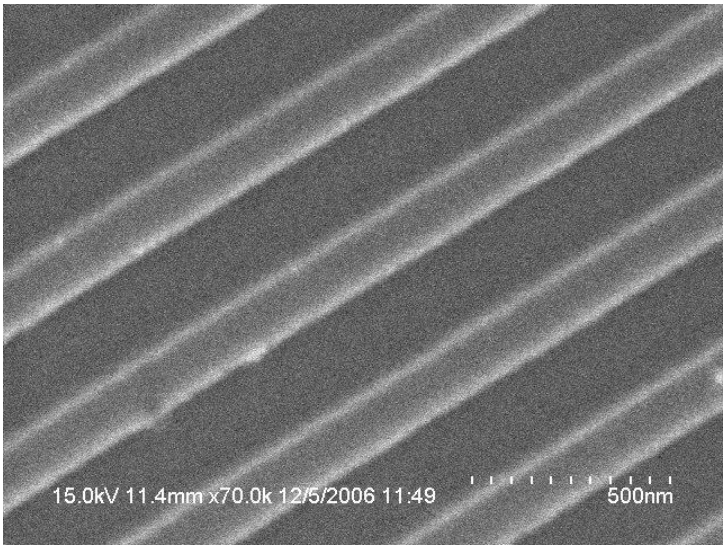

Figure 2.3 SEM image of the UVCP nanoreplica mold from the master wafer. A 1D surface PC structure is seen and the period is Λ=370 nm.

The refractive index of the UVCP layer is approximately n=1.46 in the visible wavelengths. Subsequently, TiO_2, serving as the high refractive index layer with refractive index n=2.2, was deposited on top of this UVCP layer by electron beam evaporation to a thickness of t=90 nm. Another PET substrate was used as a cover layer. A polyimide (PI), PI-2556 (HD Microsystems), film is spin-coated on the PET substrate and then baked and rubbed with a velvet cloth to pre-align the LC parallel the rubbing direction. To finish fabricating the device, the cover layer and the surface PC layer were combined to form a cavity with the azo-LC injected in between the cover and surface PC layers and allowed to spread due to capillary forces. The 1D surface PC and the PI rubbing direction were assembled such that the LC molecules would align in the *y* direction. The cover and grating layers were clamped together between two microscope glass slides for structural support. Since there are no spacers to define a gap in this device, the

capillary forces of the liquid crystal define the thickness of the resulting layer, and it is estimated to be about a few micrometers thick. The parameters for this structure are shown in Fig. 2.4.

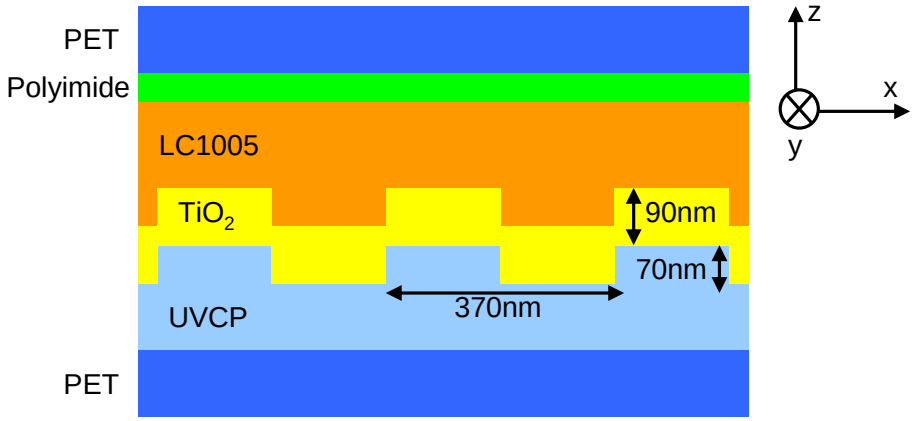

Figure 2.4 Cross section diagram of a 1D photonic crystal filter with a layer of LC1005 as an optically active superstrate.

2.4 Mechanism of Optical Tuning Using Azobenzene in 1D Surface Photonic Crystal

In this work, the *z* direction is vertical to the device substrate, the *x* direction refers to the direction perpendicular to the surface PC modulation, and the *y* direction is parallel to the grating lines as indicated in Fig. 2.4. Light is incident upon the structure from the bottom, propagating in the +*z* direction with its electric field TE polarized. For normal incidence and at the resonant wavelength for TE illumination, an optical standing wave develops with its electric field polarized in the *y* direction.

The rubbed PI film homogeneously aligns the director of the azo-LC parallel to the rubbing direction and parallel to the surface of the PI film [37-39]. Rubbing the PI film reorients the backbone of its long polymer chains parallel to the rubbing direction and also creates physical grooves on the surface of the PI film. These long molecular backbones interact with the LC molecules through Van der Waals forces and induce preferred LC alignment parallel to the rubbing direction. The physical grooves on the surface of the PI film also aid in alignment of the

LC in the same direction. This minimizes the energy state of the LC, and this type of alignment is called homogeneous alignment.

The surface PC reflectance filter can reflect a narrow band of wavelengths centered at the peak wavelength value (PWV) with a theoretical 100% efficiency. The value of the PWV is dependent on the RI of the different materials comprising the surface PC. For both TE and TM polarizations, increases in the superstrate (azo-LC) RI will red-shift the PWV value. Likewise, decreases in the superstrate RI will blue-shift the PWV. A subtle detail differentiates the behavior of the two polarizations, however. RCWA simulations calculate the electric field profiles for the PC modes at their respective wavelengths for both TE and TM polarizations at normal incidence in Figs. 2.5 and 2.6. For TE polarization, only the *y* component of the electric field exists, while only *x* and *z* electric field components exist for TM polarizations. As a consequence, the TE PWV is only dependent on RI changes in the *y* direction, while the TM PWV will be affected only by RI changes in the *x* and *z* directions. This behavior is confirmed using finite-difference time-domain (FDTD) simulations that allow anisotropic materials to be simulated. All the simulations are done with normal incident light, and the reflection spectra are calculated. For results shown in Figure 2.7, the superstrate RI in the *y* direction is changed only, and this results in a shift of the TE PWV only. The opposite is true for only changing RI in the *x* or *z* directions as depicted by FDTD simulation results in Figures 2.8 and 2.9, respectively. This characteristic is an important consideration when using azo-LC, since this material has anisotropic RI.

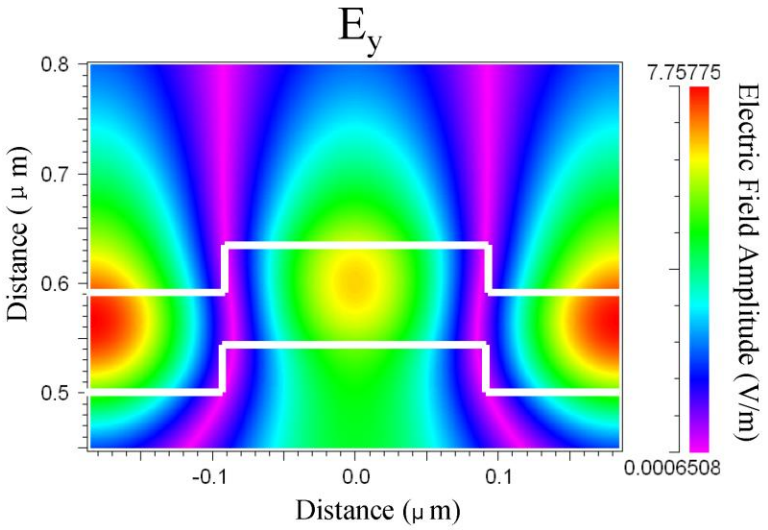

Figure 2.5 TE mode electric field profile for the *y* component. Color scale indicates relative values to the incident electric field.

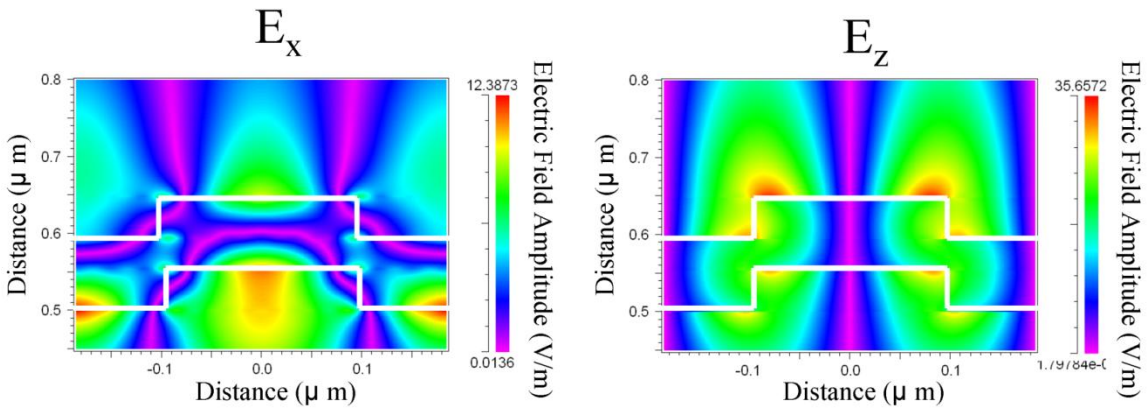

Figure 2.6 TM mode electric field profiles for the *x*- and *z*-components. Relative electric field amplitudes in the incident field are depicted in the color scale. E_z has the largest electric field enhancement due to the smaller FWHM of the TM PWV in comparison to the TE PWV.

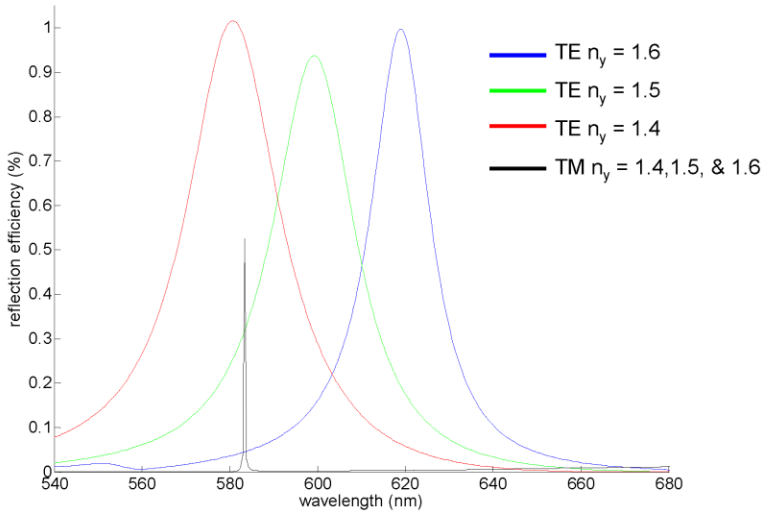

Figure 2.7 FDTD simulations for a 1D surface photonic crystal optical reflectance filter. The *y* component superstrate refractive index is varied from 1.4 to 1.6. The TE PWV (red, green, and blue curves) shifts due to this change, but the TM PWV (black curve) stays stationary and is not affected.

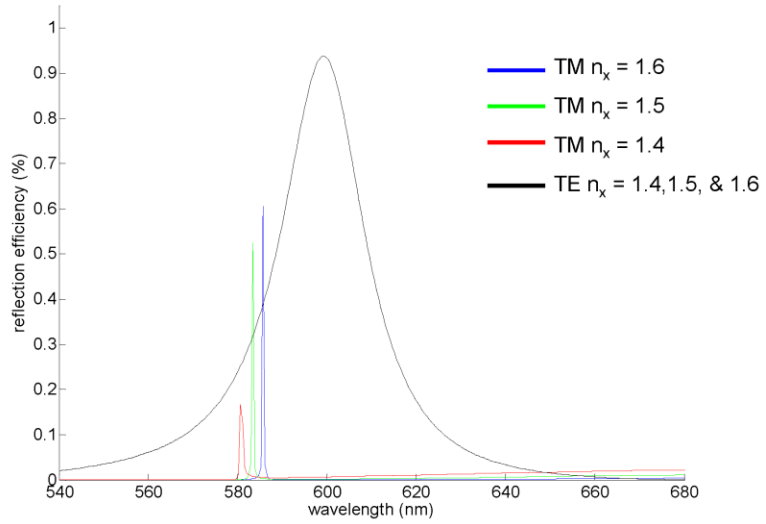

Figure 2.8 FDTD simulations for a 1D surface photonic crystal optical reflectance filter. The *x* component superstrate refractive index is varied from 1.4 to 1.6. The TM PWV (red, green, and blue curves) shifts due to this change, but the TE PWV (black curve) stays stationary and is not affected.

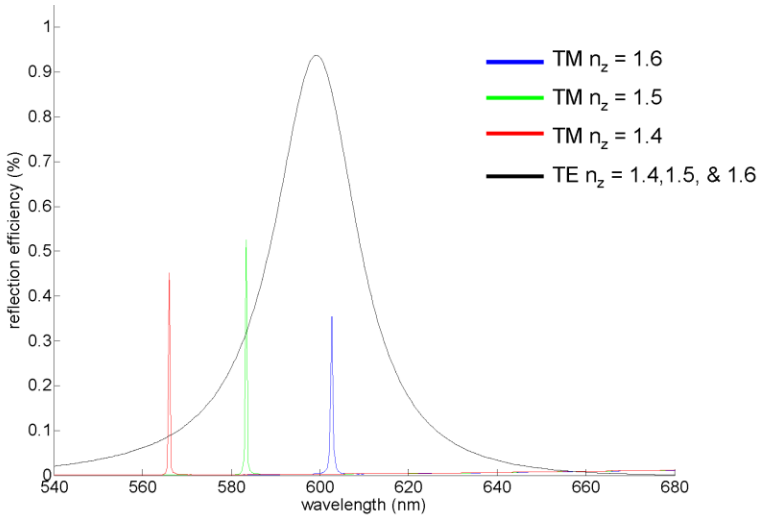

Figure 2.9 FDTD simulations for a 1D surface photonic crystal optical reflectance filter. The *z* component superstrate refractive index is varied from 1.4 to 1.6. The TM PWV (red, green, and blue curves) shifts due to this change, but the TE PWV (black curve) stays stationary and is not affected. Due to the greater overlap of the electric field with the superstrate layer, the PWV shifts are larger than in Fig. 2.8.

For the optically tunable surface PC reflectance filter, this research focuses on the TE mode resonant reflection. Therefore, RI changes in the *y* direction are critical. The azo-LC used in this paper has a RI tensor shown in Eq. 2.3 for the *trans* isomer and the refractive index tensor shown in Eq. 2.4 for the *cis* isomer [36].

$$\begin{pmatrix} n_x & & \\ & n_y & \\ & & n_z \end{pmatrix} = \begin{pmatrix} n_\perp & & \\ & n_\parallel & \\ & & n_\perp \end{pmatrix} = \begin{pmatrix} 1.492 & & \\ & 1.726 & \\ & & 1.492 \end{pmatrix} \tag{2.3}$$

$$\begin{pmatrix} n_x & & \\ & n_y & \\ & & n_z \end{pmatrix} = \begin{pmatrix} n_{cis} & & \\ & n_{cis} & \\ & & n_{cis} \end{pmatrix} = \begin{pmatrix} 1.57 & & \\ & 1.57 & \\ & & 1.57 \end{pmatrix} \tag{2.4}$$

When the azo-LC is exposed to green λ=532 nm light, the azo-LC molecules absorb the light and photo-isomerizes from their *trans* state to their *cis* state. Thus, the RI of the azo-LC layer changes, which shifts the TE PWV. The azo-LC director is initially in the *y* direction due to the rubbed PI film. The *y* RI is thus $n_y = n_\parallel = 1.726$. After photo-isomerization, the RI

changes to $n_y = n_{cis} = 1.57$, resulting in a negative RI change of $\Delta n_y = n_{cis} - n_{\|} = -0.156$. This refractive index change causes the TE PWV to blue-shift as shown in the computer-simulated reflectance spectra in Fig. 2.10.

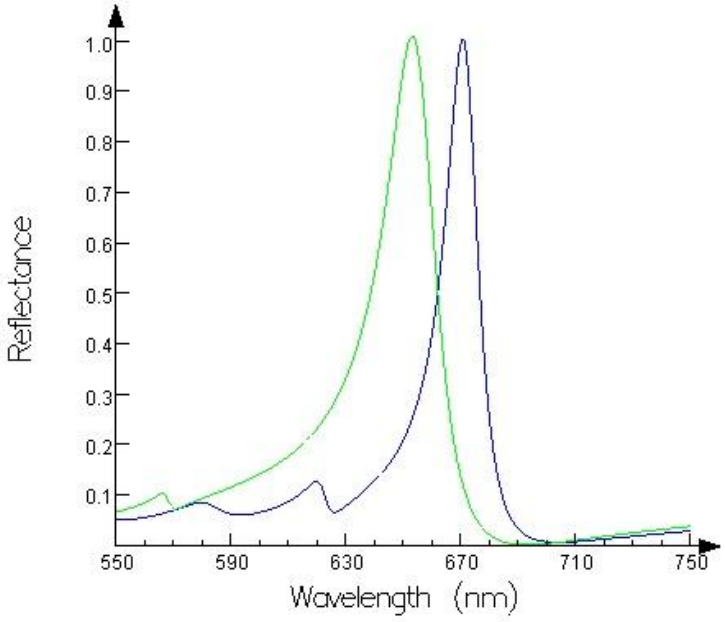

Figure 2.10 FDTD simulation showing the change in the reflectance spectrum when the azo-LC is switched from the *trans* to the *cis* state. The PWV shifts from 670 nm before pumping (blue curve) to 653 nm after pumping (green curve).

Three distinct phases occur during the azo-LC refractive index change: incubation, opalescence, and isotropic [34]. Initially all of the azo-LC molecules are in the *trans* isomer. When less than 19% of the molecules have converted to *cis* isomers, the azo-LC layer is able to maintain its nematic ordering while simultaneously changing its refractive index. Above this critical value, the large amount of *cis* isomers disrupts the nematic ordering and micron-size droplets form. These droplets create an opalescence phase that scatters and reduces the transmission of light in the visible wavelength. Experimentally, the sidebands of the surface PC filter's transmission spectrum decrease as scattering occurs. As the concentration of *cis* isomers approaches 100%, the layer becomes a uniform, homogeneous film of isotropic *cis* molecules

and no LC ordering is maintained. Thus, scattering is reduced, and the transmission of the sidebands returns to its initial value. Throughout all three stages, the RI of the azo-LC layer decreases, which blue-shifts the TE PWV.

2.5 Temporal and Spectral Response of Optical Tunable 1D Photonic Crystal at 632.8 nm

Tuning of the optical photonic crystal filter is characterized using the pump/probe setup shown in Fig. 2.11(a). A pulsed laser is used to tune the azo-LC molecules and induce *trans* to *cis* photo-isomerization. Meanwhile a low-power light source is used as a probe to observe tuning of the 1D surface PC PWV without perturbing it. Pulsed laser sources use a method known as Q-switching, which allows the laser cavity gain to become much higher than the loss in the system. When the laser cavity is allowed to lase, the output of the laser is a temporally short pulse of very high output power. Pulse widths of nanoseconds are common, and femtosecond pulses are state of the art. The instantaneous power of such pulses is on the order of megawatts. The advantage of using a pulsed laser instead of a CW laser is that much more energy is delivered to an area of the surface PC filter in a short time. This can drastically reduce the response time of the surface PC filter. The particular pulsed laser used in this research is an Nd:YaG laser and has a pulse width of 5-10 ns. The maximum pulse energy is approximately 17 mJ and the output emission is at λ=532 nm. The energy per pulse can be adjusted continuously. The transmission spectrum of the surface PC filter is obtained using broadband incident light from a tungsten halogen lamp coupled to a fiber optic cable. The incident light was TE polarized using a linear polarizer and collected on the transmitted side using another fiber optic cable which was connected to a spectrometer. The spectrometer output was observed using commercial software from Ocean Optics. The surface PC filters were mounted on a rotating stage which allowed adjustment of the angle of incident light in the *xz* plane as referenced in Fig.

2.4. Also, the PC filter was attached to a tilt mount which enabled adjustment of the surface PC filter to normal incident with respect to the incoming light.

The TE PWV is analyzed and tuned by operating the laser in single shot mode. This allows triggering of individual pulses. The TE PWV blue-shifts as expected, and it tunes from λ=658 nm to λ=635 nm with three pulses as shown in Fig. 2.12. The pulsed laser was set to its maximum energy setting of 17 mJ/pulse. Other experiments performed with lower energy pulses show additional pulses are needed to accomplish the same PWV shift as expected.

It was noticed in the real time transmission spectrum that the PWV would blue-shift when pumped with the pulsed laser and then partially relax back by red-shifting. The amount of red shift would decrease with additional pulses from the pump laser until the PWV remained stable. This behavior is attributed to the diffusion of azo-LC molecules. The λ = 532-nm light is mostly absorbed near the PC surface, since it is incident in the +*z* direction. The resonant wavelength is sensitive to the RI of the material within the evanescent field region of the superstrate since it is material within this region which contributes to the effective RI experienced by the PC leaky mode. This evanescent region extends to about 100-200 nm above the TiO2 layer as seen in Fig. 2.5. As expected, the blue shift is due to the *trans* to *cis* photo-isomerization of the azo-LC near the PC surface. Meanwhile, unconverted *trans* azo-LCs from above the PC surface diffuse into the evanescent field region and cause a red shift in the PWV due to the increased RI of the *trans* isomers.

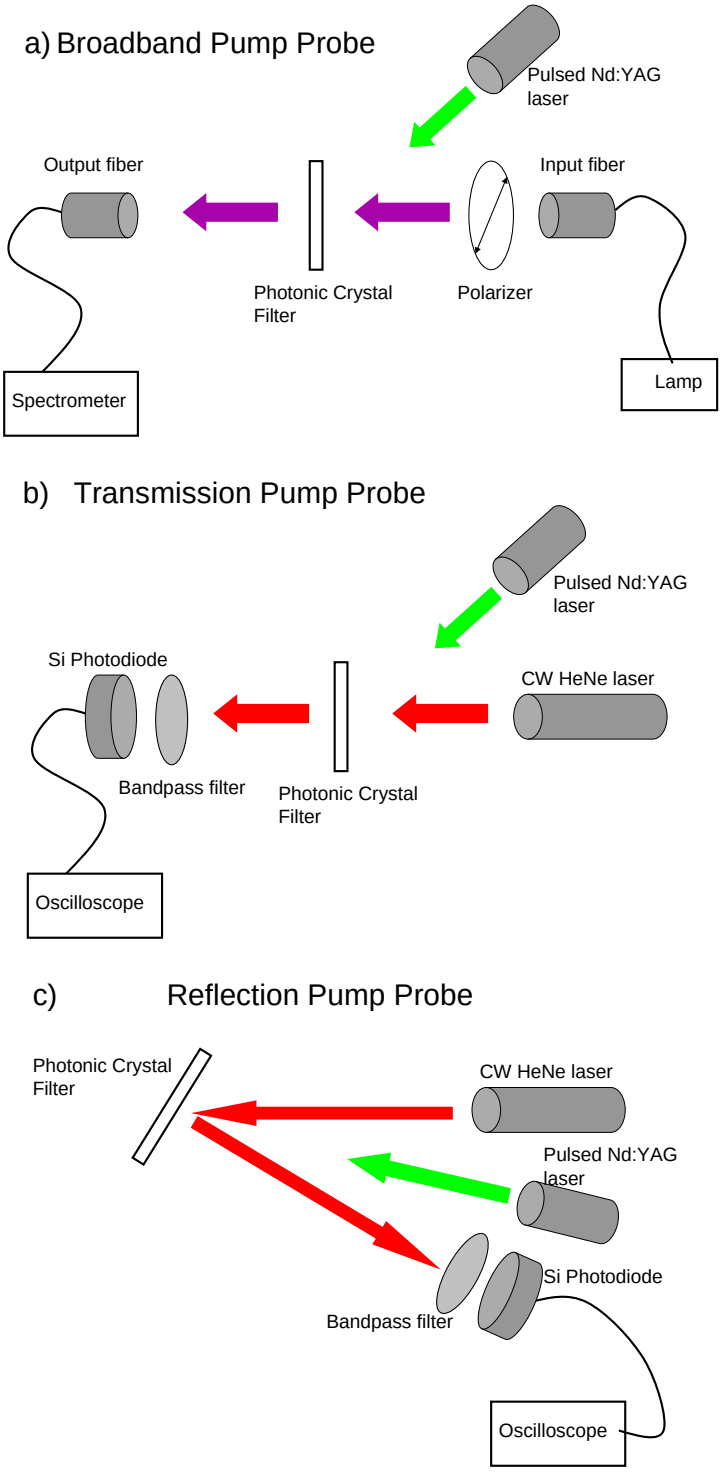

Figure 2.11 The experimental pump probe diagram is illustrated. a) Broadband light from a tungsten halogen lamp is coupled through an optical fiber and illuminated through a polarizer, and the transmitted signal is collected through an optical fiber and to a spectrometer. A pulsed Nd:YAG laser is used as pump source to tune the PWV of the PC filter. b) Single wavelength transmission pump probe setup using a HeNe laser as the probe source. A bandpass filter is placed in front of the silicon photodiode which detects the transmitted probe intensity. c) Single wavelength reflection pump probe setup. Similar to b).

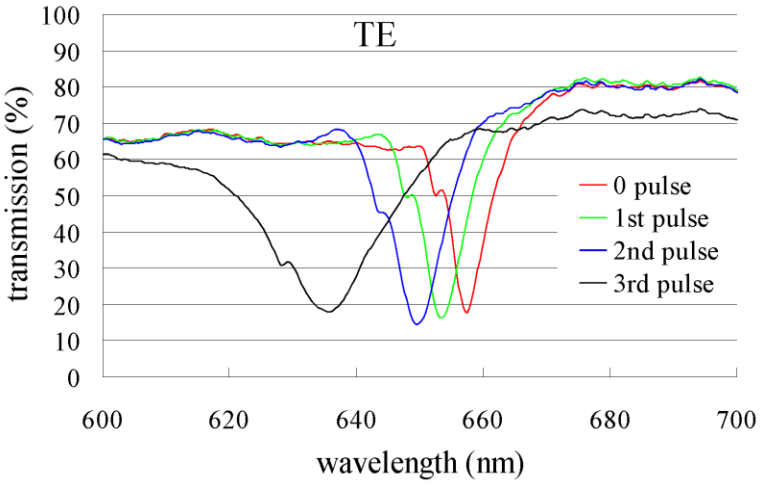

Figure 2.12 Transmission spectra of a photonic crystal filter with LC 1005. The pump source is a pulsed laser. Each pulse induces an incremental shift in the PWV. Three pulses are shown to achieve a full range shift of the PWV.

To minimize this problem, it is possible to operate the device at a colder temperature to slow the diffusion of the azo-LC molecules, but this is undesirable. A more suitable approach is to fabricate the azo-LC layer as thin as the evanescent field region of approximately 200 nm thickness. With a thinner layer, less azo-LC molecules need to be photo isomerized, and the RI tuning can be achieved with lower total energy and consequently fewer pulses from the pump laser. Additionally, fewer *trans* isomers would remain after each pulse from the pump laser, so diffusion of *trans* isomers would be negligible.

The temporal response for optical tuning of the 1D surface PC reflectance filter is characterized using the pump/probe setups shown in Figs. 2.11(b)-(c). Transmission and reflection setups are both used to probe the 1D surface PC filter, while a pulsed Nd:YAG laser at λ=532 nm provides the pump excitation light. A HeNe laser at λ=632.8 nm is used as a probe light. The transmission/reflection of the HeNe laser is detected using a Si photodiode at the transmission/reflection side of the 1D surface PC filter. A bandpass filter at λ=632.8 nm is used to filter out any light from the λ=532 nm pump source. The photodiode is connected to an

oscilloscope and the data is recorded using a custom LabView program. Because of fabrication error, it is difficult to make surface PC filters with exactly λ=632.8 nm TE PWV. For experimental purposes, it is possible to vary the incident angle of the HeNe laser with respect to the 1D surface PC filter in order to obtain a TE PWV at λ=632.8 nm. This is possible because exciting the 1D surface PC modes is dependent on both wavelength and incident angle as discussed previously in Chapter 1. For the transmission setup, the λ=632.8 nm light is initially at an incident angle which is non-resonant with the surface PC filter, and it is transmitted by the device yielding a maximum signal value from the photodiode. When the λ=532 nm pump laser illuminates the surface PC filter, it excites the azo-LC molecules and the TE PWV tunes to λ=632.8 nm. Thus, the light from the HeNe laser is now blocked by the surface PC filter, and the photodiode signal decreases. The transmitted signal at λ=632.8 nm is then detected as a function of time while the device is being tuned with the pulsed laser at λ=532 nm. The complementary behavior occurs when using the reflection setup. The observed reflected signal is initially at a low value due to little reflection from the surface PC filter. Then, the pump light causes the TE PWV to shift to λ=632.8 nm and an increase in the reflection signal is detected on the Si photodiode due to the resonant reflection from the surface PC filter.

A reflection pump/probe setup was used to investigate the effect of varying the power from the pump source and probe source independently. The Nd:YAG pump source was kept constant at 6 mJ/pulse and a10 Hz output rate. The HeNe probe was varied from 0.5 mW to 1.5 mW. The response of the photonic crystal filter is plotted in Fig. 2.13. The starting and ending values of the traces are different because the HeNe power is varied. Higher HeNe power results in overall higher values detected from the photodiode. However, the increase in signal (difference between the ending and starting signal value) relative to the starting signal value is

the similar because the pump source shifts the TE PWV by the same amount in all three cases. That is, the same amount of energy from the pump source is used to excite the azobenzene, molecules which results in the same RI shift and leads to the same TE PWV shift in the PC filter.

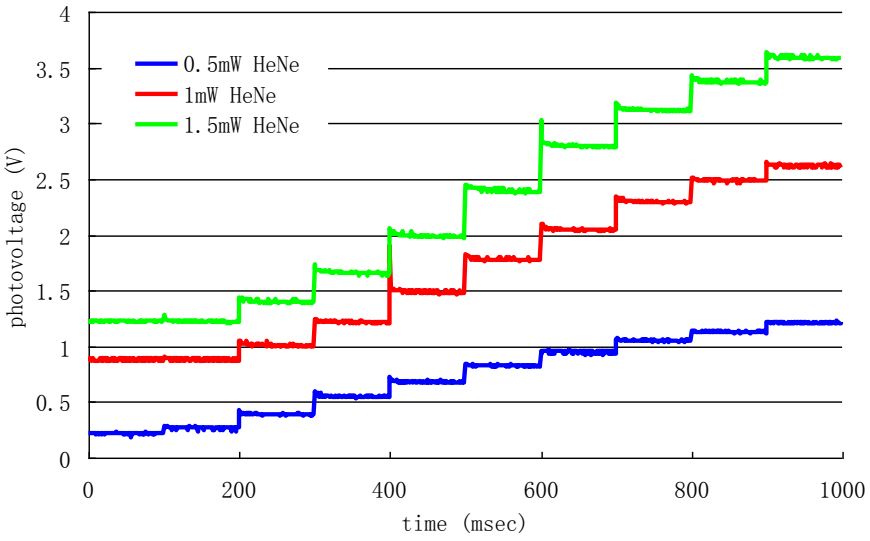

Figure 2.13 Reflection pump probe results for different HeNe laser incident powers. The pump source is kept constant at 6 mJ/pulse and 10 Hz.

When the probe light is kept at constant power and the pump light energy is varied, the response is different. Fig. 2.14 shows the time response of the surface PC filter for this case. Since the HeNe power is kept constant, the starting signal level of the photodiode is the same for all cases. However, the 6 mJ/pulse pump source produces much larger TE PWV shifts due to more RI change of the azo-LC layer. Consequently, much larger signal increases than the 2 mJ/pulse pump source are observed through the photodiode output. Thus, the device responds much faster to higher energy pulses. This is expected since more azo-LC molecules will be excited from *trans* to *cis* isomer for each λ=532 nm laser pulse, resulting in a larger RI change. This leads to the TE PWV shifting closer toward λ=632.8 nm enabling resonant reflection of more of the probe light.

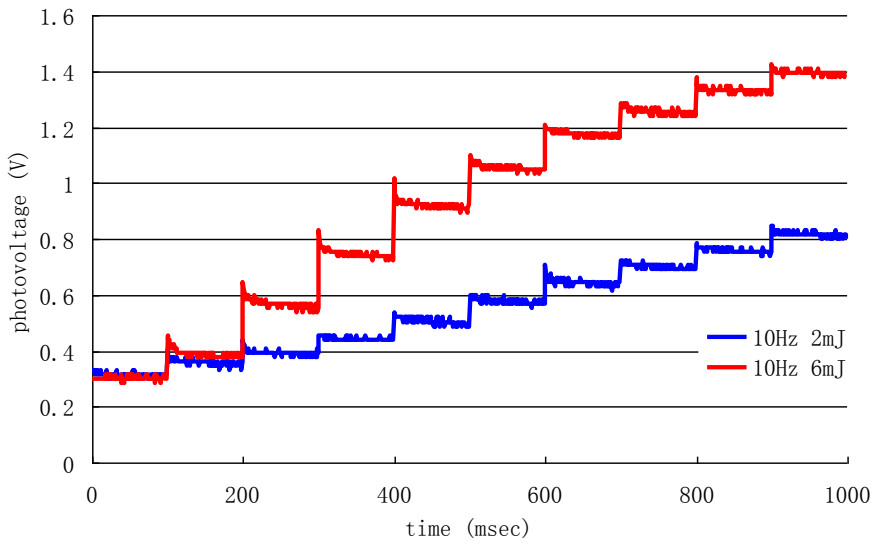

Figure 2.14 Reflection pump probe results for different Nd:YAG laser incident pulse energies. The probe beam was kept constant at 1 mW.

To reaffirm that the signal changes observed from the photodiode are due to the TE PWV shift of the surface PC filter, the transmission pump/probe setup was also used to monitor the temporal response. Since the TE PWV blue-shifts from a longer wavelength to a shorter wavelength, the HeNe laser's incident angle relative to the surface PC filter was initially aligned so that the initial TE PWV at that incident angle was at a longer wavelength than λ=632.8 nm. Simultaneously, the incident angle was aligned such that the final TE PWV, after optical tuning, would be at a shorter wavelength than λ=632.8 nm. The pulse energy was set to a value of 4 mJ/pulse, so that small changes in the RI would occur due to each pulse along with corresponding small shifts in the TE PWV causing the PWV of the device to shift from a wavelength longer than λ=632.8 nm to shorter than λ=632.8 nm. Changes in the HeNe transmission signal should follow the varying transmission efficiency of TE resonance peak across its line width as it shifts through λ=632.8 nm. The results agree with this and can be seen in Fig. 2.15. The transmission signal decreases to a minimum value as the TE PWV shifts to exactly λ=632.8 nm. As the TE PWV continues to shift to shorter wavelengths than λ=632.8 nm,

the transmission signal starts to increase again. This dip in the transmission signal should have a Lorentzian shape since the resonance reflection peak of the surface PC filter is also Lorentzian, and the TE PWV shift is small enough to sufficiently sample the resonance peak. The data points from the plot were fitted, using Origin, to a Lorentzian with a R^2 value of above 0.99. This supports the fact that the transmission signal sampled the TE PWV resonance peak as it shifted through λ=632.8 nm, and that the transmitted probe signal variation is a result of the TE PWV shift.

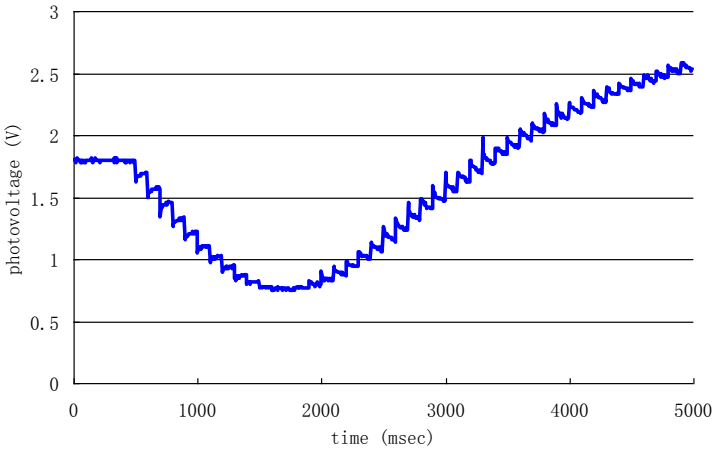

Figure 2.15 Transmission pump probe result showing the probe intensity decreasing to a minimum when the PWV is at 632 nm and increasing as the PWV is tuned past 632 nm.

When the pump source is increased to higher energy pulses, this Lorentzian line shape disappears because the PWV shift is too large to sufficiently sample. The transmission pump/probe setup is used again to observe the temporal response of the 1D surface PC filter, but the pump pulse energy is increased to 17 mJ/pulse at 10 Hz output. Also, the incident angle of the HeNe laser relative to the surface PC filter is realigned so that the TE PWV is tuned to a final value of λ=632.8 nm. The result is that the TE PWV shifts to λ=632.8 nm by four pulses from the Nd:YAG laser as shown in Fig. 2.16. After four pulses, the transmitted signal remains constant since the azobenzene molecules are all excited into their *cis* state. No more changes in

the RI and shifts of the TE PWV occur. Blocking of the probe beam has been achieved. It may be possible to have the TE PWV shift completely with one pulse by increasing the pulse energy, but the Nd:YAG laser did not have high enough pulse energy to observe this effect. Also, one would have to consider mechanical and thermal damage to the device from such high energy pulses from the pump source. Comparing Figs. 2.12 and 2.16, it is seen that the total TE PWV shift is accomplished with three and four pulses, respectively, with the same pump energy of 17mJ/pulse. This is a slight discrepancy, and can be attributed to small differences in the thickness of the azo-LC layer in the different surface PC filters and to slight variations in the pulse energy from the pump source. Still, both results are in the same order of magnitude.

The time response from the pulsed laser pump source was on the order of microseconds as seen on the oscilloscope screen capture from Fig. 2.17, which is a close-up view of the up transition in the transmitted probe signal due to the tuning of the TE PWV. This is much faster than the time response of the eye's blink reflex, which is on the order of hundreds of milliseconds. Therefore, the tuning of the TE PWV is sufficiently fast in responding to the target wavelength more quickly than the human eye. In fact, the limiting factor of the time response for a surface PC filter is the time it takes to excite the surface PC leaky mode and set up an optical resonance to destructively interfere with the fields on the transmitted side of the surface PC. This process occurs on the order of femtoseconds as simulated using FDTD. Thus, the surface PC filter can potentially be used for fast optical tuning, given sufficiently fast time response of the optically active material.

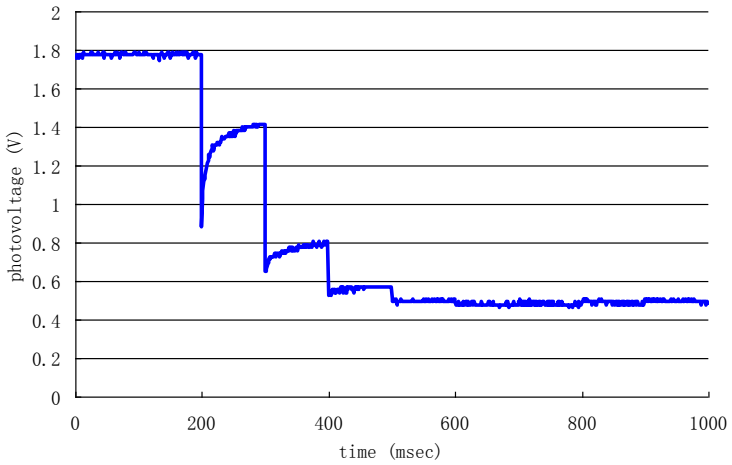

Figure 2.16 Transmission pump probe result using a high pump energy of 17 mJ/pulse. Each pulse causes a rapid decrease of the transmitted probe signal due to tuning of the PWV. After 4 pulses, the PWV has shifted to 632 nm and is stable at this final value to block the incident probe beam.

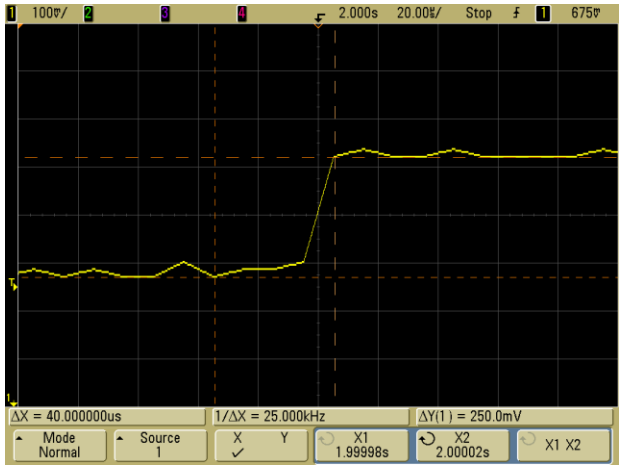

Figure 2.17 Reflection pump probe signal. An oscilloscope capture of the probe intensity increasing as a result of the response from the pump laser is zoomed in on the transition. The time response is estimated to be on the order of 40 μs.

2.6 Fabrication of Optically Tunable 2D Photonic Crystal Filters

The device fabrication utilizes a nanoreplica molding process that requires the use of a silicon "master" wafer as a molding template [9, 40, 41]. The silicon master is a 6-inch diameter wafer upon which a 2D square lattice of posts with a period of Λ=300 nm and a 50% duty cycle was patterned by deep-UV photolithography (North Carolina State University Nanofabrication Facility). The pattern is etched into the silicon wafer to a depth of d=150 nm by reactive ion etching to produce a 2D square lattice of posts. The silicon master is then used to replicate its

nanostructures onto a target substrate. To do this, a layer of liquid acrylate UV-cured polymer (UVCP) was drop-coated on top of the silicon master. A flexible polyethylene terephthalate (PET) substrate is then placed over the silicon master, and is next pressed into contact with the master using a rolling cylinder. This enables the UVCP drops to form a thin continuous layer between the two surfaces and conform to the features of the master. The UVCP is cured to a solid film by exposure to a high intensity UV lamp for 90 seconds. Next, the PET substrate is peeled away from the master, resulting in a cured UVCP layer with a square lattice of holes, period of Λ=300 nm, and duty cycle of 50% that is replicated onto the PET substrate. Figs. 2.18 and 2.19 show SEM images of the 2D surface PC silicon master and the 2D surface PC UVCP nanoreplica, respectively. Even for 2D patterns and small nanostructures, the nanoreplica molding process is uniform over large areas and contains few defects. In order to produce a surface PC filter that produces resonant optical reflection, a high refractive index thin film must be deposited over the low refractive index (n=1.46) replica-molded grating structure. Sputter-deposited thin films of approximately t=54 nm of titanium dioxide (TiO_2), with refractive index of n=2.42 at λ=532 nm, served as the high refractive index layer. This thickness of TiO_2 was used in order to achieve a TE PWV at λ=532 nm for the 2D surface PC filter. Another PET substrate was used as a cover layer. A polyimide (PI), PI-2556 (HD Microsystems), film is spin-coated on the PET substrate and then baked and rubbed with a velvet cloth to pre-align the LC parallel the rubbing direction. To finish fabricating the device, the cover layer and the surface PC layer were combined to form a cavity, with the azo-LC injected in between the cover and surface PC layers, enabling the azo-LC to spread due to capillary forces. The 2D surface PC and the PI rubbing direction were assembled such that the LC molecules would align in one of the directions of the periodicity. The cover and grating layers were clamped together between two

microscope glass slides for structural support. Since there are no spacers to define a gap in this device, the capillary forces of the liquid crystal define the thickness of the resulting layer, and it is estimated to be about a few micrometers thick. The parameters for this structure are shown in Fig. 2.20.

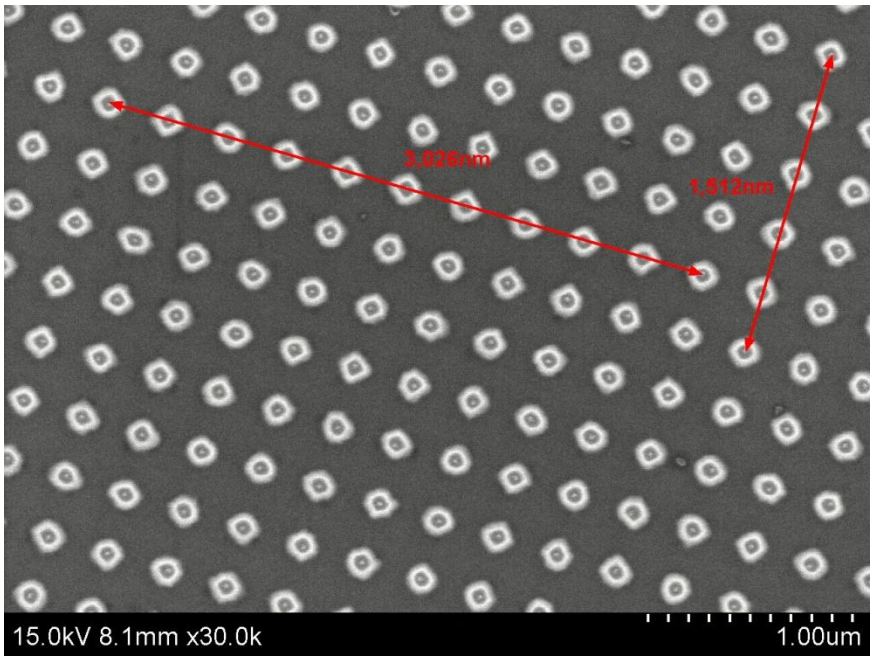

Figure 2.18 SEM image of the silicon master used for nanoreplica molding of a 2D surface PC reflection filter.

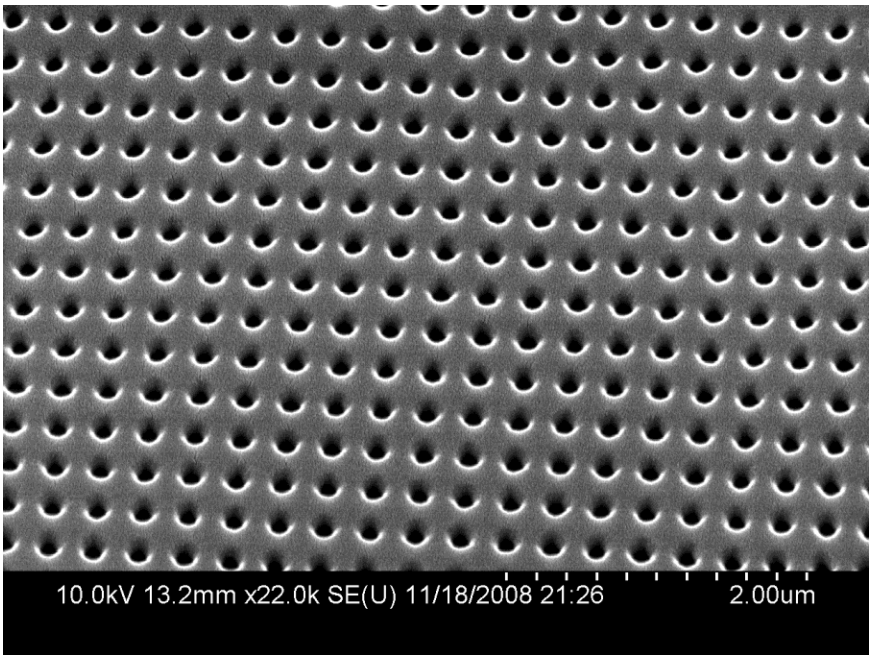

Figure 2.19 SEM image of the UVCP nanoreplica after molding from the silicon master. Since the silicon is a square lattice of posts, this results in a complementary square lattice of holes in the UVCP nanoreplica.

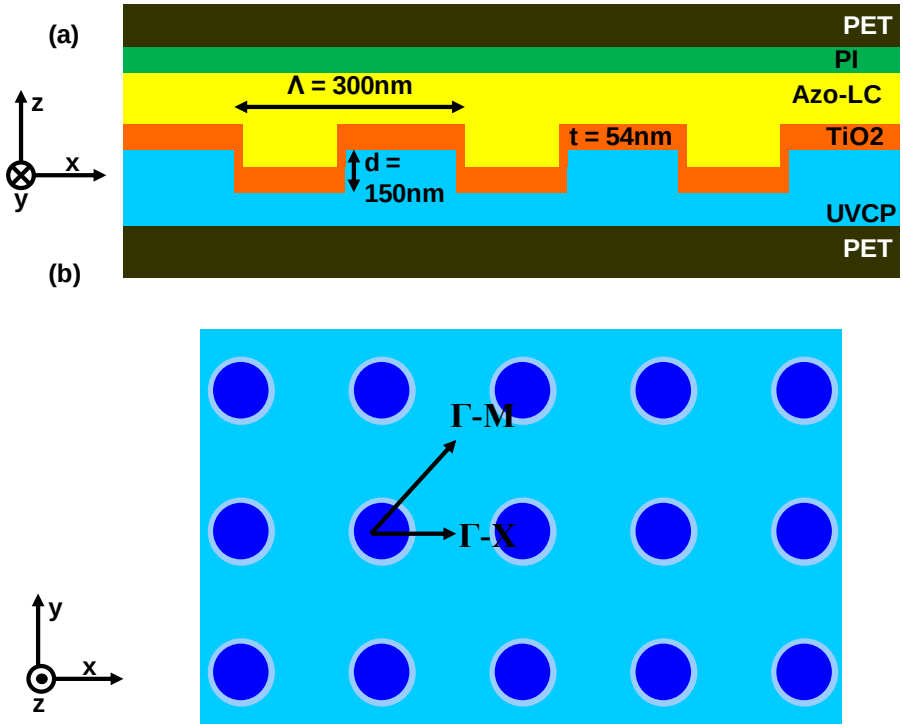

Figure 2.20 (a) Side view cross section of a 2D surface PC filter with azo-LC molecules incorporated as an optically tunable layer. The TiO_2 thickness is t=54 nm, the period is Λ=300 nm, and the modulation depth is d=150 nm. (b) A top view cross section of the device showing the square lattice of holes of the 2D surface PC. Incident angles in the Γ-M and Γ-X directions are defined in the figure.

2.7 Temporal and Spectral Response of Optically Tunable 2D Photonic Crystal at 532 nm

The optically active material used was the azo-LC with industry name LC1005. The azo-LC molecules aligned themselves parallel to the photonic crystal surface, and along one of the principal axes of the photonic crystal (in either the *x* or *y* direction as defined in Fig. 2.20). The rubbed PI film homogeneously aligns the director of the azo-LC parallel to the rubbing direction and parallel to the surface of the PI film. Rubbing the PI film reorients the backbone of its long polymer chains parallel to the rubbing direction and also creates physical grooves on the surface of the PI film. These long molecular backbones interact with the LC molecules through Van der Waals forces and induce preferred LC alignment parallel to the rubbing direction. The grooves on the surface of the PI film also aid in alignment of the LC in the same direction. This minimizes the energy state of the LC, and this type of alignment is called homogeneous alignment.

This is evident from observing the TE PWV of the surface PC transmission spectrum. In the ground state, the liquid crystal molecules are in the *trans* configuration and thus have an anisotropic refractive index along their short and long axis. For an isotropic RI material, the 2D surface PC filter is polarization independent for normal incident light. The anisotropic RI of the azo-LC breaks the symmetry of the 2D surface PC and results in a polarization dependent TE PWV, even at normal incidence. The TE leaky modes have electric fields in both the *x* and *y* directions due to the unpolarized incident light and the 2D nature of the surface PC. Thus at normal incidence, the TE modes will have two different PWVs resulting from the alignment of the azo-LC. If the TE mode's polarization is along the short (long) axis of the azo-LC molecules, then the PWV is at a shorter (longer) wavelength value. This occurs since the long axis of the azo-LC molecules has a higher RI value than the short axis. Fig. 2.21 experimentally confirms this result for a 2D surface PC filter with *trans* state of the azo-LC molecules (blue

curve). The transmission spectrum of the 2D surface PC is obtained using the transmission pump/probe setup in Fig. 2.11(a). There is a TE mode with PWV at λ=524 nm and another TE mode with PWV at λ=556 nm due to the anisotropic RI of the azo-LC *trans* isomer.

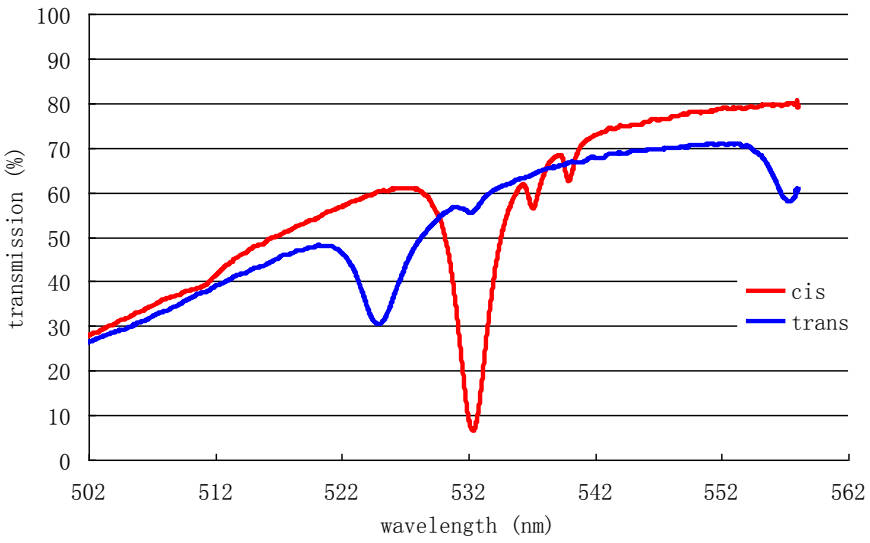

Figure 2.21 Transmission spectrum of a 2D tunable photonic crystal before (blue) and after (red) tuning with a Nd:YAG laser. The two initial PWV tune to become one polarization independent PWV at 532 nm.

An isotropic orientation of the azo-LC on the photonic crystal surface will result in an isotropic refractive index for the azo-LC layer and lead to a polarization independent TE PWV. The fact that this is not observed in the transmission spectrum supports the fact that the liquid crystal molecules are aligned homogeneously in either the *x* or *y* direction of the 2D surface PC.

Since the TE PWV is polarization dependent in the *trans* state, the maximum transmission efficiency is 50% for each of the individual TE PWV for unpolarized incident light. This is advantageous since it improves the visibility through the surface PC filter at these initial wavelengths which the surface PC filter is not meant to optically limit. Once the azo-LC molecules are excited into the *cis* state by an optical pump source at λ=532 nm, the bulk RI of the liquid crystal layer decreases and becomes isotropic in nature. Thus, the 2D surface PC filter regains its polarization independent response at normal incidence with the TE PWV shifting to a

new value. The shorter wavelength TE PWV will red-shift and the longer wavelength TE PWV will blue-shift to the same value of λ=532 nm. Since the RI change from the *trans* (short-axis) to *cis* configuration ($\Delta n = n_{cis} - n_{\perp} = +0.078$) is less than the RI change from the *trans* (long-axis) to *cis* configuration ($\Delta n = n_{cis} - n_{\parallel} = -0.156$), the red shift of the lower PWV (ΔPWV = 7.48 nm) is less than the blue shift of the higher PWV (ΔPWV = 24.97 nm). The experimental data in Fig. 2.21 is consistent with theory. The red curve is the transmission spectrum of the 2D surface PC filter after the azo-LC molecules have been excited into the *cis* state the pump laser. The transmission efficiency of the TE PWV at λ=532 nm can reach 0% in theory, but is limited by practical considerations and is approximately 8% for the particular device in Fig. 2.21.

The time response of the 2D PC was investigated using a transmission pump/probe setup similar to Fig. 2.11(b) except that the HeNe probe laser was replaced with a 4 mW CW diode pumped solid state laser at λ=532 nm. Thus, both pump and probe light sources are at the same wavelength. The transmitted light from the probe laser was detected with a silicon photodetector. This makes it difficult to separate the effects of the probe and pump lasers since the probe laser will cause the TE PWV to shift even in the absence of the pump. In addition, a bandpass filter cannot be used to separate the probe signal from the pump signal since they are at the same wavelength. Thus, it is possible that light from the Nd:YAG laser is detected by the photodetector. With this in mind, the probe beam power was decreased to a minimum value and the Si photodiode gain was increased in order to keep the signal within the linear range of the silicon photodetector. Also, the pump laser energy was increased to a maximum value of 17 mJ/pulse. This way, the tuning effect of the probe laser would be minimized while the tuning effect of the pump laser would be maximized. Even with these settings, the results show that the probe laser still shifts the TE PWV towards λ=532 nm as shown in Fig. 2.22. This depicts the

transmission signal of only the probe laser being incident on the 2D surface PC filter. The transmission signal decreases since the TE PWV is shifting to λ=532 nm. With both pump and probe lasers incident on the 2D surface PC filter, the transmitted probe signal is shown Fig. 2.23. A continuous shift of the TE PWV is seen from the CW probe laser since the transmission signal is continuously decreasing. Much faster and discrete TE PWV shifts are seen as a result of the high energy pulses from the pump laser as observed in the sharp decreases in the transmission signal following the 10 Hz rate of the pump laser. In practical applications, only one light source at λ=532 nm is present, and the 2D surface PC filter is designed to optically limit this single incident light source whether it is CW or pulsed. In this sense, the 2D surface PC filter accomplishes that task. It was for the purpose of characterizing the time response of the 2D surface PC filter that the transmission pump/probe setup was used.

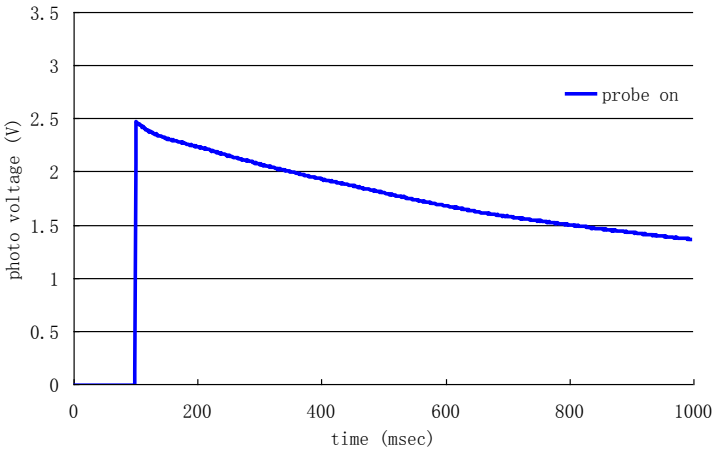

Figure 2.22 Transmission pump probe signal from exposure to only the probe beam. Tuning of the PWV is seen even with the pump beam turned off.

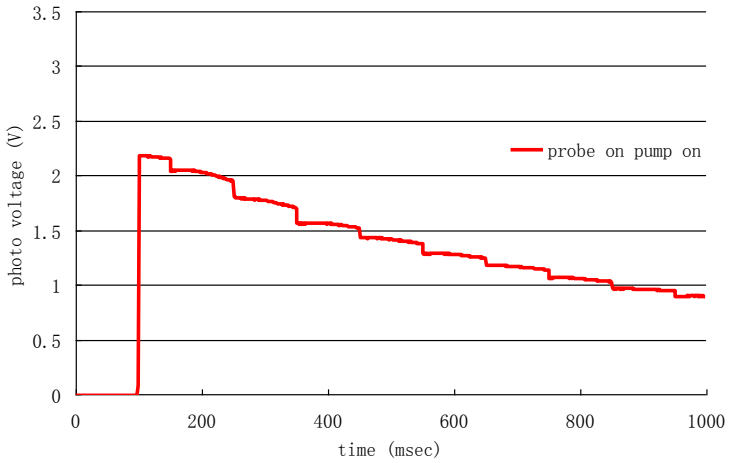

Figure 2.23 Transmission pump probe signal with both probe beam and pump beam turned on.

CHAPTER 3 TWO-DIMENSIONAL PHOTONIC CRYSTAL STACK FILTERS

3.1 Motivation

Reflectance filters based upon anomalous optical resonances that occur within certain periodic surface structures represent a class of devices that can, in theory, provide 100% reflection efficiency at a resonant wavelength. By selection of the grating period, the grating depth, the refractive index (RI) of the materials used in fabrication, and the thickness of dielectric thin films, resonance wavelengths can be engineered over a wide spectral range from UV [42, 43] to IR [11, 12, 14, 44-46]. Such devices, referred to as guided-mode resonance filters (GMRF), surface photonic crystals (PC), or PC slabs, are especially attractive as filters because they exhibit bandwidth and reflection efficiency that are similar to multilayer distributed Bragg reflectance (DBR) filters, but can be fabricated using a 1D or 2D surface grating structure combined with a single RI thin film deposition [40, 41, 47]. However, the period of the PC must be substantially less than the free-space wavelength of the filtered light, providing a challenge to inexpensive fabrication approaches, particularly for producing large device areas for visible wavelength applications. Recently, plastic-based nanoreplica molding has been applied to produce surface PC filters that enable production upon flexible sheets of plastic film in continuous rolls for application as optical biosensors [8-10].

Optical filters for protection of eyes or sensors are based on either absorption [25] or reflection [24] of incident laser radiation. For laser eye protection, the wavelengths of interest span from visible to near-IR, while protection of optical sensors used for thermal imaging and night vision are concerned with mid-IR wavelengths. Important parameters for these optical filters are optical density (OD), visible light transmission (VLT), and angular tolerance. OD is a quantitative measure of transmitted light based on a log scale, $OD = -log_{10}(T/T_0)$, where T_0 and T are the incident and transmitted light intensities, respectively. The American National

Standards Institute (ANSI) regulates the required OD for different applications and environments in order to maintain laser irradiation below maximum permissible exposure (MPE) levels when entering the human eye. These standards are regulated under the ANSI Z136 series. For example, OD = 3 is required to attenuate a continuous wave (CW) laser beam of 2 mW/cm^2 to an transmitted intensity of 2 $\mu W/cm^2$, which is the maximum permissible exposure of the human retina to a green laser (λ=532 nm).

Although computer models predict the possibility of 100% reflection efficiency for PC-based filters at their resonant wavelength [44, 48], in practice, surface PC filters do not generally fully achieve this level of performance due to several factors. Materials used for PC fabrication may have low levels of optical absorption at the resonant wavelength that reduce resonance efficiency, the device period or duty cycle may be slightly imperfect over the illuminated area, and nanometer-scale defects (such as particulate and voids) may contribute to suboptimal behavior that is not well-modeled. Nonetheless, experimental demonstrations of surface PC filters routinely achieve reflection efficiencies in the range of 90-99% [40-42, 49]. Liu et al. demonstrated a filter with reflection efficiency of 98% at λ = 860 nm fabricated on fused silica substrate. Therefore, one potential approach for obtaining OD greater than unity would be to integrate multiple surface PC filters onto a single substrate into a vertical stack, in which each layer of the stack reflects a substantial fraction of the light at a desired wavelength. Integrating multiple surface PC filters into a layered stack may also be used to broaden the angular full width at half maximum (FWHM) of the system, in order to improve the angle tolerance of the device. This work presents the design, fabrication, and characterization of an integrated 2D PC stack filter with improved optical density and angular tolerance, designed to efficiently reflect a λ=532 nm laser. A 2-dimensional grating structure was selected so the reflectance response

would be independent of incident light polarization for normal incidence. Also, compared to a DBR structure, this design can achieve similar OD while requiring substantially fewer thin film deposition steps, allowing a simpler and less expensive fabrication route for manufacturing optical limiting filters over large surface areas on flexible plastic materials. Precise fabrication of PC filter layers with identical resonant wavelength is enabled through the use of an *in-situ* monitoring technique for measuring the resonant reflection peak during dielectric thin film deposition. This work represents, to the authors' knowledge, the first report of an experimentally demonstrated stacked PC filter used to obtain increased optical density (for a wavelength in the visible region of the spectrum). We show that stacking of PC filters can indeed be used to increase OD, but that each additional PC in the stack provides a diminished OD improvement due to lack of perfect collimation of the incident light source.

3.2 Fabrication of 2D Photonic Crystal Stack Filters

The device fabrication utilizes a nanoreplica molding process that requires the use of a silicon "master" wafer as a molding template [9, 40, 41]. The silicon master is a 6-inch diameter wafer upon which a 2D square lattice of posts with a period of Λ=300 nm and a 50% duty cycle was patterned by deep-UV photolithography (North Carolina State University Nanofabrication Facility). The pattern is etched into the silicon wafer to a depth of d=150 nm by reactive ion etching to produce a 2D square lattice of posts. The silicon master is then used to replicate its nanostructures onto a target substrate. To do this, a layer of liquid acrylate UV-cured polymer (UVCP) was drop-coated on top of the silicon master. A flexible polyethylene terephthalate (PET) substrate is then placed over the silicon master, and is next pressed into contact with the master using a rolling cylinder. This enables the UVCP drops to form a thin continuous layer between the two surfaces and conform to the features of the master. The UVCP is cured to a

solid film by exposure to a high intensity UV lamp for 90 seconds. Next, the PET substrate is peeled away from the master, resulting in a cured UVCP layer with a square lattice of holes, period of Λ=300 nm, and duty cycle of 50% that is replicated onto the PET substrate. A SEM image of a UVCP nanoreplica mold is shown in Fig. 3.1(a) illustrating high integrity of the mold with few defects over many periods. An atomic force microscope (AFM) surface profile of the nanoreplica mold validates the PC period of Λ=300 nm in Fig. 3.1(b). The depth of the holes is close to d=150 nm, but due to convolution with the AFM tip, it was not possible accurately determine the hole depth. The entire grating area produced by this method is 5x8 cm^2 for the devices described here.

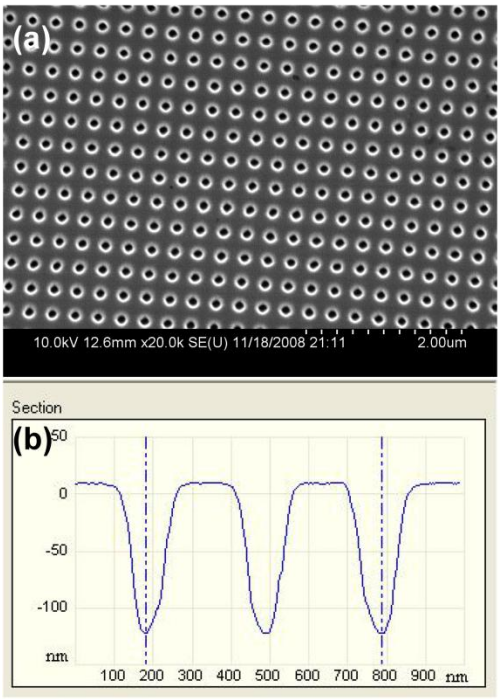

Figure 3.1 (a) SEM view of the nanoreplica mold from a 2D square lattice photonic crystal silicon master. The master is comprised of posts resulting in a nanoreplica mold of 2D square lattice of holes. (b) AFM section view of nanoreplica mold showing a period of Λ=300 nm and hole depth of approximately d=150 nm.

In order to produce a surface PC filter that produces resonant optical reflection, a high RI thin film must be deposited over the low RI (n=1.46) replica-molded grating structure. Here, sputter-deposited thin films of titanium dioxide (TiO_2), with RI of n~2.42 at λ=532 nm, served as the high RI layer. In order to stack another layer on top of the first surface PC filter, a second nanoreplica molding step is performed on top of the TiO_2 layer, which produces an additional UVCP mold of 2D square lattice of holes. The replica molding/TiO_2 sequence may be repeated to generate a stack of surface PC filters with several layers, and stacks with N=2 PCs and N=3 PCs are demonstrated in this work. Fig. 3.2(a) shows the cross section schematic for a filter consisting of 3 PCs and Fig. 3.2(b) is a top view of the same device structure. The thickness of the UVCP layers that are sandwiched between the TiO_2 films is ~5 nm, substantially greater than the designed resonant wavelength. Because the individual PC layers are separated by a substantially large gap (compared to the resonant wavelength), there is no mode coupling between PC layers, and each layer behaves as an independent filter. Therefore, there is no requirement for tight tolerance for the thickness of the UVCP layer, and there is no requirement for lateral alignment of upper PC filters to the filters beneath them. In order to validate that integrated surface PC filters operate independently, we also measured the reflectivity performance of stacked surface PCs that are individually fabricated upon separate substrates, and then characterized in series with ~8 cm gaps between each filter.

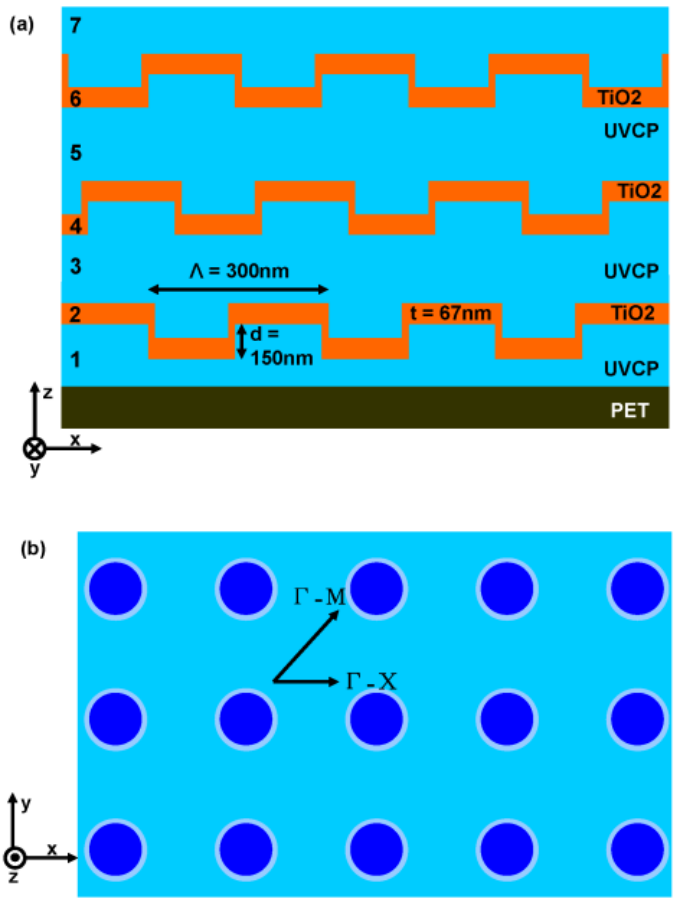

Figure 3.2 (a) Cross section schematic view of a 3 PC stack filter with 300 nm period, hole depth of 150 nm, and TiO_2 thickness of 67 nm. A single filter would consist of layers 1, 2, and 3 in the schematic. The schematic cross section is not to scale, as the UVCP layers (layers 1, 3, and 5) are each ~5 μm thick, and the PET substrate is ~250 μm thick . (b) Top view of the 2D PC filter with corresponding directions of the Brillouin zone with respect to the lattice vectors.

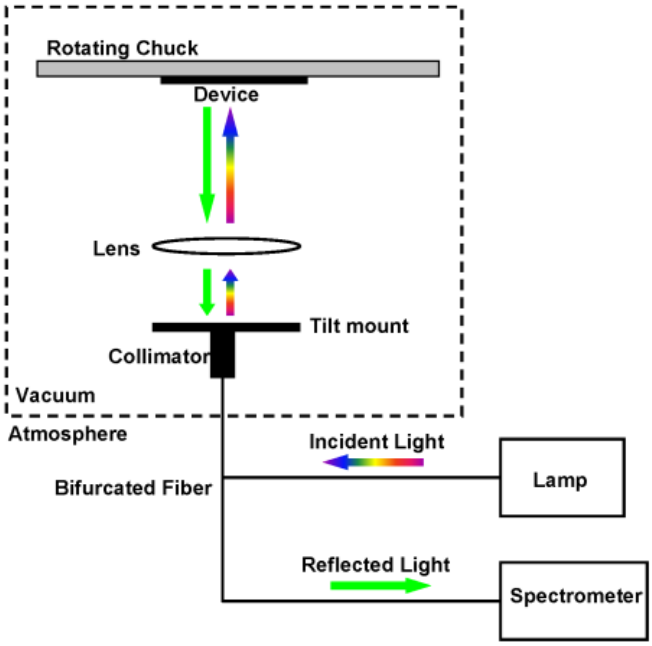

Figure 3.3 Schematic of the *in situ* reflection spectrum monitoring system. The low vacuum environment is inside the dashed box. In one leg of the bifurcated optical fiber, incident light is illuminated onto the device through a collimator and lens optical system. The reflected light is collected through the same optics and sent to the other leg of the optical fiber, where it is measured with a spectrometer.

We refer to the resonant wavelength of a surface PC filter when illuminated with normal incident light as the center wavelength. The center wavelength depends on the parameters of the PC structure such as the period, hole depth, hole diameter, TiO_2 thickness, and the RI of the UVCP and TiO_2 layers. Since a silicon master is used for nanoreplica molding, most of these parameters are fixed, and the main variable in fabrication of the PC filters is the TiO_2 thickness.

In order to produce PCs in the stack that have identical center wavelengths (λ=532 nm), strict control of the TiO_2 thin film thickness is required for each deposition. For this purpose, an *in situ* monitoring system was developed to monitor, in real time, the reflection spectrum of the PC filter while depositing TiO_2 in a sputtering chamber (see Fig. 3.3). Thus, the center wavelength was observed during the sputtering process and the process was stopped when it reached a desired value in a vacuum environment (λ=505.39 nm). This "vacuum" center wavelength

would result in λ=532 nm, after the TiO_2 film is overcoated with a UVCP layer. The monitoring system consists of a custom made bifurcated multi-mode optical fiber that includes an in-line vacuum feed through conflat flange in the sputter deposition chamber. The vacuum feed-through allowed interfacing between inside and outside of the vacuum chamber. Inside the chamber, broadband light was illuminated through one optical fiber coupled to a collimator. An additional lens was placed in order to refocus the light before it was incident onto the PC filter. The PC filter is mounted on a chuck that rotates during sputtering. The reflected light was collected through the same collimator and into the other optical fiber. Outside of the vacuum chamber, a tungsten halogen lamp was connected to one leg of the bifurcated cable to supply incident light, while the other leg was connected to a spectrometer (Ocean Optics) to acquire the reflection spectrum of the device during TiO_2 sputter deposition. Using this monitoring setup, it was possible to control the center wavelength among different PC filters in the stack to within $\Delta\lambda$ =1 nm.

3.3 Improved Optical Density and Angular Tolerance in 2D Photonic Crystal Stack Filter

The devices were characterized using a transmission setup, as depicted in Fig. 3.4, using broadband incident light from a tungsten halogen lamp coupled to a fiber optic cable. The incident light was unpolarized and collected on the transmitted side using another fiber optic cable which was connected to a spectrometer. The spectrometer output was observed using commercial software from Ocean Optics. The PC filters were mounted on a rotating stage which allowed adjustment of the angle of incident light in the *xz* plane as referenced in Fig. 3.2(a). Also, the PC filter was attached to a tilt mount which enabled adjusting the filter to normal incidence with respect to the incoming light.

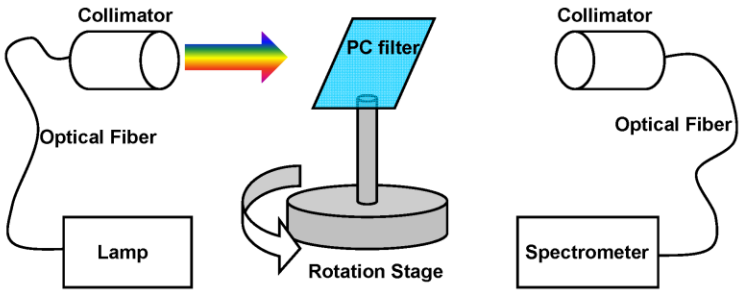

Figure 3.4 Setup used to acquire the transmission spectrum of the PC stack filter during different stages of the fabrication process. Broadband light from a tungsten halogen lamp is incident on the device and the transmitted light is collected and analyzed using a spectrometer.

The first device tested was a 3 PC stack filter with each PC filter in the stack having a center wavelength of λ=532 nm. This was achieved by depositing approximately 67 nm of TiO_2 for all 3 PCs. The goal of this design is to increase the OD of the PC filter at the target wavelength as the number of PC layers increases. Ideally, the OD of the overall filter should scale linearly with the number of PC filters as shown in Eq. 3.1:

$$OD_n = -log_{10}\left(\frac{T^n}{T_0}\right) = -n \cdot log_{10}\left(\frac{T}{T_0}\right) = -n \cdot OD_1 \tag{3.1}$$

where T^n is the transmission efficiency for a stacked device of *n* PC layers, and T_o is 100% transmission efficiency. The transmission spectrum at normal incidence was recorded during the fabrication process, after completion of each PC filter in the stack. The fabrication of subsequent PC filters resulted in increased OD at the target wavelength as seen on the transmission spectra in Fig. 3.5(a), increasing from OD=1.45 with a single PC filter to OD=2.24 with a 3 PC stack filter. This improvement shows that stacking PC filters is a feasible solution to improving the OD of PC filters.

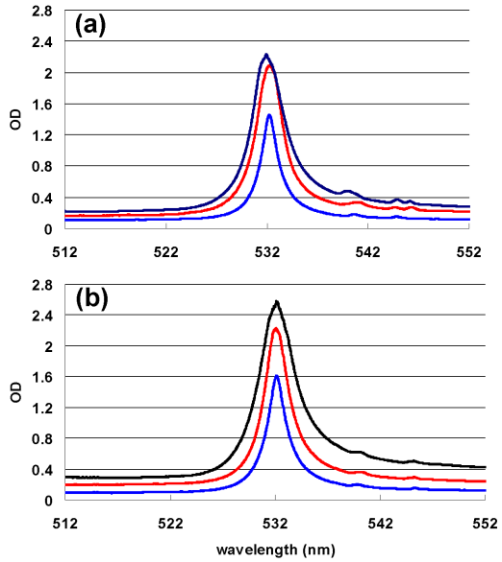

Figure 3.5 (a) OD spectrum of a PC stack filter during the fabrication process with the filter comprising N=1 (blue line), N=2 (red line), and N=3 (black line) PC filters. OD increases from 1.45 to 2.24 by stacking 3 PC filters. (b) OD spectrum of 3 discrete PC filters with 1 (blue line), 2 (red line), and 3 (black line) PC filters in the optical transmission pathway. The OD increases from 1.61 to 2.58.

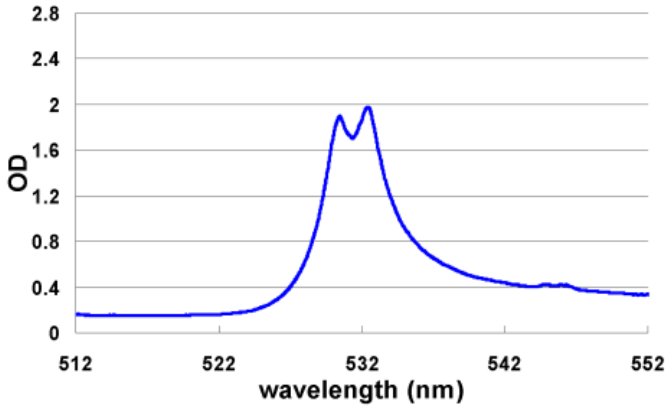

Figure 3.6 OD spectrum of a 2 PC stack filter. The center wavelengths of the two different layers are intentionally offset by 2 nm in order to increase the angular tolerance of the reflectance filter.

The second device tested was a 2 PC stack filter where the reflection peaks are offset at half width at half maximum (HWHM) apart; Fig. 3.6 shows the OD spectrum which depicts one peak at λ=530 nm and another at λ=532 nm. The wavelengths of the reflection peaks were controlled by depositing the appropriate amount of TiO_2 for each PC. This device was designed

to increase the angular tolerance of the PC filter by designing the OD spectrum to exhibit a broad and flat OD peak. A reference device with a single PC and reflection peak at the same wavelength was also fabricated for comparing angle tolerance. The transmission spectrum of the devices was recorded using the setup described above. A series of spectra was taken at different incident angles ranging from -10° to +10° at a resolution of 0.1°. Changing the incident angle of light changes the propagation constant and wavelength of the resonantly excited PC mode which produces the optical limiting effect. The optical resonances occur along the bands of the PC and are therefore a function of angle and wavelength. We were able to plot the band diagram of the PC filter along both Γ-X and Γ-M directions of the 2D square lattice PC, and it is shown in Fig. 3.7. These dispersion plots contain complete spectral and angular transmission spectrum of the devices. Taking a vertical slice through the band diagram results in a transmission spectrum over a range of wavelengths and at a single incident angle. By taking a horizontal slice through the band diagram, we observe the transmission spectrum over a range of angles at a single wavelength. At the center wavelength, the PC filter has an OD peak as a function of angle. The FWHM of this peak is a measure of the angular tolerance of the device. With this in mind, the angular transmission spectrum at the center wavelength was obtained for the 2 PC stack filter and a reference PC filter and plotted in Fig. 3.8. The angle tolerance of the 2 PC stack filter improved due to the increased angular FWHM from $\Delta\theta$=6.8° to $\Delta\theta$=9.1° in the Γ-M direction and from $\Delta\theta$=9.4° to $\Delta\theta$=14.8° in the Γ-X direction. The Γ-X FWHM is larger than the Γ-M FWHM due to the presence of a flat band which retains its guided mode resonance in the orthogonal plane to the incident plane.

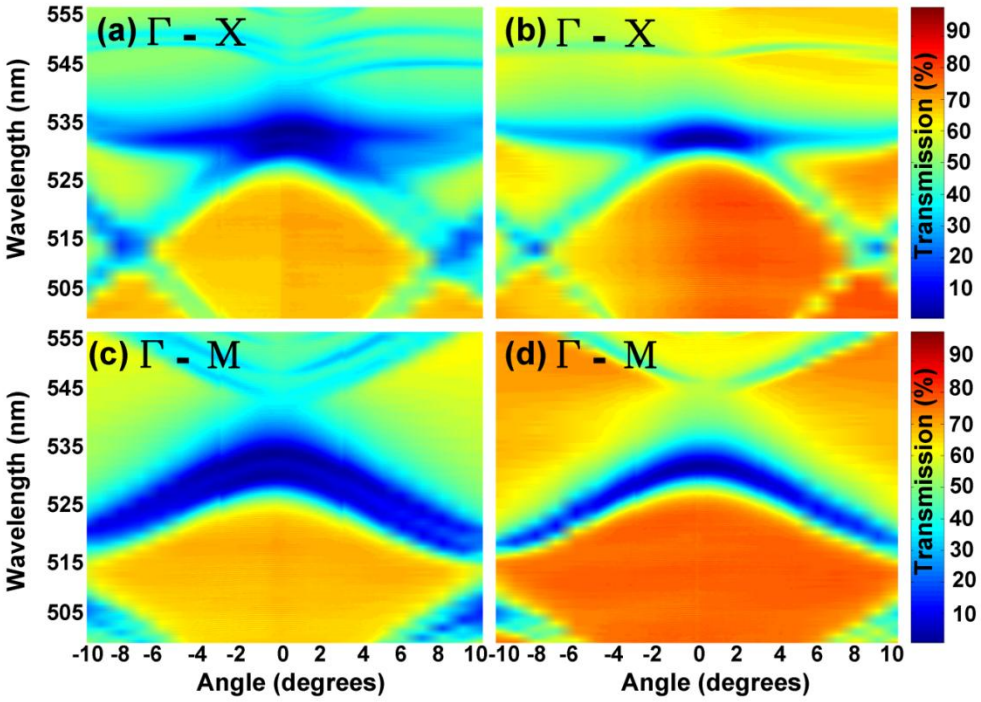

Figure 3.7 Band diagram of the 2D PC filter in the Γ-X (plots a & b) and Γ-M (plots c & d) directions. Color scale represents 0% transmission (blue) to 100% transmission (red). The Γ-X band diagram has a flat band effect that is clearly not seen in the Γ-M direction. The reference device (plots b & d) has smaller angular FWHM than the stack PC filter (plots a & c) due to its smaller resonance line width that is seen in the band diagram.

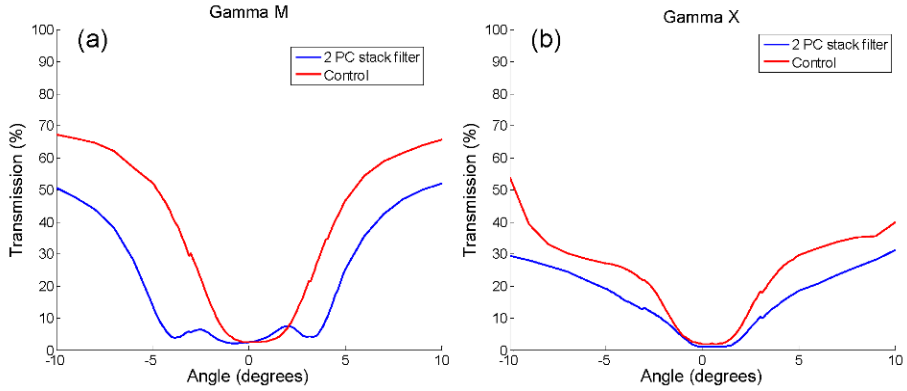

Figure 3.8 Angular transmission response of a 2 PC stack filter (blue) and control PC filter (red) at the center wavelength. (a) Γ-M direction response showing improved angular tolerance for the 2 PC stack filter. (b) Γ-X direction response showing improved angular tolerance for the 2 PC stack filter.

3.4 Limitations and Further Improvements to 2D Photonic Crystal Stack Filters

The PC stack filter was shown to increase its OD with each additional PC filter in the stack. However, it is evident that the increase in OD is not as dramatic as suggested by Eq. 3.1. One potential cause for the discrepancy between an ideal structure and the experimentally measured structure is that the center wavelengths among the PC filters do not match precisely, since they vary within $\Delta\lambda \sim 1$ nm due to slight differences between the sputtered TiO_2 thicknesses. The optical resonance has a spectral FWHM $\Delta\lambda \sim 5$ nm, so a mismatch of $\Delta\lambda \sim 1$ nm between center wavelengths will decrease the transmission efficiency appreciably. With perfect overlap, a filter comprised of 3 PC filters in series would achieve OD values closer to the values predicted by Eq. 3.1.

In order to investigate this issue further, three individual PC filters were fabricated on separate PET substrates. These filters have matching center wavelengths at $\lambda = 532$ nm. These 3 discrete PC filters were mounted individually on tilt mounts and placed in the transmission setup described earlier. The spacing between the PC filters was 8 cm. The transmission spectra of the filters were recorded with 1, 2, and 3 PC filters placed in the transmission path. Fig. 3.9 compares the theoretical and experimental OD increases as a function of number of PC filters in the stack. Using these separate PC filters, the result was similar to an integrated PC stack filter. Both cases show OD values less than predicted along with diminished increase in OD with each additional PC filter. Since both cases exhibit the same behavior, we can eliminate the possibility that optical coupling between PC filters is responsible for the observed reduced OD because the PC filters are separated by 8 cm. Also, Fabry-Perot effects can be eliminated from consideration since the spacing between PC filters was not designed as multiples of quarter or half wavelengths of the resonant light.

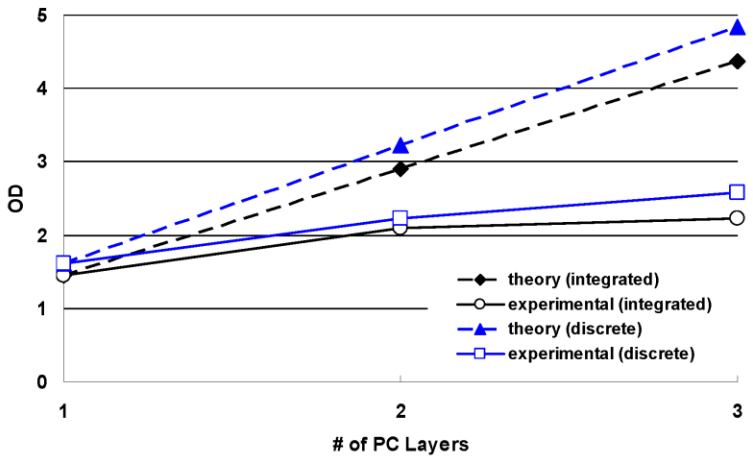

Figure 3.9 Comparison between theory and experimental data for increase in OD as a function of number of PC filters in a stack. The experimental results are lower than the predicted values and show a diminishing increase in OD with additional PC filters incorporated into the stack.

Using three discrete PC filters, we observed that the wavelength of light that was resonant with the first PC filter in the transmission setup was less efficiently blocked by the second and third PC filters. Fig. 3.10 shows the OD spectra of each PC filter in the series referenced to its incident light. The first PC blocked 97.5% of the incident light from the optical fiber, the second PC blocked 76% of its incident light (light passing through the first PC), and the third PC blocked 55% of its incident light (light passing through both the first and second PC). Therefore, when the three PC layers are designed to have the same center wavelength, each additional PC layer results in diminishing increases in OD. However, non-resonant light gave the same transmission efficiency for all three PC filters. The effect of diminishing increases in the OD can be explained as follows. In the computer model, the incident light is comprised of a perfect plane wave incident upon the PC at normal incidence, with no components at oblique incidence. The OD peak of a single PC filter has a limited angular FWHM when the response of the PC is plotted for transmission as a function of incident angle at the center wavelength. This is due to the optical resonance being a function of both wavelength and angle as mentioned previously. Additionally, the incident light is not a pure plane wave, but has a Gaussian mode

profile that can be represented by its angular wave spectrum [50]. The angular wave spectrum is the spatial Fourier representation of the wave front with the Fourier basis being plane waves in different propagation directions. Thus, a Gaussian mode profile can be deconstructed into its angular wave spectrum consisting of plane waves at different incident angles and amplitudes. At the center wavelength, the PC filter is able to efficiently block incident plane wave components that are nearest to normal incidence. This fact results in plane wave components which are oblique to be transmitted through the first PC filter and become incident on the second PC filter. These plane waves which are at the center wavelength but at oblique incidence to the second filter have higher transmission efficiency due to the limited angular tolerance of the PC filter. The result is that the second PC filter blocks less of its incident light than the first PC filter. The same argument holds when interpolating to the additional PC filters with each additional PC filter blocking less of its incident light than the PC filter before it. This is the most important reason why the experimental data deviates from theory, and places a limit on the number of PC filters that can be stacked effectively in practice.

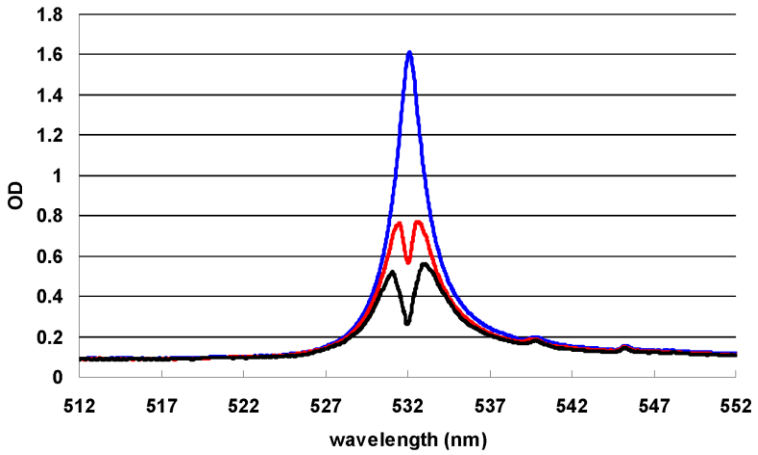

Figure 3.10 OD spectrum of a 2D PC filter when the incident has been transmitted through 0 (blue line), 1 (red line), and 2 (black line) PC filters before reaching the current PC filter.

One way to overcome the limitation of the stack PC filter is to increase its angular FWHM. This can be done by increasing the spectral FWHM of the stack PC filter by designing the different PC layers to have staggered center wavelength resulting in an effective resonance that is wider. This can be done by varying the TiO_2 thickness of each PC layer in order to obtain the desired center wavelengths. As Fig. 3.7 shows, a wider FWHM in wavelength corresponds to a broader FWHM in angle, increasing its angular tolerance. Also, it is possible to design the PC filter to have a flatter dispersion at the band edge which will increase the angular FWHM. The band edge corresponds to the center wavelength value. A flatter dispersion means that the optical resonance's wavelength does not vary as much as a function of angle, increasing the PC filter's angular tolerance at the center wavelength. This has been studied previously and it has been shown that optimizing the duty cycle of the PC to certain values can flatten the dispersion to improve angular tolerances of the PC filter in theory [51, 52].

The PC filter has a spectral FWHM $\Delta\lambda$~5 nm. This is an advantage over DBR stacks which typically have larger bandwidths for their stop bands. The PC filter can effectively block a narrow band of wavelengths around the center wavelength while transmitting a wider range of wavelengths in the visible spectrum. Thus, it is possible to maintain a sufficient level of visibility and color integrity while simultaneously optically limiting λ=532 nm wavelength light.

Another consideration is the effect of light which is not resonant with the 2D PC structure. Stacking PC filters results in large discontinuities of RI in the *z* direction as defined in Fig. 3.2(a), where each PC region effectively behaves as a thin film interference structure with a reflectivity that is wavelength dependent. As the number of PC filters increases, the number of layers of discontinuous refractive indices also increases, resulting in a highly complex reflection spectrum over a broad wavelength band. Because the UVCP layer thicknesses are not precisely

controlled, the multi-PC stack does not behave as a distributed Bragg reflector, although computer simulations show that bands of high and low reflection efficiency will form at wavelengths other than the resonant wavelength. These bands are undesirable since they reduce the transmission of light that does not couple into the 2D PC layers and should pass through the PC stack filter, and they are particularly undesirable if the bands fall within the visible spectrum, as they will reduce transmission efficiency for wavelengths other than the resonant wavelength, thus decreasing overall visibility through the filter.

When the PC layers are stacked by repeated nanoreplication steps, alignment between the principal axes of the 2D lattice is not strictly controlled among the multiple PC filters. For example, in Fig. 3.2(b) the Γ-X directions of the PC layers are not aligned. This has no effect on the transmission spectrum at normal incidence. The OD peak remains at the center wavelength at normal incidence regardless of the incoming light polarization since the 2D PC is symmetric in both *x* and *y* directions. However, at oblique incidence, the OD peak varies in wavelength when the angle is varied. This effect limits the angular tolerance of the PC filter. Careful design can result in improved performance. For a single PC filter, the dispersion in the Γ-X direction contains flat bands at the center wavelength as seen in Figs. 3.7(a) and 3.7(b) at the center wavelength of λ=532 nm. This behavior is not seen in the dispersion along the Γ-M direction. The flat band is beneficial because it allows the PC filter to maintain effective optical limiting at the center wavelength even at oblique incidence angles. When fabricating PC filters, offsetting each PC layer's principal axes relative to the others can maximize the effect of the flat band in as many directions as possible. In the case of two PC layers, the second PC layer should rotate its principal axis by 45º relative to the first PC layer, resulting in the Γ-X axis of the second PC layer lining up with the Γ-M axis of the first PC layer. Overlapping the Brillouin zones of the

PC layers in this manner would maximize the number of directions in the *xy* plane which exhibit the flat band. Thus, the angular tolerance of the filter can be improved even further.

3.5 Optically Tunable 2D Photonic Crystal Stack Filters

The OD of a single layer tunable 2D surface PC filter is practically limited by the same factors as the static 2D surface PC filter. However, additional optical loss due to the azo-LC molecule absorption at λ=532 nm reduces the OD even further. Thus, fabricating a stack of 2D surface PC filters can also be done to increase the OD. A schematic of the device cross section is shown in Fig. 3.11. The dimensions of the photonic crystal period Λ and modulation depth *d* are the same as in Fig. 3.2(a). Nanoreplica molding is used to fabricate the 2D surface PC on two PET substrates using UVCP as mentioned previously in section 2.5. A third PET substrate has the 2D surface PC nanoreplica molded on both of its sides. A thin film of t=54 nm TiO_2 is sputter-deposited on top of all four 2D surface PC layers. One azo-LC layer is shared by two surface PC which are facing each other and surrounding the azo-LC layer. Thus, a 4 layer 2D surface PC stack filter has two azo-LC layers.

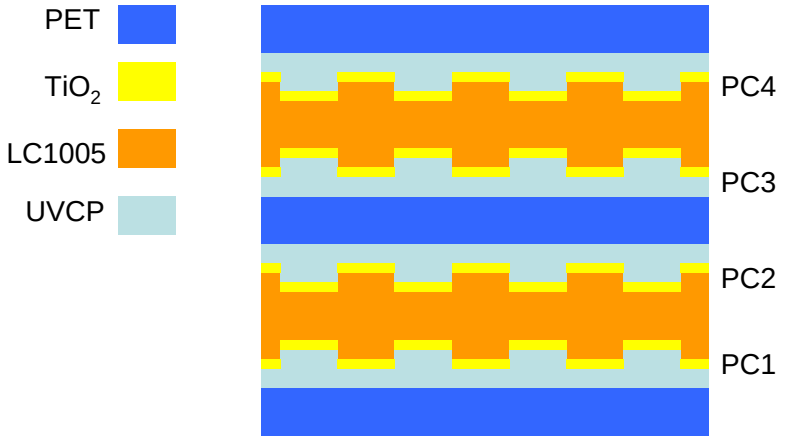

Figure 3.11 A cross section schematic of a 4 photonic crystal stack filter. Two tunable LC1005 layers are used for 4 photonic crystals.

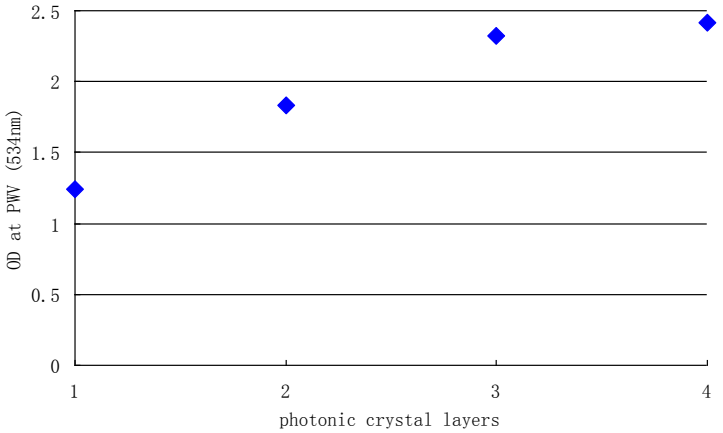

Figure 3.12 Increase in OD of a stack photonic crystal filter as a function of the number of photonic crystals in the stack. Increase from OD=1.24 to OD=2.42 is achieved by stacking 4 photonic crystals.

The transmission spectrum of the device was obtained as each 2D surface PC was added to the stack. The 2D surface PC filter was pumped with an Nd:YAG laser to excite the azo-LC molecules from *trans* to *cis*, and then the final TE PWV was measured. The OD at the TE PWV of the 2D surface PC stack filter was recorded as each additional 2D surface PC filter was added to the stack. Fig. 3.12 shows the results at the TE PWV of λ=534 nm. The PWV was off the target wavelength of λ=532 nm by λ=2 nm, but this can be corrected with a slightly thinner TiO_2 film. Going from a single surface PC to a 4 surface PC stack improved the OD from $OD = 1.24$ to $OD = 2.42$. Therefore, stacking of surface PC is an effective approach towards increasing the OD of a tunable surface PC filter in addition to a static surface PC filter. One drawback is that each additional azo-LC layer causes a reduction in transmission for wavelengths in the absorption spectrum of the azo-LC molecules. Thus, having too many azo-LC layers will decrease the visibility through the filter at these wavelengths. This places a practical limit on the number of photonic crystals that can be stacked. However, it is possible to reduce the thickness of each azo-LC layer to only around 200 nm so that high visibility is still maintained with

multiple azo-LC layers. The tunable PC stack filters fabricated in this work have azo-LC layers about micrometers thick.

Having multiple azo-LC layers does not pose a problem for tuning the TE PWV through RI change of the azo-LC molecules. The first azo-LC layer does not absorb so much of the pump light that the second layer cannot experience a RI change. Thus, both azo-LC layers are able to undergo *trans – cis* photo-isomerization and all 4 surface PCs experience a RI change and their TE PWVs all shift to the same value. Extrapolating this to multiple azo-LC layers, it will eventually come to the point that an azo-LC layer and all layers after it will not be able to undergo photo-isomerization due to the pump laser energy being absorbed by the preceding azo-LC layers. This is not a problem because this means that the pump laser has been attenuated enough that it was sufficiently blocked by the surface PC stack filter and azo-LC absorbing layers. Thus, this kind of device would have a self-limiting effect of shifting the TE PWV of only as many PC layers in the stack as required.

3.6 Conclusion

Integrated 2D PC filter stacks were fabricated using nanoreplica molding which enabled fabrication onto large area and flexible substrates. Improved OD at a target wavelength of λ=532 nm was demonstrated by designing a filter with three PCs in series with each PC having reflection peak at the same wavelength. Increased angle tolerance was achieved by designing a 2 PC stack filter with each PC having reflection peak wavelengths offset by approximately the HWHM. Both of these concepts can be combined onto a single substrate to create a high OD filter with improved angle tolerance. Further improvements to this approach were discussed including increasing the angular tolerance through optimization of the duty cycle of the PC and alignment between PC layers to take advantage of the flat bands in the 2D PC dispersion. In

principle, each PC in a vertical stack serves to increase the OD, but with diminishing improvement for each PC due to the low angular tolerance of a single PC combined with incident light that is not strictly comprised of collimated plane waves. By staggering the center wavelength through manipulation of the TiO_2 dielectric film thickness, greater angular tolerance is achieved, suggesting the possibility of using a substantially greater number of stacked PCs to obtain further increases in OD. Additionally, tunable 2D surface PC stack filters were fabricated which incorporate azo-LC as optically tunable material. The OD at λ=534 nm was improved from OD=1.24 to OD=2.42 with a 4 PC stack.

CHAPTER 4 QUANTUM DOT ENHANCED OPTICAL DOWN-CONVERSION USING SURFACE PHOTONIC CRYSTALS

4.1 Motivation

Modifying the emission characteristics of photon emitters in order to improve and tailor their performance for different applications is an ongoing field of study. The design of resonant cavities in order to either prohibit or promote emission at certain wavelengths is fundamental to many laser designs as well as for experimentally studying the fundamental physics of cavity quantum electrodynamics [53-58]. There are also many applications in sensor technology that take advantage of emission modification of fluorophores through engineering of the environment where the fluorophore is present. One such example is surface enhanced Raman spectroscopy [59-62]. In all of these cases, the engineering aspect comes in the purposeful design of the environment in which the photon emitter is located. It is advantageous to design photonic devices with cavity designs that can controllably modify the emission characteristic of optically active materials. Surface photonic crystals (PC) are practically realizable optical media which have a periodic variation in their refractive index in either 1D or 2D. In a way, surface PCs are distributed cavities which have certain resonant optical modes which can be supported within the surface PC structure. Through careful design of the surface PC geometry and optical properties, it is possible to design a surface PC with a desired band diagram that is advantageous for specific applications. Photonic crystals (PC) have been demonstrated to allow versatile control over optical properties of QD. Increasing the radiative emission rate [54], modifying the angular and spectral emission distribution [63, 64], and enhancing the emission intensity [3, 7, 64, 65] from QD have been shown. This work presents a PC enabled enhancement of optical down-conversion through enhanced excitation of λ=450 nm light and enhanced extraction of NIR light in the λ=800-900 nm range. Nanoreplica molding, which is compatible with large area and

flexible substrates, is used to fabricate the PC devices [40, 66]. This allows the PC devices discussed in this work to potentially be used for large area applications such as displays and photovoltaics. The ability to make devices on flexible substrates extends the potential applications over traditional fabrication methods such as photolithography and electron beam lithography. Additionally, nanoreplica molding has been incorporated into a roll-to-roll large scale manufacturing process of optical biosensors (SRU Biosystems).

4.2 Quantum Dots

Quantum dots (QDs) are nano-sized spherical particles of semiconductor or metallic material which have diameters ranging from 1 nm to 100 nm [67-69]. Controlling the size of a QD may lead to changes in its optical properties. For example, gold QDs of different sizes will appear different colors due to scattering of light through excitation of surface plasmon polaritons. The change in size of the gold QD will shift the surface plasmon resonance wavelength which gives the gold QD its color. Two main routes are used to fabricate QDs. First, solution based chemistry can be used to synthesize QDs from different chemical precursors. Second, chemical vapor deposition methods can be used to fabricate QDs on semiconductor wafers. Both methods usually produce QDs which cover a range of diameters centered at an average value. Because of their unique optical properties, QDs are now routinely incorporated into a broad range of photonic emitters and detectors including photoconductors [70, 71], solar cells [72, 73], LEDs [74, 75], and video displays [76, 77]. Semiconductor QDs are unique because their size determines the photon wavelength that is emitted. Due to the quantum confinement effect of the electronic wave function, QDs exhibit discrete electron energy levels which lead to narrow absorption and emission bands which are blue-shifted from their bulk counterparts. Varying the size and materials of the QD enables tuning of the emission and absorption wavelengths from the

ultraviolet (UV) to the near infrared (NIR). The electron and hole wave functions must satisfy the boundary conditions imposed by the QD confinement. Solving Schrödinger's equation, one finds that this confinement allows only discrete energy levels for the electrons and holes to occupy. The smaller the diameter of the QD, the stronger the confinement and the farther apart the allowed energy levels become. Thus, the ground state of the free electron and the ground state of the free hole have a wider energy gap. When the electron and hole recombine to emit a photon, this results in shorter wavelength (higher energy) photons emitted from smaller diameter QD. This work utilizes lead sulfide (PbS) QDs which emit in the NIR region of λ=700-900 nm.

4.3 2D Asymmetric Surface Photonic Crystal Incorporating Semiconductor Quantum Dots

A 2D asymmetric PC was designed and fabricated in order to modify the emission characteristics of colloidal lead sulfide (PbS) QD interacting with the PC environment. The PC was used to engineer the optical dispersion and spatial profile of optical modes supported within the PC structure through design of the PC period, modulation depth, duty cycle, and refractive index (RI). Moreover, optical modes which exist above the light line are leaky modes due to the fact that they can be coupled into and out of the PC through free space propagating waves enabled by phase matching through the PC. This coupling is strictly determined by the wavelength and incident/emission angle of the incoming/outgoing light [3]. In essence, the PC behaves as an optical antenna which redirects emitted light in a controlled direction. Therefore, it is possible to engineer the PC to efficiently extract light at desired wavelengths and emission angles. In addition, light of a particular wavelength and incident angle can be resonantly coupled into the PC structure in order to excite a PC mode with an electric field intensity much higher than the incident field. This occurs since the surface PC mode is a resonant mode that is bound within the PC structure and experiences constructive feedback within the distributed cavity. A

surface PC with a resonant reflection peak that has a narrower full width at half maximum (FWHM), or higher quality factor (Q factor), will excite a surface PC mode with a higher electric field intensity.

The emission and absorption characteristic of a semiconductor QD can be modeled as a two level system interacting with a sinusoidal time-varying perturbation. Eq. 4.1 is Fermi's golden rule which is a first order approximation using time dependent perturbation theory to solve Schrödinger's equation for such a case [78].

$$W_{12} = \frac{2\pi}{\hbar}|H'_{12}|^2\rho(\omega) \tag{4.1}$$

$$H'_{12} = \langle 2| - e\vec{r}\cdot\vec{E}(\vec{r},t)|1\rangle \tag{4.2}$$

First, both spatial overlap between the electric field and the QD and spectral overlap between the photon energy and the energy gap between the electron and hole energy levels are critical to efficient emission and absorption. In other words, the excitation photon needs to be within the absorption spectrum of the QD. Second, the absorption rate is proportional to the electric field intensity that is exciting the QD. Thus, an enhanced absorption rate is possible using a surface PC that couples the excitation light into the surface PC structure to excite the QD. Third, the emission rate of the QD is also critically dependent on the spatial and spectral overlap of the electric field with the QD. For spontaneous emission, the interacting electric field is the zero point energy electric field, that is, the electric field that is present for a particular optical mode when no photons are occupying that mode. The surface PC modifies the density of optical states in which the QD is able to emit a photon. Surface PC modes with a higher zero point energy and better spatial overlap with the QD will have higher emission rates into those modes. Thus, through design of the surface PC and engineering of its photonic band diagram, it is

possible to extract emitted photons from the QD into surface PC leaky modes which can efficiently couple out to free space.

1D PCs and symmetric 2D PCs are limited in the achievable wavelength separation of their leaky modes. In order to design a PC with simultaneous leaky modes at $\lambda = 450$ nm and $\lambda =$ 800-900 nm, it is not enough to design a PC using higher order modes and different polarizations to achieve leaky modes across this wavelength range. Thus, an asymmetric 2D PC design was chosen as a solution to overcome this limitation. Through the enhanced extraction and enhanced excitation effects, a 2D asymmetric PC with embedded PbS QD demonstrated enhanced efficiency of optical down-conversion from the blue to NIR wavelengths.

The 2D surface PC is designed asymmetrically such that the period of RI modulation differs in orthogonal directions. This design produces a 2D surface PC that behaves as two combined 1D surface PCs. The 2D surface PC design is shown in Fig. 4.1 and comprises a 2D rectangular lattice of holes that are d=130 nm deep. One direction of the surface PC has a period of Λ_2=220 nm with 50% duty cycle while the orthogonal direction has a period of Λ_1=520 nm with 60% duty cycle. A high RI region, with thickness t=100 nm, is surrounded by lower RI regions in order to support guided PC modes. The optical properties of the device are simulated using rigorous coupled wave analysis (DiffractMod, RSOFT) which provides solutions to Maxwell's equations for periodic structures. The simulation region comprises a single lattice of the PC structure with periodic boundary conditions in both *x* and *y* directions. The PC is a three layer structure with a high RI layer surrounded above and below by two low RI layers. A thermoplastic polymer was used as the low RI layer while the high RI layer was simulated as titanium dioxide (TiO_2). In order to take into account the material dispersion, the simulation was run with different RI values at $\lambda = 450$ nm and $\lambda =$ 800-900 nm. The RI values were obtained

from measurements of thin film samples of the corresponding materials using a variable angle spectroscopic spectrometer (J. A. Woollam). As mentioned above, leaky modes of the PC are coupled through free space incident light. It is known that this phenomenon results in resonant reflection peaks in the reflection spectrum of the incident light through the guided mode resonance effect [42, 44]. Moreover, varying the angle of incident light allows coupling to leaky modes of varying propagation constants through phase matching from the PC. As a result, the PC band diagram is obtained through measurement of the reflection of the PC as a function of both incident angle and wavelength. Additionally, the leaky modes' polarization is dependent on the polarization of the coupled incident light.

It is possible to design a 2D asymmetric surface PC to engineer modes with wide wavelength separation in order to enhance optical down-conversion from the blue to NIR wavelengths. In the PC band diagram shown in Fig. 4.2(b), both TE and TM modes are present in the NIR wavelength range of λ=800-900 nm which spectrally overlap with the NIR emission of the PbS QD. Thus, this provides enhanced extraction of emitted light from the QD through coupling of the PC mode to free space. Additionally, as seen in Fig. 4.2(a), PC modes are also obtained at λ=450 nm which spectrally overlap with the blue wavelength pump light, providing enhanced excitation through resonant coupling of the excitation light into the PC mode. Fig. 4.3 shows the simulated reflection spectrum for normal incident light with optical resonances located at (a) λ = 450 nm and (b) λ = 850 nm.

The simulated electric field mode profiles of the TE mode at λ=888 nm and TM mode at λ=848 nm are shown in Fig. 4.4(a) and Fig. 4.4(b), respectively. The white rectangular regions depict the high RI TiO_2 material. In this simulation, the QDs are located in the polymer. Due to the boundary conditions of continuous dielectric displacement, the TM mode has higher electric

field intensity concentrated in the low RI regions as compared to the TE mode. Additionally, the TM mode has electric field components in both *x* (not shown) and *z* directions, while the TE mode only has electric field components in the *y* direction.

The PC mode at λ=850 nm does not interact with the Λ_2=220 nm PC since the feature sizes are much smaller than the wavelength of the light. However, the PC mode at λ=450 nm does interact with the Λ_1=520 nm PC since the feature sizes are larger than the wavelength of the light. This interaction causes diffraction from the Λ_1=520 nm PC which reduces the coupling efficiency which was confirmed by simulation results. This effect can be minimized by varying the duty cycle of the Λ_1=520 nm PC to the optimal value of 60% resulting in a maximum reflection efficiency of 80% for the PC mode at λ=450 nm. Maximizing this value is critical in obtaining the highest intensity electric field for enhanced excitation. The 2D surface PC is not polarization independent since the surface PC is asymmetric. Thus, for unpolarized incident light, the maximum amount of light reflected from the surface PC is 50% for both TE PWV.

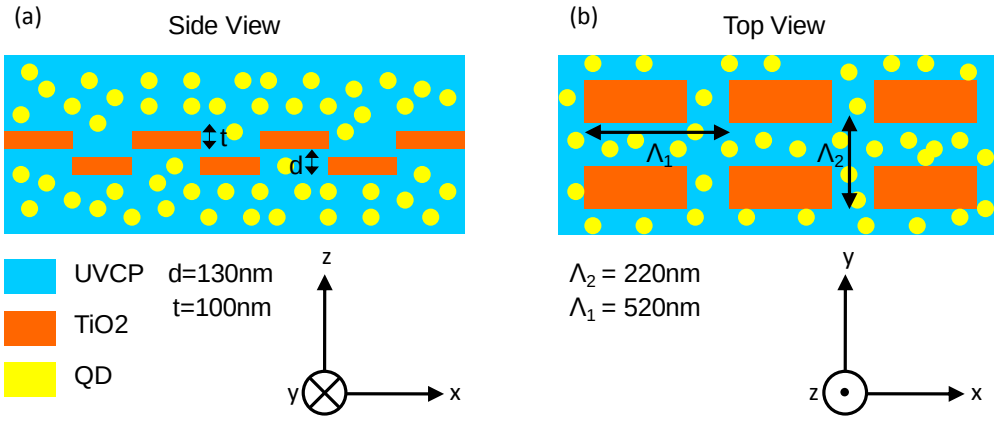

Figure 4.1 Schematic cross section of both (a) side view and (b) top view of the 2D asymmetric surface PC.

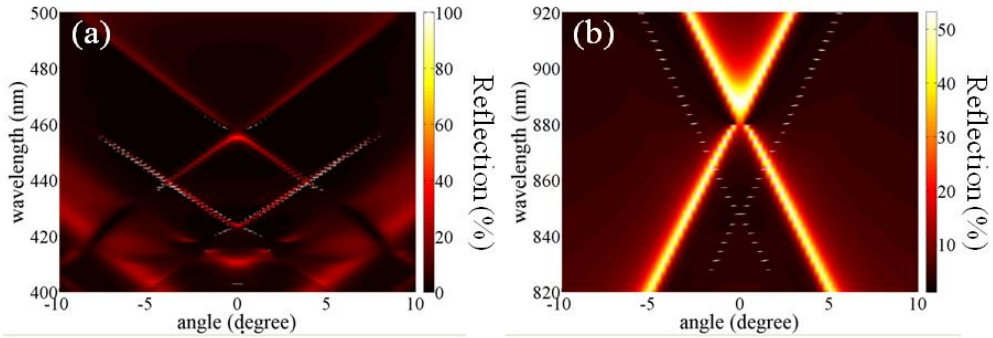

Figure 4.2 RWCA simulation results of the PC leaky mode band diagram at (a) excitation wavelength range and (b) extraction wavelength range.

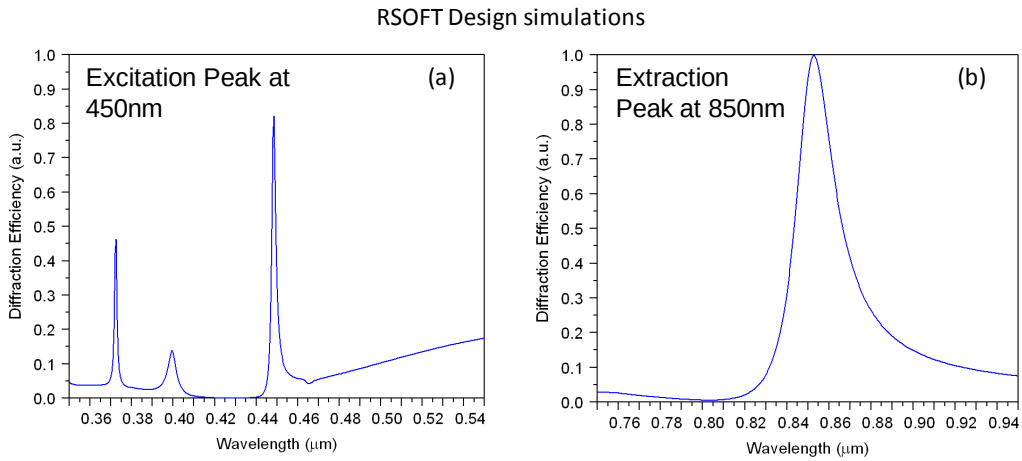

Figure 4.3 RCWA simulation results showing the reflection spectrum for TE polarized in both the (a) Λ_2=220 nm and (b) Λ_1=520 nm directions.

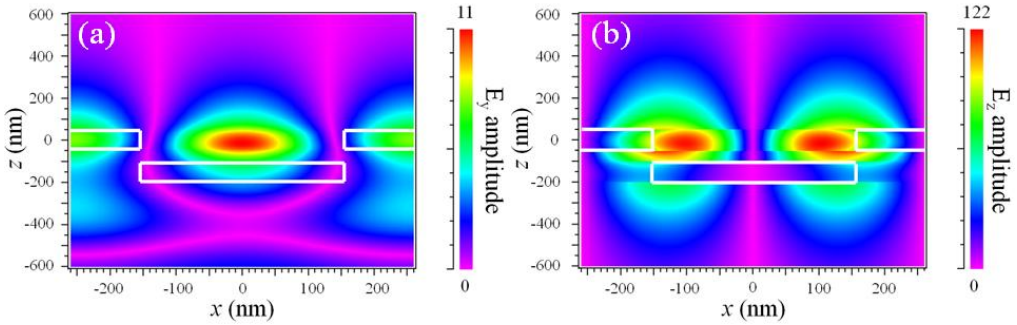

Figure 4.4 RWCA simulations of (a) TE mode *y*-polarized electric field at λ=888 nm and (b) TM mode *z*-polarized electric field at λ=848 nm.

4.4 Fabrication of 2D Asymmetric Surface Photonic Crystal with Semiconductor Quantum Dots

The fabrication process employs nanoreplica molding which allows room temperature, low cost, and large area fabrication on plastic substrates. The process flow diagram is depicted in Fig. 4.5. First, a 2D surface PC structure was nanoreplica molded from a master wafer onto a polyethylene terephthalate (PET) substrate. The master is a 2-inch diameter silicon wafer upon which a 2D surface PC structure with a period of Λ_1=520 nm and 50% duty cycle and Λ_2=220 nm and a 60% duty cycle is patterned by electron beam lithography over a 2x2 mm^2 area. The 2D surface PC pattern is etched into the silicon wafer to a depth of d=130 nm by reactive ion etching. The completed master wafer is composed of a rectangular lattice of rectangular posts. Fig. 4.6 shows an SEM of the silicon master. The 2D surface PC is nanoreplica molded from a thermoplastic embedded with QD. Ten milligrams of the thermoplastic (Tetramer NDM, Tetramer Tech.) are dissolved in 100 μL of the organic solvent, mesitylene, while the PbS QDs (Evident Tech.) are in a toluene solution of 10 mg/mL concentration. 100 μL thermoplastic solution and 400 μL QD solution are mixed to obtain a mass ratio of QD/thermoplastic of 2/5. The mixture is placed in a desiccator in order to evaporate the solvent until 100 μL remains. This solution of thermoplastic/QD is spin-coated onto the silicon master wafer at 3000 rpm for 30 seconds. A thin film of approximately 4 μm of the thermoplastic forms on the silicon master wafer and conforms to the 2D surface PC structure. The silicon master is then placed on a hotplate at 110 ˚C for 120 seconds in order to evaporate any remaining solvent. The nanoreplica mold of the PC structure is then transfer printed onto a flexible PET substrate. In order to transfer the PC structure from the silicon master, a layer of liquid ultraviolet curable polymer (UVCP) was drop-coated over the thermoplastic/QD film. A PET substrate is then placed over the master wafer and brought into contact using mechanical pressure from a rolling cylinder.

This enabled the UVCP drops to form a thin continuous layer between the PET and the thermoplastic/QD thin film. Next, the UVCP is cured for 90 seconds using a high intensity UV lamp (Xenon Corp.). The PET substrate, along with the UVCP layer and thermoplastic/QD thin film, is released from the silicon master and the thin film of thermoplastic/QD with the 2D surface PC nanoreplica mold is fabricated. Fig. 4.7 shows an SEM image of the nanoreplica mold. In order to produce a surface PC that supports optical modes, a high RI thin film must be deposited over the low RI (n=1.56) replica-molded grating structure. Sputter-deposited thin films of approximately t=110 nm of TiO_2, with a RI of n=2.59 at λ=450 nm and n=2.32 at λ=850 nm, served as the high RI layer. Next, an additional film of thermoplastic/QD is spin-coated over the TiO_2 layer in order to complete the device structure. After spin-coating, the device is baked in an oven at 90 ˚C for 15 minutes to evaporate any remaining solvents. Even though this work used a 2x2 mm^2 patterned area for proof of concept, the fabrication area is limited only by the size of the silicon master. Previous work using nanoreplica molding used an 8 inch diameter silicon master wafer to fabricate large area PC devices [40].

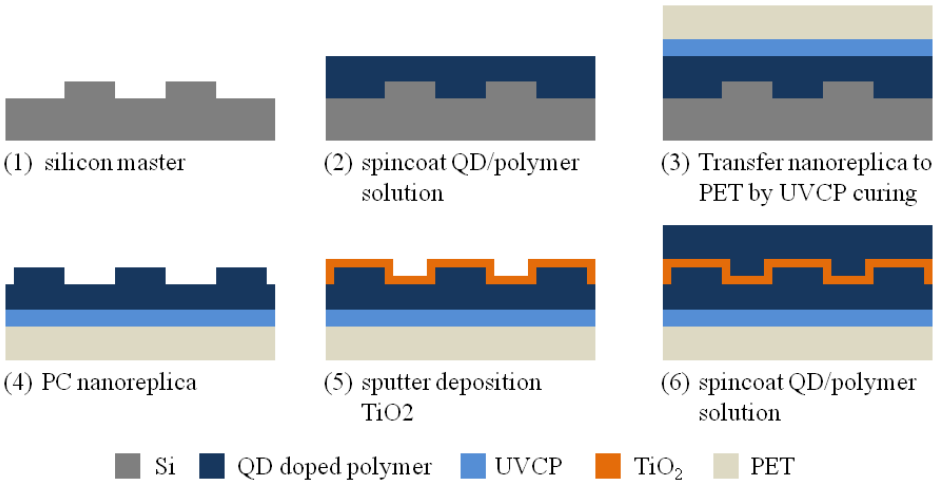

Figure 4.5 Process flow diagram of nanoreplica molding process of 2D photonic crystal.

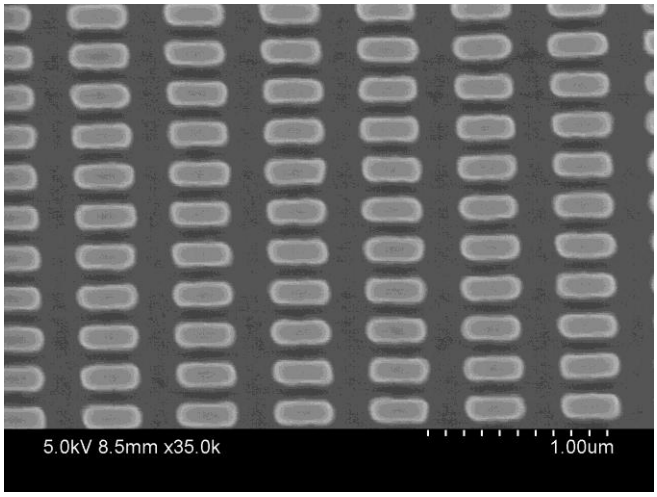

Figure 4.6 SEM image of the silicon master made from Ebeam lithography. The 2D surface PC structure is a rectangular lattice of rectangular posts with periods Λ_2=220 nm and Λ_1=520 nm in orthogonal directions.

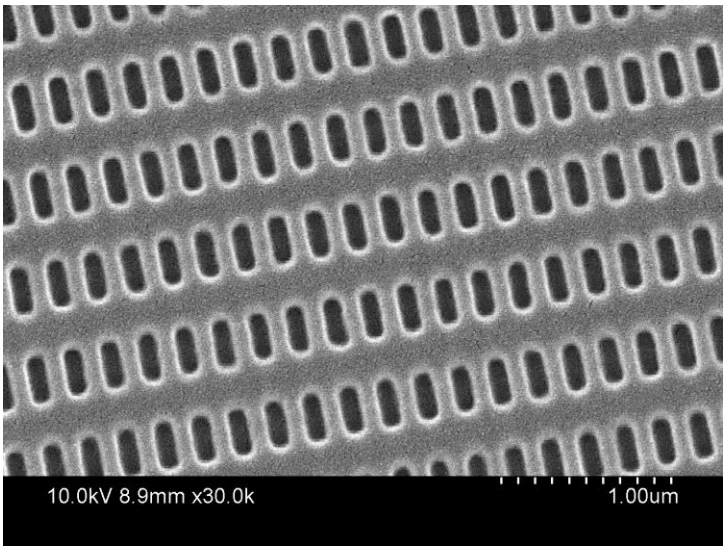

Figure 4.7 SEM image of the thin film thermoplastic/QD nanoreplica mold after release from the silicon master. The resulting mold is a rectangular lattice of rectangular holes, complementary to the silicon master structure.

4.5 Enhanced Extraction Effect of 2D Surface Photonic Crystal on Quantum Dots

The angle resolved fluorescence setup shown in Fig. 4.8 is used to characterize the emission properties of the PC device. A continuous wave (CW) laser source at λ=457 nm is used to optically pump the QD. The PC device is mounted on an adjustable tilt mount that can rotate in order to adjust the incident angle between the PC and the excitation laser beam. A fiber optic

cable connected to a collimating lens is attached to an optics rail that is allowed to rotate around the mount holding the PC device. The light emitted from the QD is collected at different extraction angles relative to the PC surface normal. The collimating lens is adjusted relative to the optical fiber end such that only light which is incoming at normal incidence is coupled into the fiber. This enabled the collection optics to have good angular resolution for observing emission of the QD. A high pass filter is placed in front of the collimating lens in order to filter out the excitation light at λ=457 nm. The other end of the optical fiber is connected to a spectrometer (USB2000, Ocean Optics) and the emission spectrum is observed using the accompanying software (001Base, Ocean Optics). Using angle resolved fluorescence, the enhanced extraction effect is measured by setting the excitation angle θ constant at an off resonant value while varying the extraction angle φ from 0 to 10 degrees in 0.5 degree increments.

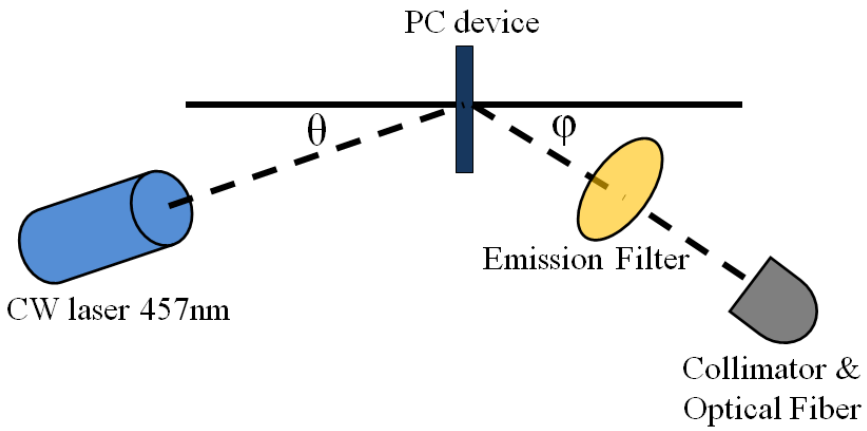

Figure 4.8 Angle resolved fluorescence setup used to characterize the emission properties of QD in the PC device. The excitation angle θ and the extraction angle φ are both adjustable. Enhanced extraction experiment is performed by varying the extraction angle φ while keeping the excitation angle θ constant. Enhanced excitation experiment is performed by varying the excitation angle θ while keeping the extraction angle φ constant.

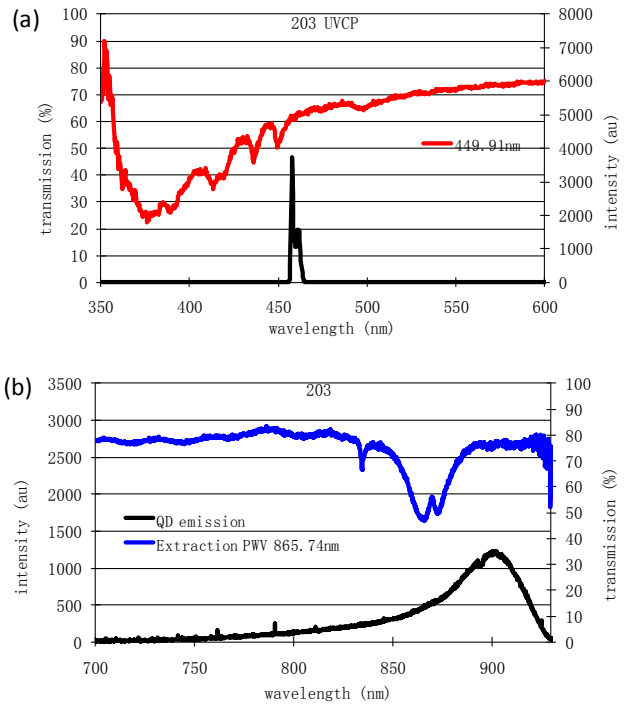

Figure 4.9 Transmission spectrum of the 2D surface PC showing the TE PWV for both (a) Λ_2=520 nm and (b) Λ_1=520 nm directions. The TE PWV achieve close spectral overlap with the excitation laser wavelength and the QD emission wavelength.

The normal incidence transmission spectrum of a 2D surface PC embedded with QD is shown in Fig. 4.9. The TE PWV in the Λ_2=220 nm direction is the red curve and is located at approximately λ=450 nm. The excitation laser output is superimposed in black and occurs at λ=457 nm. By slightly adjusting the incident angle of the surface PC with the laser, it is possible to excite a surface PC mode at λ=457 nm. The TE PWV in the Λ_1=520 nm direction is the blue curve and is located at approximately λ=865 nm. The black curve is the QD emission observed from the stock solution of QD in toluene. Even though the TE PWV is not at λ=850 nm, the emission peak of the QD is broad enough (FWHM=100 nm) that sufficient spectral overlap remains and is tolerant to slight deviations from the designed value. The transmission spectrum is normalized to the unpolarized incoming light. Thus, the TE PWV is able to block a maximum amount of 50% of the incoming light. The longer wavelength TE PWV is able to achieve this

value, while the shorter wavelength TE PWV has less efficient resonance peak. This may be due to the narrow linewidth of the resonance preventing the limited spectral resolution of the spectrometer to resolve the true minimum value of the PWV. Additionally, the light at λ=450 nm can experience diffraction loss from the Λ_1=520 nm period PC which decreases its efficiency as well.

The photonic band diagram of the 2D PC can be experimentally obtained by acquiring the transmission spectrum at different incident angles and compiling the data to form a plot of the transmission as a function of both wavelength and angle. The optical transmission setup comprises a broadband tungsten-halogen lamp which is coupled to an optical fiber connected to a collimator. The light is incident on the PC, and the transmitted light is collected through another optical fiber coupled to a spectrometer (Ocean Optics USB2000). The PC is held on a rotation mount which enables characterization of the transmission spectrum at varying incident angles.

Using unpolarized light, the photonic band diagram for the PC is obtained and depicted in Fig. 4.10(a). Two offset "X" shaped features are seen in the photonic band diagram. The band labeled *i* is a wide, full width at half maximum (FWHM) TE band that is resonant at λ=900 at normal incidence. Likewise, the band labeled *ii* is a narrow FWHM TM band that is resonant at λ=860 nm at normal incidence. These are the leaky modes allowed by the surface PC. The experimental band diagram is red-shifted by approximately $\Delta\lambda$=12 nm compared to the simulated band diagram in Fig. 2(a). This is due to slight differences between the simulated and fabricated structures due to fabrication variations. In addition, the RI dispersion of the materials comprising the PC was not taken into account, within the range of λ=820 – 920 nm, in the simulation. However, even with the simplified simulated PC structure, the experimental and simulated results agreed quite well, qualitatively. The polarization dependence of the TE and

TM bands was confirmed by placing linear polarizers in front of the collection optical fiber. The two bands could be distinguished by a 90º rotation of the linear polarizer. When there is spatial and spectral overlap, the QD emission is preferentially coupled to these surface PC modes and the photons are coupled out of the surface PC to free space at the appropriate extraction angles which satisfy the phase matching condition. This is observed in the angle resolved emission measurements shown in Fig. 4.10(b). The emission intensity from the QD is much stronger along the bands of the surface PC due to this enhanced extraction effect.

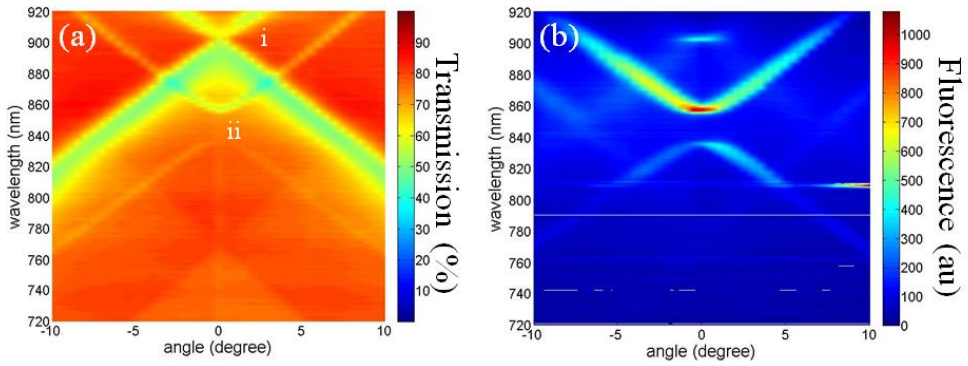

Figure 4.10 (a) Experimental photonic band diagram for the PC device and (b) the corresponding angle resolved emission spectrum of QD in the PC device.

The emission is strongest when the surface PC mode spectrally overlaps the emission peak of the QD at λ=860 nm and decreases for wavelengths away from this value. In fact, the emission is much lower at wavelengths above λ=900 nm and below λ=800 nm. This is due to the poor spectral overlap between the QD emission spectrum and the PC optical modes outside this wavelength range. Additionally, the enhanced extraction effect is stronger for the TM band than the TE band. The TM mode has better spatial overlap with the low RI regions (thermoplastic/QD layers) of the PC where the QDs are located, as shown in the simulations results in Fig. 4.4(b). This improves the spontaneous emission rate since the QDs interact with

more of the electric field profile. This reason points to the TM modes having higher extraction enhancement than the TE modes.

At normal incidence, the emission spectra of the QD within the surface PC (red curve) and the QD with no surface PC (blue curve) are compared and shown in Fig. 4.11. The two shorter wavelength emission peaks correspond to extraction due to outcoupling from TM modes, while the longest wavelength emission peak corresponds to extraction enhancement due to outcoupling from a TE mode. At these wavelengths and normal incidence emission, the enhanced extraction effect is clearly seen over the QD with no surface PC. At λ=865 nm, the enhancement is ~8x relative to an adjacent QD/polymer coated surface with no PC pattern.

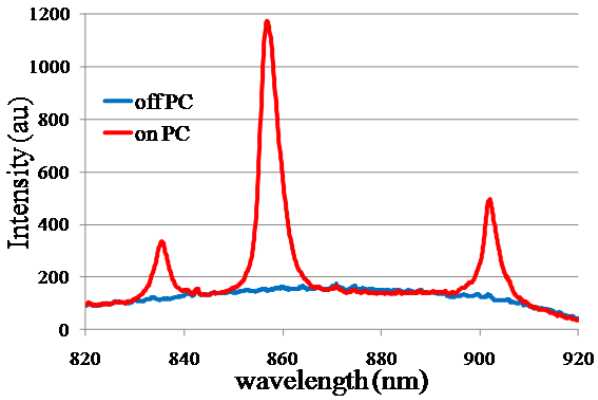

Figure 4.11 Emission from QD at normal incidence extraction angle for QD in the PC device (red) and QD with no PC (blue). The enhanced extraction is about eight times at the emission peak of λ=865 nm.

Angle resolved emission measurements are obtained for the QD with no surface PC and compared to the QD within a surface PC. The emission spectrum for the QD with no surface PC shows no enhanced extraction effect and no variation in emission peak intensity as a function of angle, as seen in Fig, 4.12(a). The QDs within the surface PC show clear modifications in their emission characteristics, in comparison. This effect is useful for controlling the emission angle

of a narrow band of wavelengths in order to achieve better coupling or collection efficiency to other optical elements.

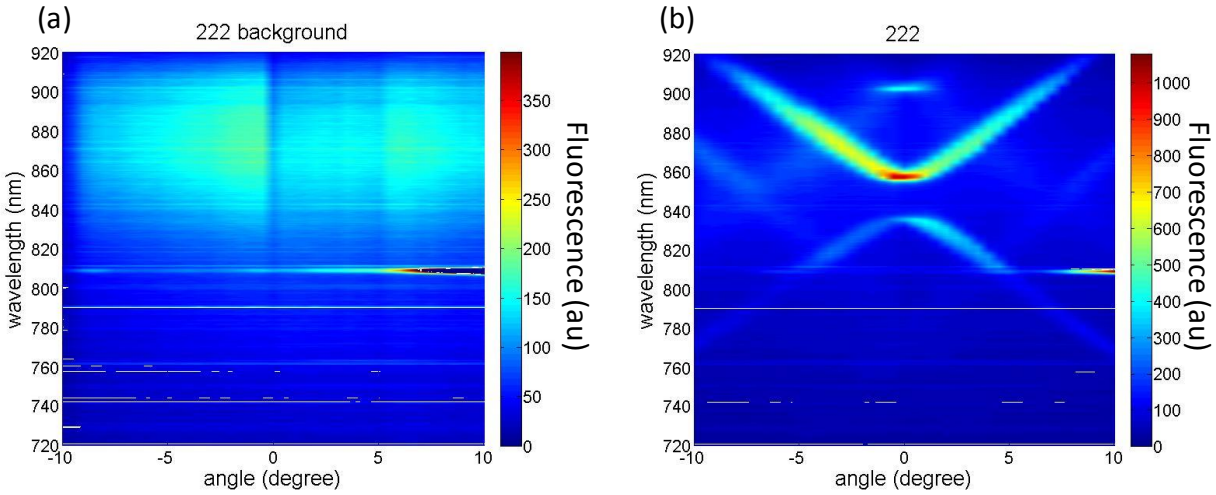

Figure 4.12 Angle resolved emission from (a) QD with no surface PC and (b) QD within a surface PC. The broad emission peak at λ=865 nm is seen from (a) with no variation as a function of emission angle. The emission is clearly modified by the surface PC through wavelength and emission angle dependent enhanced extraction effect seen in (b).

4.6 Excitation Effect of 2D Surface Photonic Crystal on Quantum Dots

Angle resolved emission measurements were also used to characterize the enhanced excitation effect of the PC. This was accomplished by observing the emission from the QD at a fixed extraction angle φ normal to the PC surface while varying the excitation angle θ. At a certain excitation angle, the pump light is able to couple into a PC mode through phase matching enabled from the PC. This results in enhanced electric fields relative to the pump light, which increases the radiative absorption rate of the QD. Consequently, the emission intensity is enhanced. Thus, at this resonant excitation angle, the QD emission intensity is at maximum. Fig. 4.13 shows the transmission spectrum of a PC at 5.5º incident angle, along with the emission spectrum of the pump laser. There is good spectral overlap between the PC resonance and the pump light. Additionally, the polarization of the PC mode matches the polarization of the pump light, which is critical for coupling. The measured resonance transmission efficiency is 47% as

observed using the broadband transmission setup. Using a silicon photodetector to measure the transmitted power of the pump laser at different excitation angles results in a measured transmission efficiency of 40%. This discrepancy is most likely due to the limited resolution of the spectrometer.

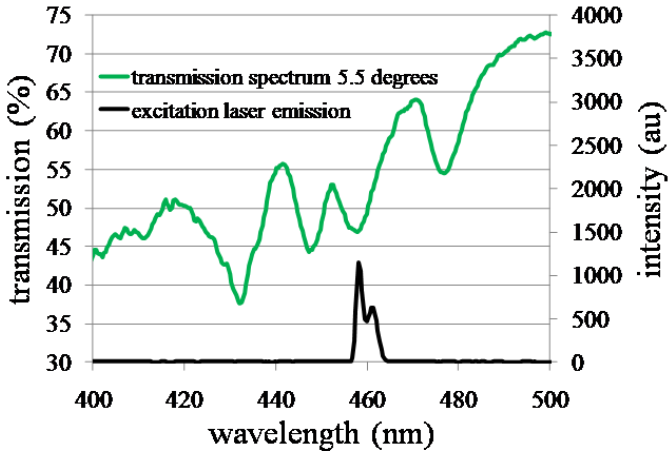

Figure 4.13 Transmission spectrum of the PC device at 5.5 degrees oblique incidence overlaid with the emission laser of the excitation laser. Good spectral overlap is observed at λ=457nm at this excitation angle which satisfies the enhanced excitation condition.

The resolved emission intensity at normal incidence was observed as a function of excitation angle, and the maximum fluorescence intensity was plotted as a function of the excitation angle. From Fig. 4.14, the enhanced excitation effect is shown to increase the fluorescence intensity 1.5x for the measured PC. Even though this demonstrates enhanced excitation, the enhancement value is limited by the coupling efficiency of the PC mode. The enhanced electric fields enabled through coupling to the PC mode are lowered due to multiple optical loss mechanisms. Currently, the transmission efficiency is 40% resulting in low enhancement values. Improving the transmission efficiency, i.e. reducing the transmission value towards 0%, will result in higher excitation enhancement values. The main loss mechanisms are absorption from the QD and polymer and scattering from the PC. Since the excitation light at wavelength λ = 457 nm is able to interact with the λ = 550 nm period PC, this results in scattering and introduces loss to the PC mode. Thus, the efficiency is reduced resulting in

lowered electric fields and a lower Q factor. Improving on the PC design to reduce this loss due to scattering will lead to higher excitation enhancement values.

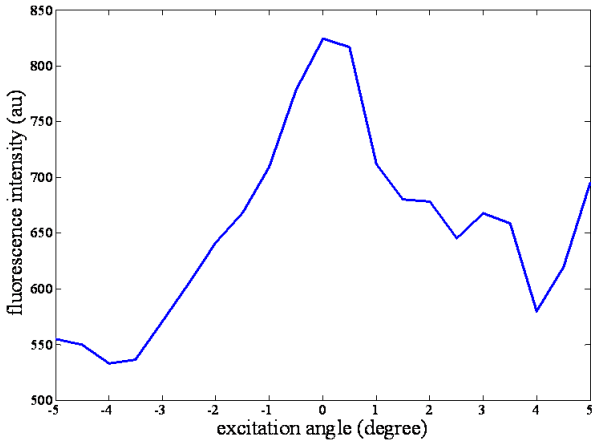

Figure 4.14 Peak emission fluorescence intensity at normal incidence extraction angle for varying excitation angle. An increase in fluorescence intensity is observed at the resonant excitation angle condition.

The conversion efficiency of the QD embedded PC was measured using an integrating sphere. The conversion efficiency is defined as the input power of the laser divided by the output power of the QD. This was measured using a silicon photodetector. The excitation laser power was measured directly without the integrating sphere. The PC was placed directly in front of an input port of the integrating sphere and pumped using the excitation laser. An emission filter is placed in front of the photodetector, and the QD emission was measured from the output port of the integrating sphere. This measured power was then converted into total power by taking into account the area ratio between the integrating sphere and the output port and also the fact that only half of the QD emission is directed into the integrating sphere while the other half is directed away.

The measured conversion efficiency is comparable between the QD embedded in a PC and the QD embedded in non-structured polymer when enhanced excitation does not occur. Since the enhanced extraction effect only couples light into preferential directions and does not increase the emission rate of the QD, the total emission power integrated over all emission angles

should not change for the QD embedded in PC and in non-structured polymer layer. Therefore, no increase in emission power is expected. Re-absorption effects might result in decreased emission power in the PC device compared to non-structured polymer due to increased interaction time for the output light that couples to leaky modes for enhanced extraction. However, this was not seen in the experimental results indicating that re-absorption effects are negligible for this PC device. Typical conversion efficiencies were around 10%. A non-reversible degradation in the conversion efficiency of PC devices was observed after being optically pumped over time. This was due to an irreversible decrease in the emission intensity of the PbS QD over time, which is a characteristic of the QD and not a result of the PC design [79]. The conversion efficiency of the PC device was measured as a function of excitation angle. At the resonant excitation angle, enhanced excitation occurred, and the QD embedded in the PC increased in emission power due to increased absorption rate. An accompanying increase in conversion efficiency occurred. At the resonant angle, the enhanced excitation effect improved the conversion efficiency approximately 2.5x, from 10% to 25 %, for the QD embedded in PC compared to the QD embedded in non-structured polymer layer as shown in Fig. 4.15. The differences in enhanced excitation values between Figs. 4.14 and 4.15 are due to Fig. 4.14 reporting enhancement values at a single wavelength while Fig. 4.15 is a result of enhanced excitation integrated over all wavelengths emitted by the QD. Also, different devices were used in each experiment with varying performance due to fabrication variations and device degradation over the course of experiment trials. In each case, however, the effect of enhanced excitation is evident.

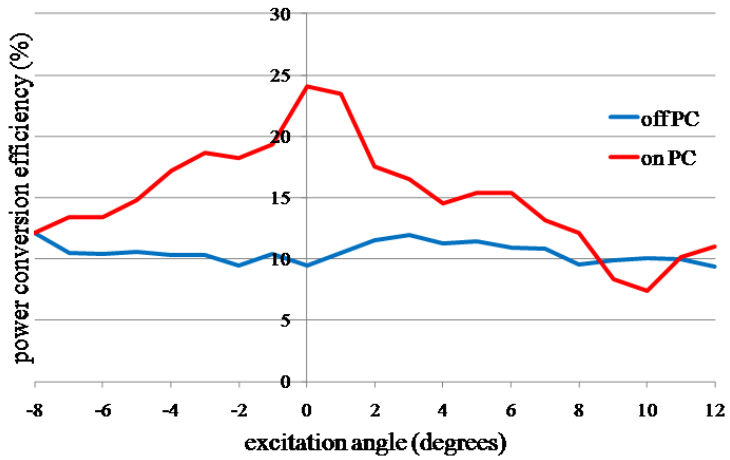

Figure 4.15 Power conversion efficiency measured using an integrating sphere and at varying excitation angles. The PC improves the conversion efficiency over 2.5x through the enhanced excitation effect.

4.7 Conclusion

We demonstrated the design, fabrication, and characterization of a 2D asymmetric PC engineered to improve the conversion efficiency of optical down-conversion of PbS QD from the blue to NIR wavelengths. Using a nanoreplica molding process that can potentially scale up to large areas and flexible substrates, we fabricated PC with embedded QD. Both enhanced extraction and enhanced excitation effects were simultaneously possible at wide wavelength separation due to the 2D asymmetric PC design. Coupling to leaky modes of the PC enabled an enhanced extraction effect that preferentially coupled QD emission light out of the PC into controlled directions. This is important for directing light to other optical elements. Furthermore, the enhanced excitation effect was observed when the excitation light was at a resonant condition. This increased the emission intensity and improved the conversion efficiency in comparison to the QD embedded in non-structured polymer.

CHAPTER 5 FUTURE WORK

5.1 Stacked 2D Surface Photonic Crystals

The 2D asymmetric PC was designed in order to achieve PC leaky modes at large wavelengths separations, namely, at an excitation wavelength of $\lambda = 450$ nm and an extraction wavelength of $\lambda = 800 – 900$ nm. One disadvantage of using an asymmetric design is that the PC leaky mode resonances are polarization dependent. Thus, the phase matching conditions depend on the wavelength, incident angle, and polarization of incident light. As a consequence, only light that is TE polarized can couple into the leaky modes for the PC enhanced excitation described in section 4.6. Using a laser for enhanced excitation allows all of the polarized output light to couple into the PC leaky mode, in theory. However, for light sources such as LEDs, the output light is not polarized. In this case, a maximum of half of the output light can couple into the PC leaky modes and contribute to the enhanced excitation effect, in theory. In enhanced extraction, the light emitted by the QD must have the correct polarization, wavelength, and wave vector in order to couple to a PC leaky mode and be extracted from the PC in a controlled fashion. For a given wavelength, assuming the PC leaky mode is TE polarized, the light emitted by the QD which is TM polarized will not couple into this mode and contribute to enhanced extraction. The complementary case is also true. Thus, it is important to have polarization independent leaky modes in order to increase the enhanced excitation and extraction effects. An increase of potentially 2x from enhanced excitation and enhanced extraction may be possible.

This may be accomplished using 2D symmetric surface PC. However, the PC design must achieve leaky modes at large wavelength separations. This can be achieved by stacking two 2D symmetric PC with different periods. Fig. 5.1 shows a cross section schematic of the proposed device design. The red region consists of the thermoplastic polymer with embedded QD shown as yellow dots. The purple layer is the high RI TiO_2. Figs. 5.2(a) and 5.2(b) depict

the top view of the top PC and bottom PC, respectively. The bottom layer is a 2D symmetric PC with period Λ = 250 nm, while the top layer is a 2D PC with period Λ = 500 nm. The modulation depth is d = 150 nm for both surface PC and the high RI TiO_2 layer is t = 100 nm for both surface PC as well. The bottom PC is designed for a leaky mode at an excitation wavelength of λ = 450 nm at normal incidence, while the top PC is designed for a leaky mode at an extraction wavelength of λ = 850 nm at normal emission. The spacing between the two PC layers is *s* = 200 nm. This spacing parameter is critical and determines how much mode coupling occurs between the two PC layers. The embedded QD must have spatial overlap with both excitation and extraction modes. Hence, there must be mode coupling between the PC layers in order for the embedded QD to experience both enhanced excitation and extraction effects.

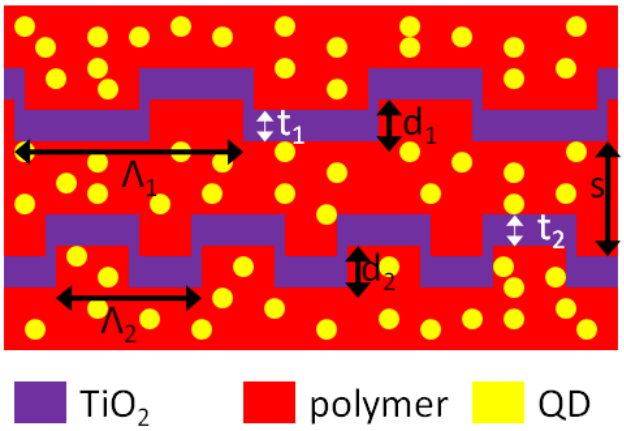

Figure 5.1 Cross section schematic of a stack 2D surface PC.

RCWA simulations were performed on this PC device design using the same simulation rules discussed previously in section 4.3. Fig. 5.3 shows the result of the normal incidence reflection spectrum for unpolarized incident light, illustrating leaky modes at λ = 850 nm and λ = 450 nm. Additionally, the leaky mode spatial profiles at the excitation and extraction wavelengths are shown in Figs. 5.4(a) and (b), respectively. Mode coupling can clearly be seen

between the two PCs and good spatial overlap occurs with the embedded QD. The simulation results support the hypothesis that this PC device design has polarization independent leaky modes at both $\lambda = 850$ nm and $\lambda = 450$ nm.

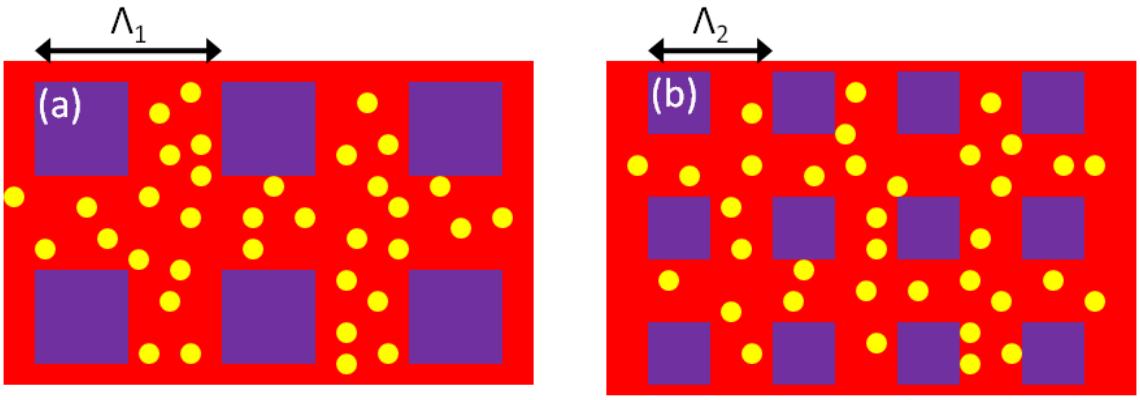

Figure 5.2 Top view of the surface PC for (a) enhanced extraction effect and (b) enhanced excitation effect.

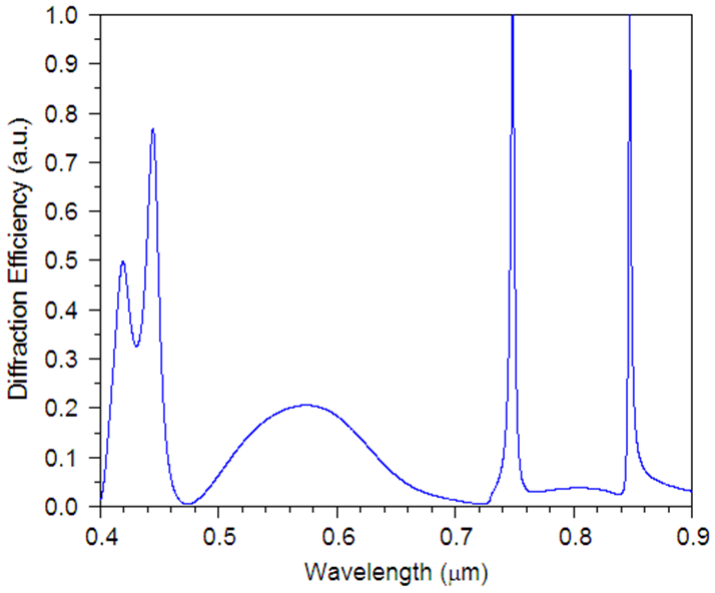

Figure 5.3 RCWA simulation of the reflection spectrum of the stack surface PC. TM leaky mode resonances are observed at the wavelengths near $\lambda = 450$ nm and $\lambda = 850$ nm.

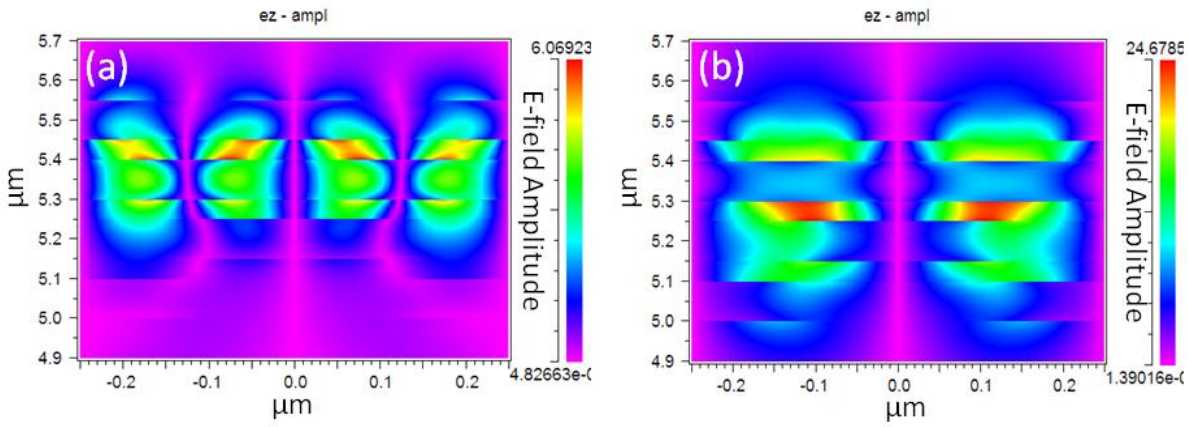

Figure 5.4 RCWA simulations showing the electric field mode profile at (a) excitation wavelength and (b) extraction wavelength. Mode coupling between the two surface PC are clearly seen.

The fabrication process is proposed here. The bottom PC can be fabricated by using nanoreplica molding of a QD embedded thermoplastic and transfer printing onto a plastic substrate as discussed in previously in section 4.3. Then, a layer of TiO_2 is deposited using sputter deposition. Next, the same QD embedded thermoplastic is deposited over the TiO_2 layer using horizontal dipping method. Horizontal dipping enables deposition of thin films of uniform thickness over a large area. Using a PDMS mold made from a silicon master comprising the top PC structure, the second polymer layer can be replica molded. Then, another layer of TiO_2 is deposited using sputter deposition. The last layer of QD embedded polymer is then spin-coated over the second TiO_2 layer in order to complete the device. Further work on fabrication and characterization needs to be pursued for future work.

5.2 Beam Steering Using Tunable Surface Photonic Crystals

The enhanced extraction effect enables engineered control of the emission from light emitters such as QD embedded within a surface PC. The emission is preferentially emitted in certain emission angles depending on its wavelength. This occurs due to the phase matching that is provided by the surface PC and the resulting efficient outcoupling, or extraction, of light from

the surface PC at these resonant conditions. Different wavelengths of light will preferentially couple out of the surface PC structure at different emission angles. By incorporating and utilizing optically tunable materials into the PC design, it is possible to tune the emission angle of light from a QD, given a particular wavelength. For instance, tuning the RI of the superstrate layer will change the effective RI of the PC leaky mode. This will change the phase matching equation. Hence, different wavelength and emission angle conditions will satisfy the new phase matching condition. Consequently, light at a given wavelength will now couple into a new leaky mode, and enhanced extraction will occur at a different emission angle. Incorporating materials whose RI can be either electro-optically or all optically tuned, allows such control. Previous work was demonstrated using nematic LC and azo-LC to tune the optical response of 1D and 2D surface. In general, other materials can be used, such as electro-active polymers, conducting polymers, and electro-optic polymers, whose RI can be tuned electro-optically.

The proposed 1D surface PC design is illustrated in Fig. 5.5. The 1D surface PC has a period of Λ = 485 nm, TiO_2 thickness of t = 100 nm, and modulation depth of d = 150 nm. The cross section schematic show a layer of QD embedded polymer. The surface PC structure can be fabricated using nanoreplica molding using a silicon master wafer with the appropriate 1D surface PC features. The silicon master can be fabricated using either deep UV lithography or nanoimprint lithography. The nanoreplica mold can be transfer-printed onto a plastic substrate as previously described in section 4.4. Next, a high RI layer of TiO_2 is deposited using sputter deposition. For all optical tuning, a layer of azo-LC is used as the superstrate and capped off with a cover layer consisting of another plastic substrate with a rubbed PI layer for homogenous alignment as described in section 2.3.

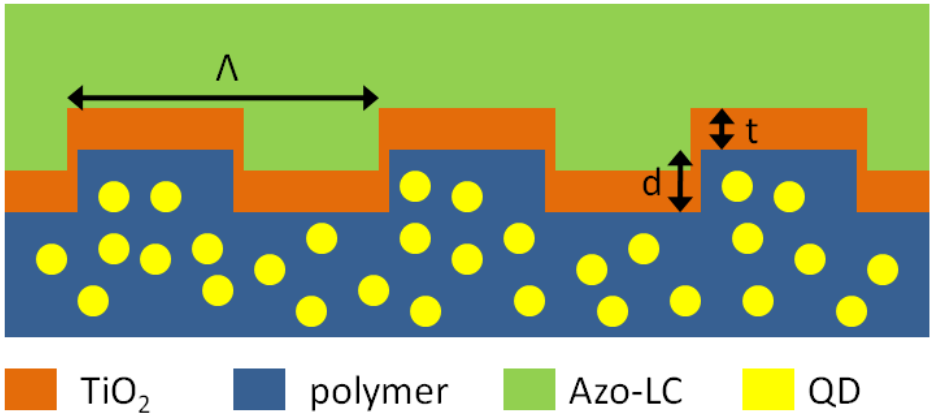

Figure 5.5 Cross section schematic of a tunable 1D surface PC with embedded quantum dots.

In principle, the device would be able to tune the RI of the azo-LC by inducing photo-isomerization between *trans* and *cis* isomers. Transition from *trans* to *cis* would be accomplished using green light, while transitions from *cis* to *trans* would be accomplished using red light. In both cases, the pump light would also serve as the excitation source for the QDs themselves. In this way, all optical tuning of the emission angle of QD emission would be enabled. Since the QD emission spectrum is broad, multiple wavelengths will be emitted at multiple corresponding angles. In order to selectively emit only one particular wavelength and angle, a band pass optical filter can be placed above the surface PC.

The proposed surface PC device was simulated using RCWA simulation. The RI of the superstrate was tuned from $n_{cis} = 1.57$ to $n_{\parallel} = 1.726$, and the angular reflection spectrum of the surface PC was simulated for the TM mode. As shown in Fig. 5.6, at an emission wavelength of $\lambda = 848.2$ nm, the emission angle could be tuned from 0º to 3.84º for a $\Delta n = 0.156$. For this particular 1D surface PC, the sensitivity is -23.92 degrees/RIU as calculated by a linear fit to the simulation data with a high R^2 value, as shown in Fig. 5.7. The simulation results are consistent with theory and are promising. Further work on fabrication and characterization needs to be pursued for future work.

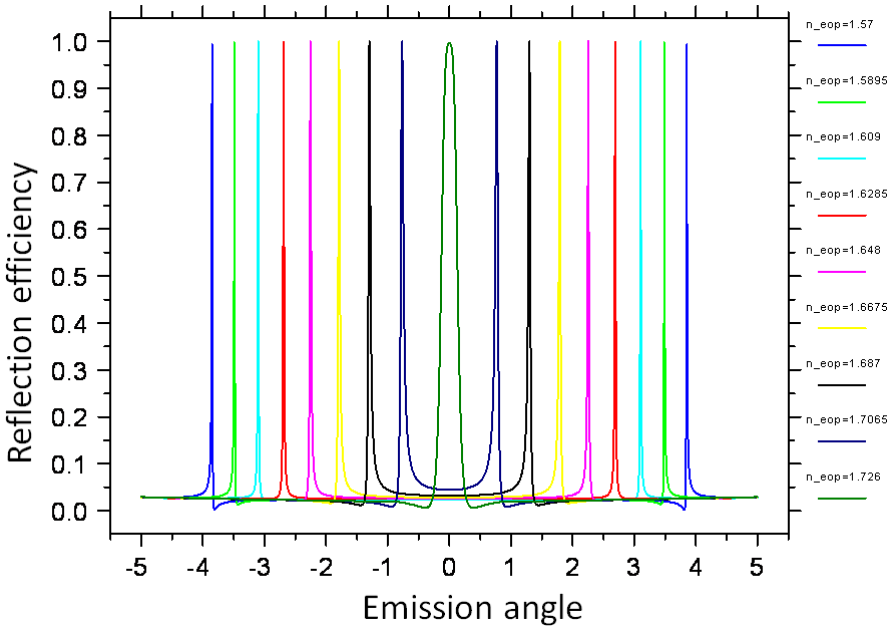

Figure 5.6 RCWA simulation results for the angular reflection spectrum at λ = 848.2 nm for different RI of the azo-LC.

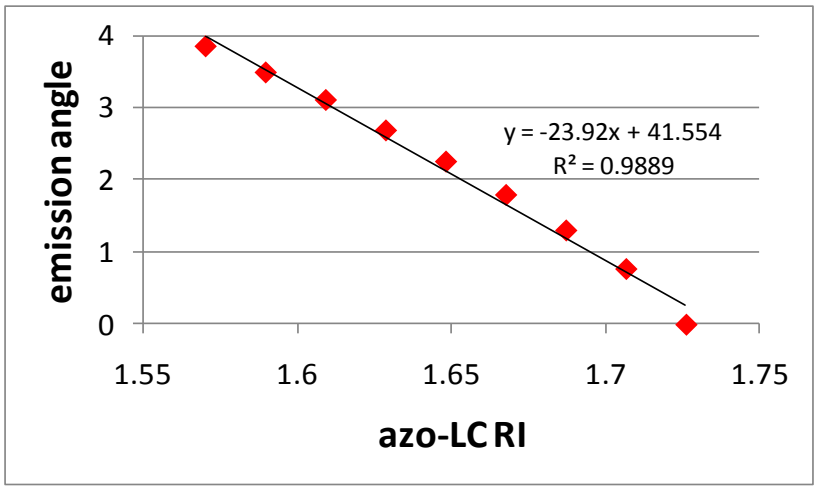

Figure 5.7 Plot of emission angle versus RI change of azo-LC.

REFERENCES

1. J. D. Joannopoulos, R. D. Meade, and J. N. Winn, *Photonic Crystals: Molding the Flow of Light* (Princeton University Press, 1995).
2. S. G. Johnson, S. H. Fan, P. R. Villeneuve, J. D. Joannopoulos, and L. A. Kolodziejski, "Guided modes in photonic crystal slabs," Physical Review B **60**, 5751-5758 (1999).
3. N. Ganesh, I. D. Block, P. C. Mathias, W. Zhang, E. Chow, V. Malyarchuk, and B. T. Cunningham, "Leaky-mode assisted fluorescence extraction: application to fluorescence enhancement biosensors," Optics Express **16**, 21626-21640 (2008).
4. R. Magnusson, D. Shin, and Z. S. Liu, "Guided-mode resonance Brewster filter," Optics Letters **23**, 612-614 (1998).
5. R. Magnusson and S.-S. Wang, "Optical Guided-Mode Resonance Filter," 5,216,680 (June 1 1993).
6. R. Magnusson and S. S. Wang, "New Principle for Optical Filters," Applied Physics Letters **61**, 1022-1024 (1992).
7. N. Ganesh, W. Zhang, P. C. Mathias, E. Chow, J. A. N. T. Soares, V. Malyarchuk, A. D. Smith, and B. T. Cunningham, "Enhanced fluorescence emission from quantum dots on a photonic crystal surface," Nature Nanotechnology **2**, 515-520 (2007).
8. B. Cunningham, P. Li, B. Lin, and J. Pepper, "Colorimetric resonant reflection as a direct biochemical assay technique," Sensors and Actuators B-Chemical **81**, 316-328 (2002).
9. B. Cunningham, B. Lin, J. Qiu, P. Li, J. Pepper, and B. Hugh, "A plastic colorimetric resonant optical biosensor for multiparallel detection of label-free biochemical interactions," Sensors and Actuators B-Chemical **85**, 219-226 (2002).
10. B. Cunningham, J. Qiu, P. Li, and B. Lin, "Enhancing the surface sensitivity of colorimetric resonant optical biosensors," Sensors and Actuators B-Chemical **87**, 365-370 (2002).
11. L. F. Desandre and J. M. Elson, "Extinction-Theorem Analysis of Diffraction Anomalies in Overcoated Gratings," Journal of the Optical Society of America a-Optics Image Science and Vision **8**, 763-777 (1991).
12. A. Hessel and A. A. Oliner, "A New Theory of Wood's Anomalies on Optical Gratings," Applied Optics **4**, 1275 (1965).
13. A. Hessel and A. A. Oliner, "Wood Anomaly Effects on Gratings of Large-Amplitude," Optics Communications **59**, 327-330 (1986).
14. M. Neviere, P. Vincent, R. Petit, and M. Cadilhac, "Systematic Study of Resonances of Holographic Thin Film Couplers," Optics Communications **9**, 48 (1973).
15. S. S. Wang, R. Magnusson, J. S. Bagby, and M. G. Moharam, "Guided-Mode Resonances in Planar Dielectric-Layer Diffraction Gratings," Journal of the Optical Society of America a-Optics Image Science and Vision **7**, 1470-1474 (1990).
16. B. Curtis, *Invitation to Biology* (Worth Publishers, New York, 1994), p. 163.
17. B. E. A. Saleh and M. C. Teich, *Fundamentals of Photonics* (John Wiley & Sons, New Jersey, 2007).
18. M. Bouhifd, M. P. Whelan, and M. Aprahamian, "Flourescence imaging spectroscopy utilising acousto-optic tuneable filters," Proceedings of SPIE **5826**, 185-193 (2005).
19. H. Y. Gan, H. X. Zhang, C. T. DeRose, R. A. Norwood, M. Fallahi, J. D. Luo, A. K. Y. Jen, B. Y. Liu, S. T. Ho, and N. Peyghambarian, "Hybrid Fabry-Perot etalon using an electro-optic polymer for optical modulation," Applied Physics Letters **89**, - (2006).
20. E. Hallstig, T. Martin, L. Sjoqvist, and M. Lindgren, "Polarization properties of a nematic liquid-crystal spatial light modulator for phase modulation," Journal of the Optical Society of America a-Optics Image Science and Vision **22**, 177-184 (2005).
21. I. Kurtz, R. Dwelle, and P. Katzka, "Rapid Scanning Fluorescence Spectroscopy Using an Acoustooptic Tunable Filter," Review of Scientific Instruments **58**, 1996-2003 (1987).

22. M. W. Maeda, J. S. Patel, C. L. Lin, J. Horrobin, and R. Spicer, "Electronically Tunable Liquid-Crystal-Etalon Filter for High-Density Wdm Systems," IEEE Photonics Technology Letters **2**, 820-822 (1990).
23. A. Sharon, D. Rosenblatt, A. A. Friesem, H. G. Weber, H. Engel, and R. Steingrueber, "Light modulation with resonant grating-waveguide structures," Optics Letters **21**, 1564-1566 (1996).
24. M. Chen, C. F. Li, M. Xu, W. B. Wang, S. J. Ma, and Y. X. Xia, "Eye-protection glasses against YAG laser injury based on the band gap reflection of one-dimensional photonic crystal," Optics and Laser Technology **39**, 214-218 (2007).
25. M. J. Grout, "Application of bacteriorhodopsin for optical limiting eye protection filters," Optical Materials **14**, 155-160 (2000).
26. M. Haurylau, S. P. Anderson, K. L. Marshall, and P. M. Fauchet, "Electrically tunable silicon 2-D photonic bandgap structures," IEEE Journal of Selected Topics in Quantum Electronics **12**, 1527-1533 (2006).
27. A. S. P. Chang, K. J. Morton, H. Tan, P. F. Murphy, W. Wu, and S. Y. Chou, "Tunable Liquid Crystal Resonant Grating Filter Fabricated by Nanoimprint Lithography," IEEE Photonics Technology Letters **19**, 1457 (2007).
28. N. Inoue and T. Baba, "External control of guided resonance in photonic crystal slab by changing the index anisotropy of liquid crystal," Optoelectronic Materials and Devices **6352**, 63520R (2006).
29. DoITPoMS and U. o. Cambridge, "Introduction to Anisotropy: Liquid Crystals," retrieved April 7, 2008, http://www.doitpoms.ac.uk/tlplib/anisotropy/liquidcrystals.php?printable=1.
30. T. G. Pedersen, P. S. Ramanujam, P. M. Johansen, and S. Hvilsted, "Quantum theory and experimental studies of absorption spectra and photoisomerization of azobenzene polymers," Journal of the Optical Society of America B-Optical Physics **15**, 2721-2730 (1998).
31. S. J. Lalama and A. F. Garito, "Origin of the Non-Linear 2nd-Order Optical Susceptibilities of Organic-Systems," Physical Review A **20**, 1179-1194 (1979).
32. K. D. Singer, J. E. Sohn, L. A. King, H. M. Gordon, H. E. Katz, and C. W. Dirk, "2nd-Order Nonlinear-Optical Properties of Donor-Substituted and Acceptor-Substituted Aromatic-Compounds," Journal of the Optical Society of America B-Optical Physics **6**, 1339-1350 (1989).
33. N. Tabiryan, U. Hrozhyk, and S. Serak, "Nonlinear refraction in photoinduced isotropic state of liquid crystalline azobenzenes," Physical Review Letters **93**, 113901 (2004).
34. N. V. Tabiryan, S. V. Serak, and V. A. Grozhik, "Photoinduced critical opalescence and reversible all-optical switching in photosensitive liquid crystals," Journal of the Optical Society of America B-Optical Physics **20**, 538-544 (2003).
35. S. V. Serak, N. V. Tabiryan, M. Peccianti, and G. Assanto, "Spatial soliton all-optical logic gates," IEEE Photonics Technology Letters **18**, 1287-1289 (2006).
36. U. A. Hrozhyk, S. V. Serak, N. V. Tabiryan, and T. J. Bunning, "Optical tuning of the reflection of cholesterics doped with azobenzene liquid crystals," Advanced Functional Materials **17**, 1735-1742 (2007).
37. A. J. Pidduck, G. P. BryanBrown, S. Haslam, R. Bannister, I. Kitely, T. J. McMaster, and L. Boogaard, "Atomic force microscopy studies of rubbed polyimide surfaces used for liquid crystal alignment," Journal of Vacuum Science & Technology a-Vacuum Surfaces and Films **14**, 1723-1728 (1996).
38. A. Mosley, B. M. Nicholas, and P. A. Gass, "Surface Alignment of Liquid-Crystals by Rubbed Polymer Layers," Displays **8**, 17-21 (1987).
39. J. Stohr, M. G. Samant, A. Cossy-Favre, J. Diaz, Y. Momoi, S. Odahara, and T. Nagata, "Microscopic origin of liquid crystal alignment on rubbed polymer surfaces," Macromolecules **31**, 1942-1946 (1998).
40. F. Yang, G. Yen, and B. T. Cunningham, "Voltage-tuned resonant reflectance optical filter for visible wavelengths fabricated by nanoreplica molding," Applied Physics Letters **90**, 261109 (2007).

41. F. Yang, G. Yen, G. Rasigade, J. A. N. T. Soares, and B. T. Cunningham, "Optically Tuned Optical Reflectance Filter," Applied Physics Letters **92**, 091115 (2008).
42. N. Ganesh, I. D. Block, and B. T. Cunningham, "Near ultraviolet-wavelength photonic-crystal biosensor with enhanced surface-to-bulk sensitivity ratio," Applied Physics Letters **89**, 023901 (2006).
43. N. Ganesh and B. T. Cunningham, "Photonic-crystal near-ultraviolet reflectance filters fabricated by nanoreplica molding," Applied Physics Letters **88**, 071110 (2006).
44. I. D. Block, L. L. Chan, and B. T. Cunningham, "Photonic crystal optical biosensor incorporating structured low-index porous dielectric," Sensors and Actuators B-Chemical **120**, 187-193 (2006).
45. N. Ganesh, A. Xiang, N. B. Beltran, D. W. Dobbs, and B. T. Cunningham, "Compact wavelength detection system incorporating a guided-mode resonance filter," Applied Physics Letters **90**, 081103 (2007).
46. P. C. Mathias, N. Ganesh, L. L. Chan, and B. T. Cunningham, "Combined enhanced fluorescence and label-free biomolecular detection with a photonic crystal surface," Applied Optics **46**, 2351-2360 (2007).
47. I. D. Block, L. L. Chan, and B. T. Cunningham, "Large-area submicron replica molding of porous low-k dielectric films and application to photonic crystal biosensor fabrication," Microelectronic Engineering **84**, 603-608 (2007).
48. D. Rosenblatt, A. Sharon, and A. A. Friesem, "Resonant grating waveguide structures," IEEE Journal of Quantum Electronics **33**, 2038-2059 (1997).
49. S. Tibuleac and R. Magnusson, "Narrow-linewidth bandpass filters with diffractive thin-film layers," Optics Letters **26**, 584-586 (2001).
50. J. W. Goodman, *Introduction to Fourier Optics*, 3 ed. (Roberts & Company, Englewood, 2005).
51. D. L. Brundrett, E. N. Glytsis, T. K. Gaylord, and J. M. Bendickson, "Effects of modulation strength in guided-mode resonant subwavelength gratings at normal incidence," Journal of the Optical Society of America a-Optics Image Science and Vision **17**, 1221-1230 (2000).
52. F. Lemarchand, A. Sentenac, and H. Giovannini, "Increasing the angular tolerance of resonant grating filters with doubly periodic structures," Optics Letters **23**, 1149-1151 (1998).
53. P. Lodahl, A. F. van Driel, I. S. Nikolaev, A. Irman, K. Overgaag, D. L. Vanmaekelbergh, and W. L. Vos, "Controlling the dynamics of spontaneous emission from quantum dots by photonic crystals," Nature **430**, 654-657 (2004).
54. D. Englund, D. Fattal, E. Waks, G. Solomon, B. Zhang, T. Nakaoka, Y. Arakawa, Y. Yamamoto, and J. Vuckovic, "Controlling the spontaneous emission rate of single quantum dots in a two-dimensional photonic crystal," Physical Review Letters **95**, 013904 (2005).
55. M. Makarova, V. Sih, J. Warga, R. Li, L. Dal Negro, and J. Vuckovic, "Enhanced light emission in photonic crystal nanocavities with erbium-doped silicon nanocrystals," Applied Physics Letters **92**, 161107 (2008).
56. G. Subramania, Y. J. Lee, A. J. Fischer, T. S. Luk, C. J. Brinker, and D. Dunphy, "Emission modification of CdSe quantum dots by titanium dioxide visible logpile photonic crystal," Applied Physics Letters **95**, 151101 (2009).
57. T. Baba, D. Sano, K. Nozaki, K. Inoshita, Y. Kuroki, and F. Koyama, "Observation of fast spontaneous emission decay in GaInAsP photonic crystal point defect nanocavity at room temperature," Applied Physics Letters **85**, 3989-3991 (2004).
58. M. Boroditsky, R. Vrijen, T. F. Krauss, R. Coccioli, R. Bhat, and E. Yablonovitch, "Spontaneous emission extraction and Purcell enhancement from thin-film 2-D photonic crystals," Journal of Lightwave Technology **17**, 2096-2112 (1999).
59. I. Yoon, T. Kang, W. Choi, J. Kim, Y. Yoo, S. W. Joo, Q. H. Park, H. Ihee, and B. Kim, "Single Nanowire on a Film as an Efficient SERS-Active Platform," Journal of the American Chemical Society **131**, 758-762 (2009).
60. A. Lucotti and G. Zerbi, "Fiber-optic SERS sensor with optimized geometry," Sensors and Actuators B-Chemical **121**, 356-364 (2007).

61. D. Choi, T. Kang, H. Cho, Y. Choi, and L. P. Lee, "Additional amplifications of SERS via an optofluidic CD-based platform," Lab on a Chip **9**, 239-243 (2009).
62. A. M. Polubotko, "The phenomenon of single-molecule detection by the SERS method and the SERS quadrupole theory," Journal of Optics a-Pure and Applied Optics **1**, L18-L20 (1999).
63. M. Barth, A. Gruber, and F. Cichos, "Spectral and angular redistribution of photoluminescence near a photonic stop band," Physical Review B **72**, 085129 (2005).
64. F. S. Diana, A. David, I. Meinel, R. Sharma, C. Weisbuch, S. Nakamura, and P. M. Petroff, "Photonic crystal-assisted light extraction from a colloidal quantum dot/GaN hybrid structure," Nano Letters **6**, 1116-1120 (2006).
65. I. V. Soboleva, E. Descrovi, C. Summonte, A. A. Fedyanin, and F. Giorgis, "Fluorescence emission enhanced by surface electromagnetic waves on one-dimensional photonic crystals," Applied Physics Letters **94**, 231122 (2009).
66. F. Yang, G. Yen, and B. T. Cunningham, "Integrated 2D photonic crystal stack filter fabricated using nanoreplica molding," Optics Express **18**, 11846-11858 (2010).
67. D. Graham-Rowe, "From dots to devices," Nature Photonics **3**, 307-309 (2009).
68. X. Y. Wang, X. F. Ren, K. Kahen, M. A. Hahn, M. Rajeswaran, S. Maccagnano-Zacher, J. Silcox, G. E. Cragg, A. L. Efros, and T. D. Krauss, "Non-blinking semiconductor nanocrystals," Nature **459**, 686-689 (2009).
69. J. McBride, J. Treadway, L. C. Feldman, S. J. Pennycook, and S. J. Rosenthal, "Structural basis for near unity quantum yield core/shell nanostructures," Nano Letters **6**, 1496-1501 (2006).
70. V. Sukhovatkin, S. Hinds, L. Brzozowski, and E. H. Sargent, "Colloidal Quantum-Dot Photodetectors Exploiting Multiexciton Generation," Science **324**, 1542-1544 (2009).
71. S. A. McDonald, G. Konstantatos, S. G. Zhang, P. W. Cyr, E. J. D. Klem, L. Levina, and E. H. Sargent, "Solution-processed PbS quantum dot infrared photodetectors and photovoltaics," Nature Materials **4**, 138-142 (2005).
72. V. Aroutiounian, S. Petrosyan, A. Khachatryan, and K. Touryan, "Quantum dot solar cells," Journal of Applied Physics **89**, 2268-2271 (2001).
73. S. Gimenez, I. Mora-Sero, L. Macor, N. Guijarro, T. Lana-Villarreal, R. Gomez, L. J. Diguna, Q. Shen, T. Toyoda, and J. Bisquert, "Improving the performance of colloidal quantum-dot-sensitized solar cells," Nanotechnology **20**, 295204 (2009).
74. P. O. Anikeeva, J. E. Halpert, M. G. Bawendi, and V. Bulovic, "Quantum Dot Light-Emitting Devices with Electroluminescence Tunable over the Entire Visible Spectrum," Nano Letters **9**, 2532-2536 (2009).
75. N. Tessler, V. Medvedev, M. Kazes, S. H. Kan, and U. Banin, "Efficient near-infrared polymer nanocrystat light-emitting diodes," Science **295**, 1506-1508 (2002).
76. V. Wood, M. J. Panzer, J. L. Chen, M. S. Bradley, J. E. Halpert, M. C. Bawendi, and V. Bulovic, "Inkjet-Printed Quantum Dot-Polymer Composites for Full-Color AC-Driven Displays," Advanced Materials **21**, 2151-2155 (2009).
77. K. S. Cho, E. K. Lee, W. J. Joo, E. Jang, T. H. Kim, S. J. Lee, S. J. Kwon, J. Y. Han, B. K. Kim, B. L. Choi, and J. M. Kim, "High-performance crosslinked colloidal quantum-dot light-emitting diodes," Nature Photonics **3**, 341-345 (2009).
78. M. Fox, *Quantum Optics* (Oxford University Press, 2006).
79. J. J. Peterson and T. D. Krauss, "Photobrightening and photodarkening in PbS quantum dots," Physical Chemistry Chemical Physics **8**, 3851-3856 (2006).